1-1-2013

Creation of an Internal State Variable Plasticity-Damage-Corrosion Model Validated by Experiments with Magnesium Alloys

Christopher Avery Walton

Creation of an internal state variable plasticity-damage-corrosion model validated by experiments with magnesium alloys

By

Christopher Avery Walton

A Dissertation
Submitted to the Faculty of
Mississippi State University
in Partial Fulfillment of the Requirements
for the Degree of Doctor of Philosophy
in Engineering
in the Department of Mechanical Engineering

Mississippi State, Mississippi

December 2013

Creation of an internal state variable plasticity-damage-corrosion model validated by experiments with magnesium alloys

By

Christopher Avery Walton

Approved:

_____

Mark F. Horstemeyer
(Major Professor)

_____

Holly J. Martin
(Committee Member)

_____

Tonya W. Stone
(Committee Member)

_____

Paul T. Wang
(Committee Member)

_____

Kalyan K. Srinivasan
(Graduate Coordinator)

_____

Achille Messac
Dean
Bagley College of Engineering

Name: Christopher Avery Walton

Date of Degree: December 14, 2013

Institution: Mississippi State University

Major Field: Engineering

Major Professor: Mark F. Horstemeyer

Title of Study: Creation of an internal state variable plasticity-damage-corrosion model validated by experiments with magnesium alloys

Pages in Study: 113

Candidate for Degree of Doctor of Philosophy

In this study, a new consistent formulation coupling kinematics, thermodynamics, and kinetics with damage using an extended multiplicative decomposition of the deformation gradient that accounts for corrosion effects is presented. The technical approach used for modeling the corrosion behavior of magnesium alloys was divided into three primary steps. First, a predictive corrosion model was developed based on experimental corrosion observations. The experimentally-observed corrosion mechanisms of pitting, intergranular, and general corrosion on the AZ31 magnesium alloy were quantified in 3.5 wt.% NaCl immersion and salt spray environments using optical microscopy and laser profilometry to document the changes in the pit characteristics. Although both environments showed similar trends, the immersion environment was more deleterious with respect to intergranular and general corrosion. On the other hand, the salt-spray environment allowed deeper pits to form throughout the entirety of the experiments, which led to a substantial thickness drop (general corrosion) compared with the immersion environment. Next, the complete corrosion model based upon the internal state variable theory was formulated to capture the effects of pit

nucleation, pit growth, pit coalescence, and general corrosion. Different rate equations were given for each mechanism. Following the formulation of the model, the aforementioned experimental work and experimental work on four other magnesium alloys (AZ61, AM30, AM60, and AE44), was used to validate the model.

Keywords: Corrosion, Modeling, Magnesium Alloy, Internal State Variable

DEDICATION

I would like to dedicate this work to my family, especially my parents, T.A. and Vivian, and my fiancé, Jazmin Hamilton, for supporting me throughout graduate school.

ACKNOWLEDGEMENTS

First, I would like to thank my major professor Dr. Mark F. Horstemeyer for the continuous guidance and help since I arrived at Mississippi State. I would also like to thank my committee members Dr. Holly Martin, Dr. Tonya Stone, and Dr. Paul Wang for technical guidance and support. Also, I would like to thank Dr. Doug Bammann for his technical assistance with the theoretical efforts of this work.

I would like to thank the following people for assisting with the collection of some of the experimental data presented herein: Weiwei Song, Wil Whittington, Scott Turnage, Ayesha Hicks, Jasmine Danzy, and Christopher Horstemeyer.

Financial support from the Center for Advanced Vehicular Systems at Mississippi State University is gratefully acknowledged. This work was also supported by the Department of Energy, the National Energy Technology, and the Department of Defense. Also, I would like to acknowledge the James Worth Bagley College of Engineering, NASA Mississippi Space Grant Consortium, the National GEM Consortium, and Corning Incorporated for fellowship funding.

TABLE OF CONTENTS

LIST OF TABLES

LIST OF FIGURES

LIST OF ABBREVIATIONS

Al: Aluminum

CAFE: Corporate Average Fuel Economy

CAVS: Center for Advanced Vehicular Systems

EDS: Energy Dispersed X-Ray Spectroscopy

FE: Finite Element

HE: Hydrogen Embrittlement

ICAF: Intergranular Corrosion Area Fraction

IGSCC: Intergranular Stress Corrosion Cracking

ISV: Internal State Variable

Mg: Magnesium

MOOSE: Multiphysics Object Oriented Simulation Environment

MSU: Mississippi State University

NND: Nearest Neighbor Distance

RE: Rare Earth

SCC: Stress Corrosion Cracking

SEM: Scanning Electron Microscope

TGSCC: Transgranular Stress Corrosion Cracking

Zn: Zinc

CHAPTER I

INTRODUCTION

1.1 Motivation

Magnesium (Mg) alloys exhibit the attractive combination of low densities and high strength per weight ratios (comparable or greater than that of precipitation strengthened Al alloys), along with good damping capacity, castability, weldability, and machinability [1–4]. The National Academy of Science report on Corporate Average Fuel Economy (CAFE) standards indicates that a 10% reduction in weight results in 6.6-8% increase in fuel efficiency [5]. Because of these characteristics, Mg alloys are being increasingly used in electronics, automobiles, and aerospace industries [2–4,6]. Of the various commercial Mg alloys, those developed from the Al-Zn ternary system (i.e. the as-named AZ alloys) have found the largest number of industrial applications [3]. The principal drawbacks of Mg alloys are their high chemical activity leading to a low corrosion resistance [4,7–10] and the higher cost [11,12]. When exposed to saltwater, Mg has a high corrosion rate, relegating its current use to unexposed locations within the vehicle [13–15]. By altering the microstructure with the addition of various elements, including aluminum (Al), zinc (Zn), manganese (Mn), and rare earth (RE) elements, the corrosion rate of Mg alloys can be reduced [9,16,17]. In addition to the alteration of the microstructure, the method of processing Mg alloys can also affect the corrosion rate. The presence of an as-cast skin often found on castings, which consists of very small

grains formed during alloy cooling, improves the corrosion resistance of the Mg alloy ten-fold [9,18]. While castings are commonly used for parts of a vehicle, such as control arms or engine cradles, extruded metal is also used for bumpers and doors. Therefore, a detailed understanding of Mg's response to various corrosion conditions from different processing and product environments, through the modeling of general, pitting, and intergranular corrosion is needed.

Since Mg is electrochemically the most active structural material, it will corrode preferentially. A more critical use of Mg in load bearing components requires not only a good understanding on how to model mechanical response, but also its response to aggressive corrosion environments. It can be generally stated that the combined action of corrosion and stress can cause premature failure compared to the failure rate of the two loading cases separately. Due to the serious negative effects on durability, corrosion of Mg alloys should trigger substantial attention focused on modeling the corrosion behavior under automotive service conditions. Knowledge of environmental factors that influence degradation, types of corrosion to which Mg alloys are most susceptible, protection schemes, and design considerations can significantly minimize corrosion and increase the use of this family of lightweight alloys.

1.2 Internal State Variable Damage Modeling

Over the past few decades, significant research has been published to formulate constitutive models for ductile materials using multiplicative decomposition of the deformation gradient (e.g. [19–28]). The idea of utilizing multiplicative decomposition of the deformation gradient to describe the finite deformation elastic-plastic response was introduced by Bilby et al. [29] and independently by Kröner [30]. For the corrosion

model presented in this dissertation, a kinematic approach where the deformation due to internal defects appears naturally and that is capable of describing the isotropic behavior will be used. Previous researchers [28,31–37] have taken the same approach of kinematic decomposition.

Coleman and Gurtin [38] were the first to lay out a framework for internal state variable (ISV) theory. Horstemeyer and Bammann [39] recently presented a history review of ISV theory but did not mention any application to corrosion. In the context of this dissertation, Horstemeyer et al. [35] modified the Bammann ISV Plasticity model [32] to capture the stress state dependent damage evolution and to include the heterogeneities of microstructure for damage progression and failure analysis. The model by [35] is used as the basis for this study and requires additional modifications to account for corrosion-based stress state dependent damage evolution. The rate equations are generally written as objective rates with indifference to the continuum frame of reference assuming a Jaumann rate in which the continuum spin equals the elastic spin [40]. The ISV equations are functions of the observable variables: temperature, stress, and strain. In general, the rate equations of generalized displacements, or thermodynamics fluxes, describing the rate of change may be written as independent equations for each ISV or as derivatives of a suitably chosen potential function arising from the hypothesis of generalized normality [19]. The selection of the ISVs may, in principle, be somewhat arbitrary, but the kinematic hardening, isotropic hardening, and damage rate equations are physically motivated and strongly influence the history of the material and can be garnered from lower length scale arguments [40]. The ISV model accounts for deviatoric inelastic deformation resulting from the presence of dislocations in crystalline material,

dilatational deformation, and ensuing failure from damage progression [40]. Damage will reduce the material strength, enhance the inelastic flow, and soften the elastic moduli.

1.3 Corrosion Damage Modeling

There is limited published work on Mg corrosion modeling. There have been a few corrosion modeling studies at the electronic and atomistic scale. Kwak and Chaudhuri [41] presented a first-principle-based analysis on the role of RE doping on Mg alloy corrosion. They concluded that the electronic effect by the RE doping could significantly enhance the integrity of oxide films formed on the Mg alloys. Xiao et al. [42] completed a study in which they examined the effects of intermetallic particles in localized corrosion. This model integrates the complex alloy microstructure and composition into the modeling framework which greatly enhances the predictive power and it allows a more comprehensive characterization of the corrosion process [42].

At the microscopic level, Deshpande [5] created a numerical model capturing the evolution of cross-sectional microstructure to investigate its effect on corrosion behavior. The model incorporates various α-Mg phase-β phase configurations along the depth of the alloy. Deshphande found that a configuration with a continuous network of β phase around the α phase, as in die casting, provides the best corrosion resistance [5]. Also, the corrosion rate was found to be higher during the initial stages due to increased β phase fraction, but corrosion was halted after the α phase preferentially dissolved in the electrolyte solution, exposing the β phase which is less electrochemically active [5].

Dietzel et al. [43] developed a mesoscale model predicting the hydrogen embrittlement (HE) effect on the stress-strain response of an AZ91 Mg alloy exposed to

distilled water. The effect of HE on the stress-strain curves was simulated by assuming that the hydrogen was generated in localized corrosion pits and subsequently diffuses into the bulk, thereby reducing the strain-to-failure [43]. These few examples of corrosion modeling in the literature present very valuable information about hydrogen effects on mechanical properties.

1.4 Multiscale Modeling

To accurately model both chemical and mechanical mechanism effects, one must use multiscale modeling techniques. The modeling philosophy "From Atoms to Autos" at Mississippi State University's (MSU) Center for Advanced Vehicular Systems (CAVS) is used as the foundation to capture the history effects from lower length scales (i.e. Electronics Principles) to the full structural scale material model. Using that philosophy and starting with the end in mind, the ability to use different forms of Mg alloys for structural automobile applications is the end goal. As an example, the Chevrolet Corvette engine cradle is being cast from an AE44 (Al-Rare Earth Elements ternary) Mg alloy. The success of the engine cradle project shows that there is opportunity to create lightweight structural members for automobiles, but being able to accurately model the multiscale effects through up scaling and down scaling principles will be vital to further improvement.

The importance of figuring out what is needed (down scaling) and what is to be given (up scaling) between length scales creates "bridges" that connect the length scales to construct the entire model. Integrating corrosion mechanisms and recognizing the interaction and effects at all lengths scales becomes very important. The major length scales to consider include: electronics scale, nanoscale, microscale, mesoscale,

macroscale, and structural scale. Since this modeling philosophy is a top-down approach, the last bridge would be the structural finite element analysis to determine the feasibility of the material for the application. The finite element analysis bridge is preceded by the material modeling bridge from the macroscale ISV continuum level. The macroscale ISV continuum level requires information from all length scales (down scaling) to address the performance and manufacturing processes. Depicted in Figure 1.1, each length scale also depends on every other length scale to carry out the history of damage for the material.

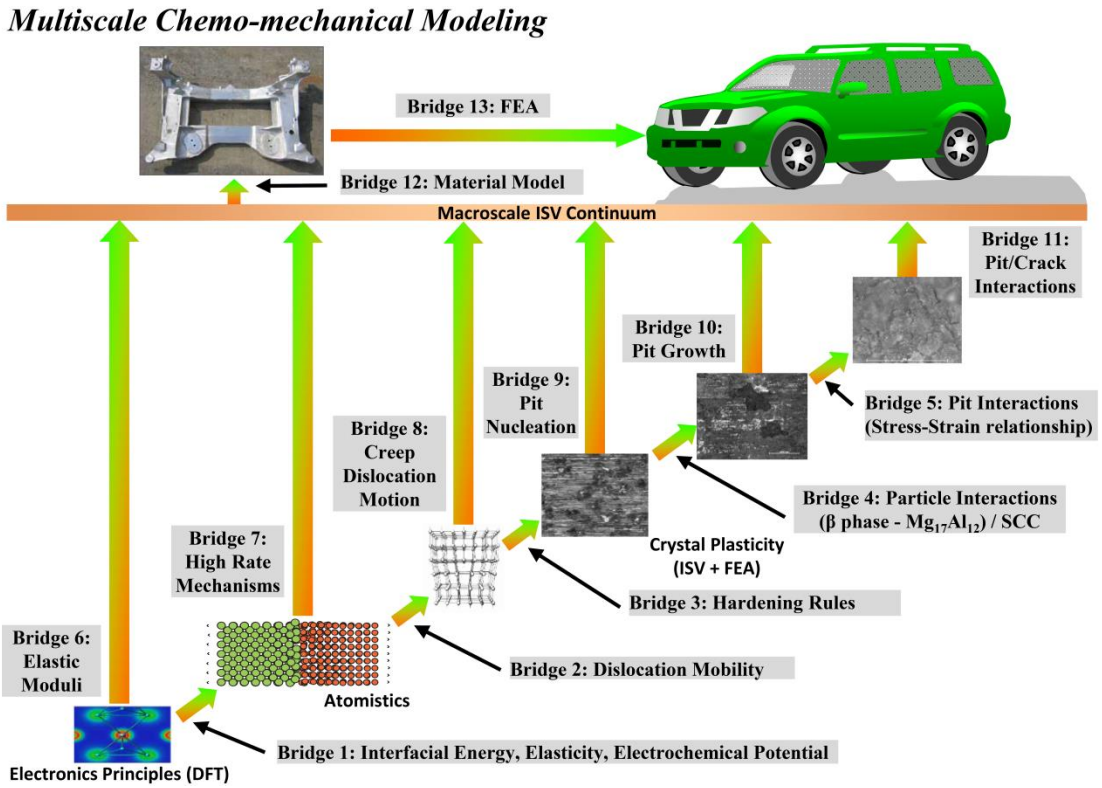

Figure 1.1 Multiscale modeling approach to chemomechanical modeling

1.5 Dissertation Structure

Chapter I was a general introduction to the dissertation and provided the motivation behind this work and a literature of the topics to be covered. Chapter II presents experimental results, delineating the three major corrosion mechanisms: general, pitting and intergranular corrosion. The corrosion mechanisms were examined on an extruded AZ31 Mg alloy subjected to immersion and salt-spray environments. The three mechanisms were quantified using optical microscopy and laser profilometry for over 60 hours of testing. Chapter III presents the formulation of the macroscale corrosion damage model. The corrosion model captures the effects of general corrosion, pit nucleation, pit growth, pit coalescence, and intergranular corrosion. The different geometrically-affected rate equations are given for each mechanism after the ISV formalism and have a thermodynamic force pair that acts as an internal stress. Chapter IV presents the application of the aforementioned model to Mg alloys of different forms and alloying element compositions. Chapter V details a chemomechanical experimental study, determining the corrosion effects on the tensile and stress relaxation behavior of an extruded AZ31 Mg alloy subjected to immersion and salt-spray environments. Finally, Chapters VI and VII summarize the results of this study and give recommendations for the continuing of this research.

CHAPTER II

QUANTIFICATION OF CORROSION MECHANISMS ON AN EXTRUDED AZ31 MAGNESIUM ALLOY

2.1 Introduction

Corrosion testing is usually performed using two main techniques, salt spray and immersion testing. The literature contains many such studies on various Mg alloys under salt spray [44–51] and immersion tests [52–59]. The two testing environments are so commonly used that ASTM standards have been developed for both the salt spray environment and the immersion environment, labeled as ASTM B-117 and ASTM G-31, respectively [60,61]. However, the two ASTM standards require different concentrations of salt, meaning that a direct comparison between the results obtained from the two methods cannot be made [60,61]. In addition, the two methods do not translate well to corrosion field tests performed for the automotive industry [62,63]. This issue has led to the industrial development of cyclical tests, which contain a pollution phase and a wet or dry phase, in an effort to expose test alloys to the environmental factors associated with engine cradles, such as de-icing salt, mud, and condensation [63,64]. However, even an accurate comparison between these tests cannot be made, as none of the variables are similar, with varying concentrations of salt, temperature, humidity, and exposure time [63]. Also, the electrochemical potential changes as the pH of the solution increases and a Mg hydroxide film forms on the surfaces of these alloys [4,17,56,65]. This

phenomenon also varies between uninterrupted (continuous exposure until end of testing) or interrupted (analyzed at specific testing times) studies. The experimental work presented examines the interrupted testing procedure. Both the immersion and salt spray were employed in this research study in an effort to expose the AZ31 Mg alloy to an environment similar to that experienced by automotive engine blocks.

It is typical to see surface characteristics of the corrosion specimens being studied under optical microscopy. Optical microscopy allows for the examination of specimen surface changes in a non-destructive manner. Another method described in this section not well documented for Mg alloys under NaCl environments is laser profilometry. In literature, optical and laser profilometry have been used to analyze specimens under aggressive environments and documented for Al alloys [66–68], stainless steel alloys [69], and Mg alloys [7,49,51]. Laser profilometry is also a non-destructive method which gives 3D maps of specimen surfaces for pit size quantification.

In this chapter, the corrosion mechanisms of extruded AZ31 are investigated, which has not been evaluated before in the context of comparing salt spray and immersion corrosion methods. Specifically, AZ31 defects were analyzed by examining the pitting corrosion, intergranular corrosion, and general corrosion as they occurred over a 60 hour period in two corrosion environments: cyclic salt-spray and immersion. As such, this research is an effort to determine how common exposure environments, similar to those experienced by automobiles, affect corrosion mechanisms.

2.2 Materials and Experimental Methods

2.2.1 Testing

Twelve AZ31 (Mg-3Al-1Zn) coupons (3.00 cm x 1.86 cm x varying thicknesses) were cut from extruded sheet squares using a vertical band saw (MSC Industrial Supply Company, Columbus, MS). The coupon surfaces were left untreated, with no surface grinding or polishing, to test the corrosion effects on the extruded AZ31 Mg alloy. For the cyclic salt spray testing, a Q-Fog CCT (Q-Panel Lab Products, Cleveland, OH) was used to cycle through three stages set at equal times, including a 3.5 wt.% NaCl spray at 35 °C, 100% humidity using distilled water at 35 °C, and a drying purge at 35 °C. For immersion testing, an aquarium with an aeration unit was filled with 3.5 wt.% NaCl at room temperature. For both tests, the six coupons per test environment were hung at 20° to the horizontal, as recommended by ASTM B-117 [41]. The coupons were exposed to the test environment for 1 h, removed, rinsed with distilled water to remove excess salt, and dried in a dessicator. Following the profilometer analysis, the coupons were then placed back into the test environment for an additional 3 h, an additional 8 h, an additional 24 h, and another 24 h. These times allowed for a longitudinal study to follow pit growth and surface changes over time, where $t_0 = 0$ h, $t_1 = 1$ h, $t_2 = 4$ h, $t_3 = 12$ h, $t_4 = 36$ h, and $t_5 = 60$ h. Between analyses and environmental exposures, the coupons were stored in a desiccator to ensure that no further surface reactions occurred.

2.2.2 Analysis

Following each time exposure of the tests, the coupons were analyzed using optical microscopy and laser profilometry. The coupons were also weighed prior to testing and following each exposure on two different scales and an average was taken.

Four thickness measurements were taken on each sample prior to and following the test. Measurements for all figures were averaged from the data with error bars based on one standard deviation.

Optical microscopy with an inverted light was used to take multiple images of the exposed surfaces at 5x and 10x magnification (Axiovert 200M Mat, Carl Zeiss Imaging Solutions, Thornwood, NY). The 5x magnification images were combined and then analyzed using the ImageAnalyzer (v. 2.1-2) provided by Mississippi State University to determine the number of pits, the pit surface area, the nearest neighbor distance (NND), and the intergranular corrosion area fraction necessary for the development of a corrosion model not detailed in this chapter but previously outlined by Horstemeyer *et al.* [35]. The 10x magnification was used to pictorially show the changes over the six cycles. Laser profilometry was used to scan a 1 mm by 1 mm area on two coupons per environment following each test cycle (Talysurf CLI 2000, Taylor Hobson Precision Ltd, Leicester, England). The resulting 2-D and 3-D images were used to document the changes in the pit characteristics due to the different test environments over the six cycles (Talymap Universal, v. 3.18, Taylor Hobson Precision Ltd, Leicester, England). Forty-eight data points where taken per environment per cycle.

2.3 Experimental Results

Figure 2.1 shows the average weight change over the five exposure times for both the immersion and salt spray environments. For both environments, they followed a linear trend. The immersed samples showed a weight loss compared to a weight gain observed on the salt spray samples. Figure 2.2 shows the changes in thickness of the coupons for the immersion and salt spray environments. Both environments followed a

logarithmic trend as a function of time. The immersion showed a thickness loss that was less than the salt spray samples.

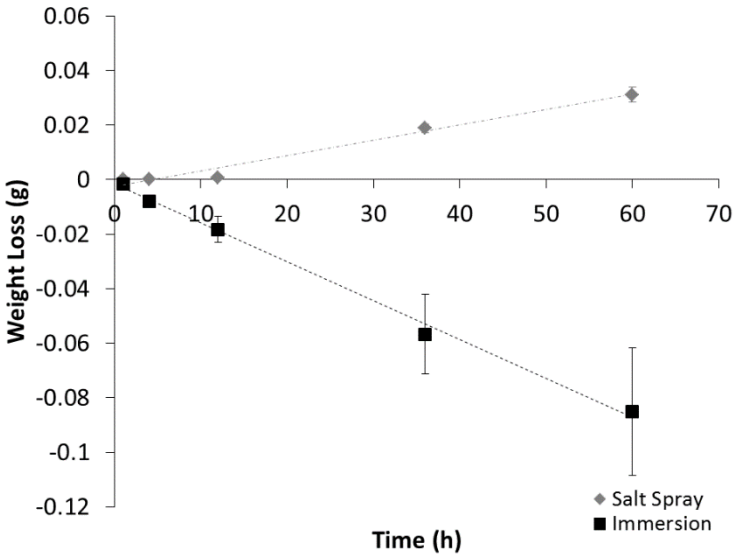

Figure 2.1 The average weight change of extruded AZ31 coupons based on a test environment over 60 hours.

The error bars were one standard deviation in each direction. Notice that the coupons exposed to the salt spray environment not only did not lose weight but actually gained weight due to the attachment of chloride ions. Note that both weight changing trends followed a linear behavior.

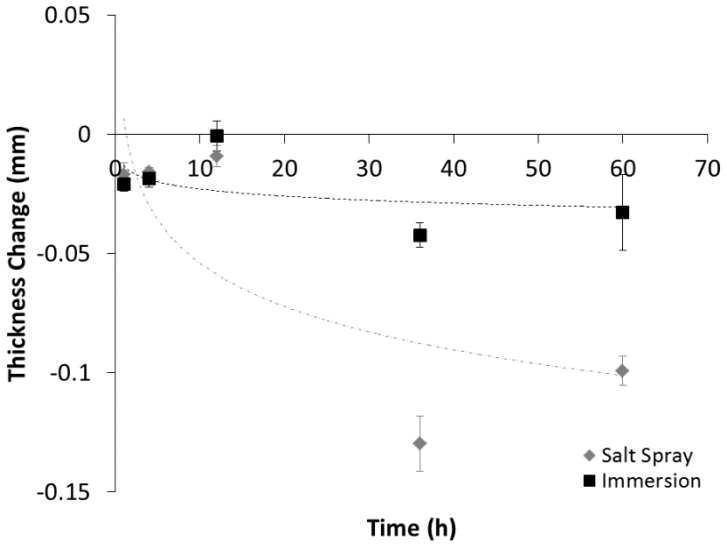

Figure 2.2 Average thickness loss of AZ31 coupons based on test environment over 60 hours.

The error bars were one standard deviation in each direction. Notice that the coupons exposed to the immersion environment lost less magnesium than the coupons exposed to the salt spray environment, although the thickness loss followed the same logarithmic trend.

In Figure 2.3, the maximum and mean pit depths over the exposure time for both immersion and salt spray environments followed a second-order polynomial trend. In the salt spray environment, the maximum and mean pit depth showed increasing trends. The maximum pit depth trend was increasing at a faster rate than the mean pit depth. In the immersion environment, the maximum and mean pit depth showed slightly decreasing trends.

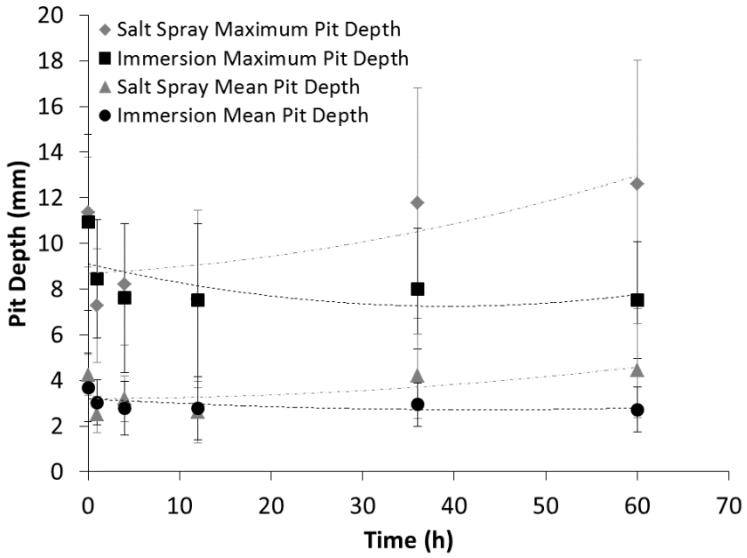

Figure 2.3 Maximum and mean pit depths based on test environment over 60 hours. The error bars were one standard deviation in each direction. Notice that the maximum pit depth and the mean pit depth for the salt spray environment increased. Also, notice that the maximum pit depth and the mean pit depth for the immersion environment decreased.

Figure 2.4 graphically represents the pit 3-D surface area throughout the experiment. The trends for the immersion and salt spray environments were comparable and followed approximately the same second-order polynomial. Both environments showed that as time increased, the pit surface area increased. Notice that at t_3 and t_5, the error bars increased in the immersion environment indicating that there was a large variation in the surface area of the pits.

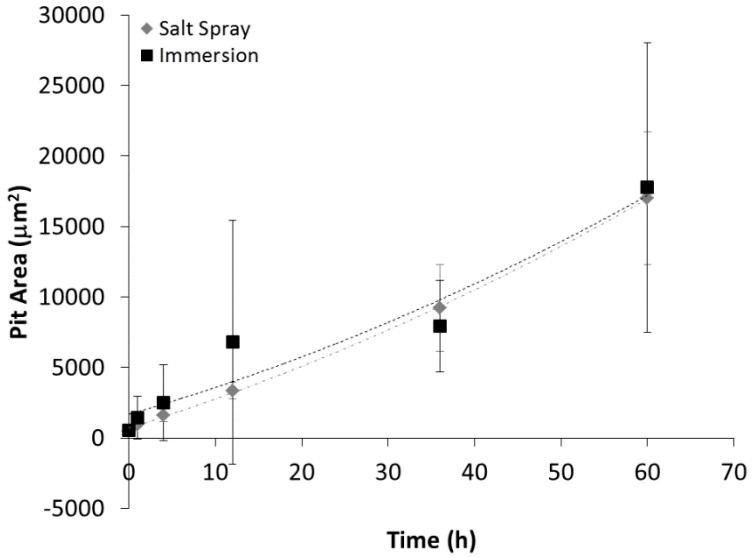

Figure 2.4 Individual pit surface area based on test environment over 60 hours.

The error bars were one standard deviation in each direction. Notice that the initial pit area for both environments was approximately the same. However, after the initial exposure, the pit area on the immersion surfaces was larger. Both surfaces followed a slight second-order polynomial trend.

Figure 2.5 shows the changes in pit volume during the five exposure times. The pit volume for the immersion environment and salt spray environment followed slight second-order polynomial trends. The salt spray environment initially started off with a higher pit volume and then decreased below the immersion environment trend between t_3 and t_4, at approximately 25 hours. By t_5, the pit volume for the salt spray environment was higher again.

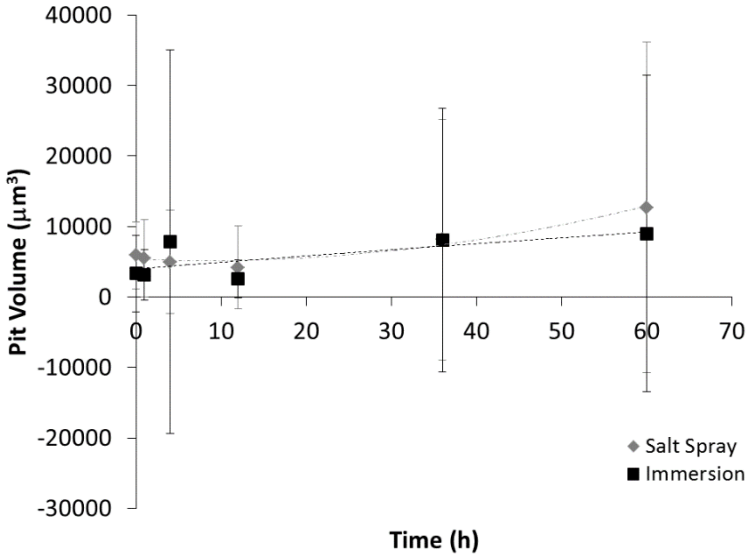

Figure 2.5 Individual pit volume based on test environment over 60 hours.

The error bars were one standard deviation in each direction. Notice that the initial pit volume was higher for the salt spray environment as compared to the immersion environment. The salt spray surface followed a second-order polynomial trend, although the volume mainly increased, while the immersion surface reached a saturation value.

Figure 2.6 shows the change in pit number density, which is the number of pits per unit area, for both the immersion environment and the salt spray environment as a function of time. Both environments experienced a downward second-polynomial trend. The pit number density observed in the immersion environment, however, always stayed higher than the salt spray environment.

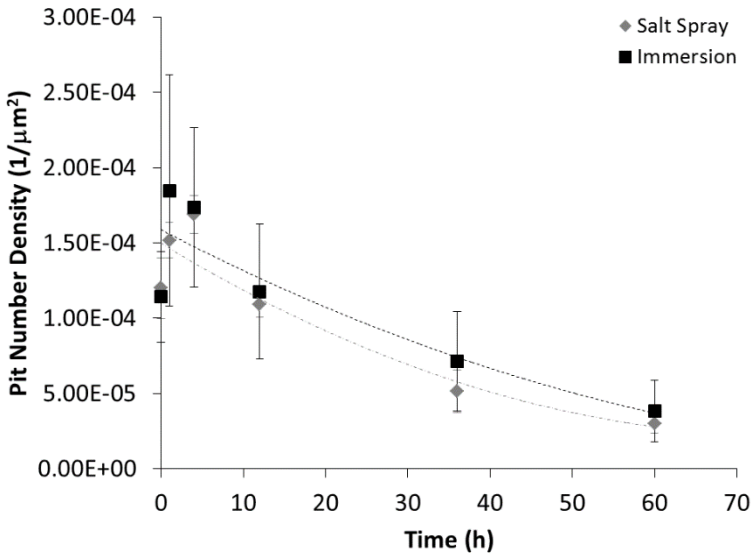

Figure 2.6 Pit Number Density based on test environment over 60 hours.

The error bars were one standard deviation in each direction. Notice that the initial number of pits on the surface was higher for the immersion environment as compared to the salt spray environment. The pit number density for the immersion surface increased the first hour then began to decrease. The salt spray surface pit number density also increased until 4 hours and then began to decrease.

In Figure 2.7, the pit area based on the 2-D area covered by the pits as observed by the micrographs for the immersion and salt spray environments is shown. The two environments were very comparable with an increasing second-order polynomial trend. The immersion environment trend stayed slightly higher than the salt spray environment trend throughout the 60 hours.

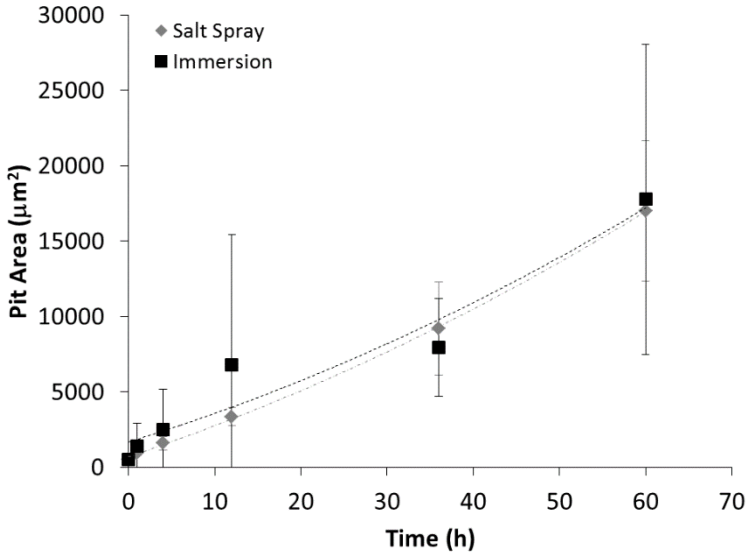

Figure 2.7 In-Plane pit area based on test environment over 60 hours.

The error bars were one standard deviation in each direction. Notice that the initial pit area on the surface was approximately equal for the immersion environment as compared to the salt spray environment. Also note the large deviation in pit area for both environments at 12 hours, indicating a large difference due to growth and coalescence of previously formed pits and pit nucleation. The immersion and salt spray surfaces followed a slight second-order polynomial trend throughout the tests.

Figure 2.8 shows the changes in the NND, which is the distance between two pits, for the two environments being tested. Both environments showed an increasing trend starting at approximately the same initial condition. The salt spray specimens NND increased at a higher rate than the immersion environment.

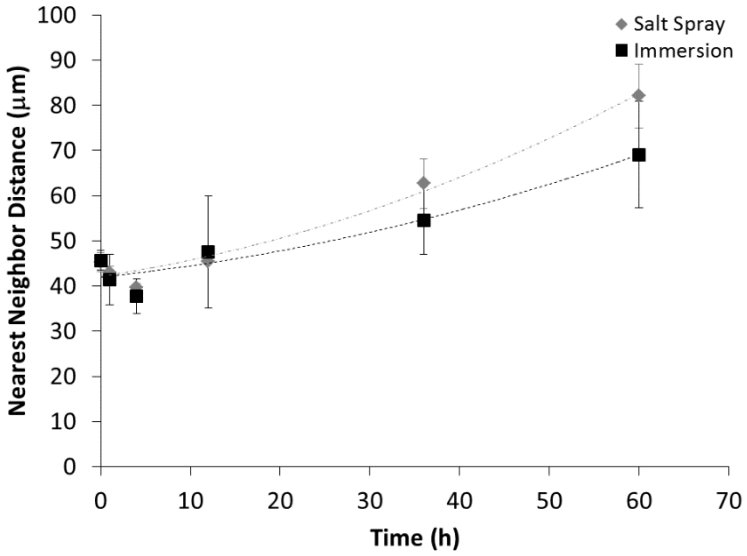

Figure 2.8 Nearest Neighbor Distance based on test environment over 60 hours.

The error bars were one standard deviation in each direction. Notice that the initial nearest neighbor distance on the surface was about the same for the immersion and salt spray environments. Both the immersion surface and the salt spray surface followed second-order polynomial trends. The nearest neighbor distance decreased initially until about 4 hours before increasing.

In Figure 2.9, the changes in the intergranular corrosion area fraction (ICAF) for the salt and immersion environments are shown. The ICAF shows how much of the surface is experiencing corrosion at the β-phase ($Mg_{17}Al_{12}$) precipitates of the alloy that nucleate at the grain boundaries of the microstructure. On both immersion and salt spray surfaces, a second-order polynomial trend was observed. The ICAF initially increased for the immersion specimens until approximately 25 hours, before decreasing rapidly to values below that of the salt spray environment at 60 hours. The ICAF experienced by the salt spray specimens increased until approximately 35 hours and decreased from there.

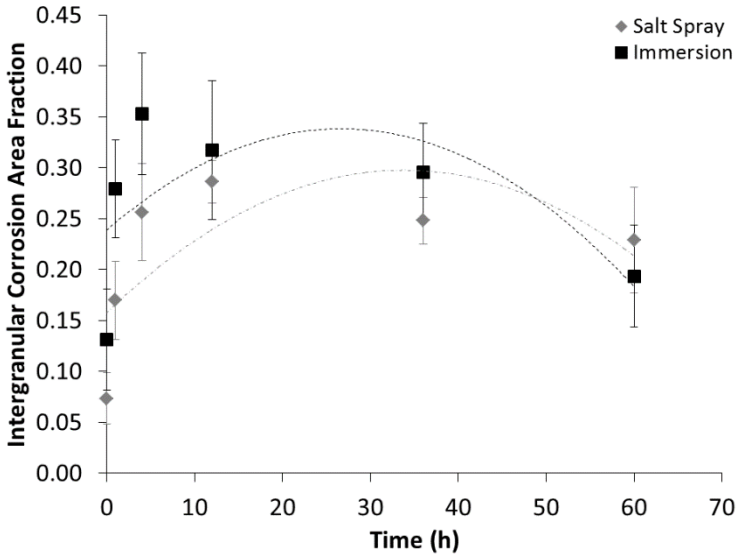

Figure 2.9 Intergranular Corrosion Area Fraction based on test environment over 60 hours.

The error bars were one standard deviation in each direction. Notice that the initial intergranular corrosion area fraction on the surface was higher for the immersion environment as compared to the salt spray environment. Both the immersion surface and the salt spray surface followed second-order polynomial trends. The ICAF increased until approximately 35 hours for the salt spray environment and approximately 25 hours for the immersion environment before decreasing.

Figures 2.10-2.11 pictorially show the changes in individual pit characteristics in 2-D over the 60 hours for both the salt spray environments (Figure 2.10) and the immersion environments using laser profilometry, respectively. Figures 2.12-2.13 show the pit characteristics in 3-D of the salt spray and immersion environments, respectively. In both figures, the changes between individual pits covering an area of 0.2 mm by 0.2 mm for each time was examined, where $t_0 = 0$ h, $t_1 = 1$ h, $t_2 = 4$ h, $t_3 = 12$ h, $t_4 = 36$ h, and $t_5 = 60$ h. The color legend gives an indication of the depth of the pits in the figure. The lowest points within the pits are shown by shades of blue, while the highest points outside the pits are shown by the pinks and reds. When looking at the salt spray surface (Figure 2.10 and Figure 2.12), the pit number initially increased from t_0 to t_2. Following t_3, the

pits began to coalesce until one larger pit was visible shown by the increase in the blue area. Also, as time passed, the larger pit increased in depth from approximately 90 μm at t_4 to 140 μm at t_5. The immersion environment surface (Figure 2.11 and Figure 2.13) pit depth increased with time as well. Notice that from t_0 to t_3 that the pit number stayed approximately the same. At t_4, however, more pits began to form before coalescencing at t_5 indicated by the transition from a rougher to a flatter surface.

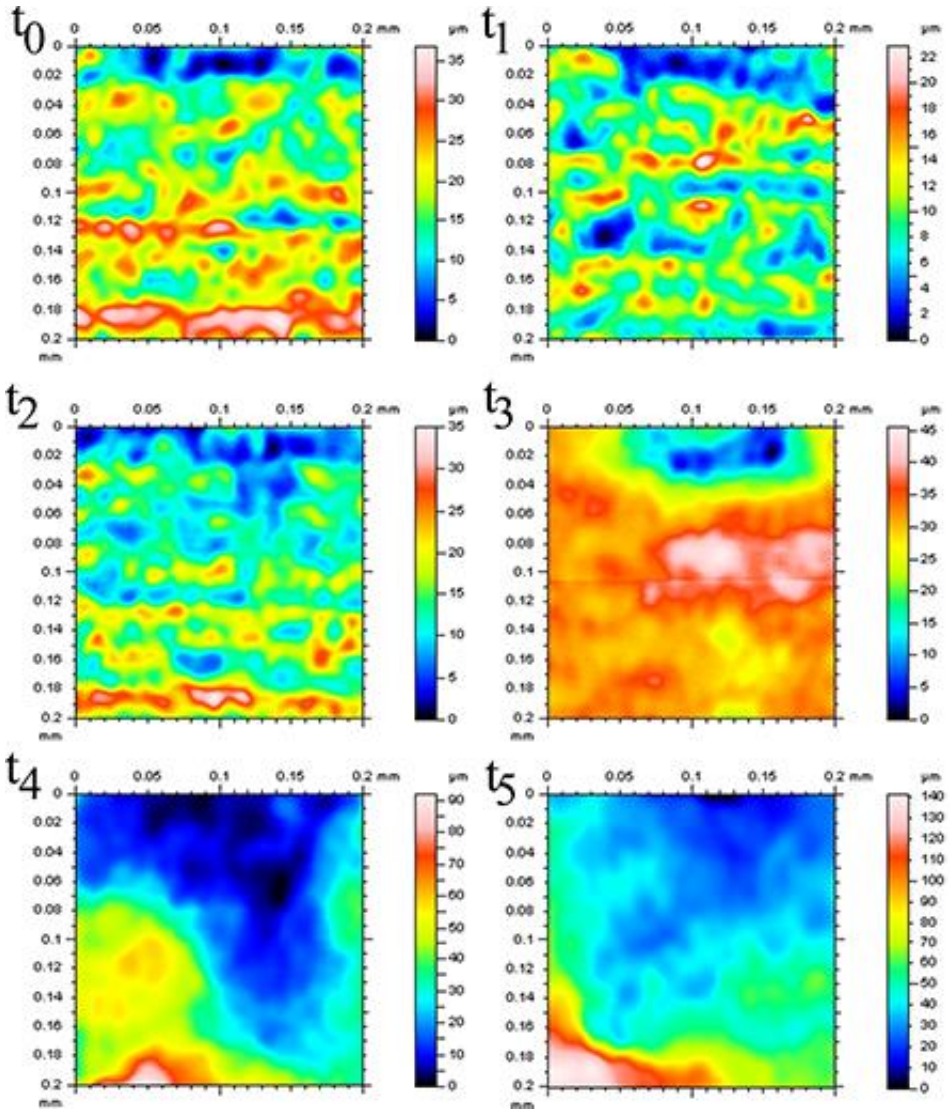

Figure 2.10 2-D Laser Profilometry of the salt spray surface over 60 hours.

All spots were examined over a 30 µm x 30 µm area. Height measurements were made from the lowest point, shown as dark blue and listed as zero in the legend, to pink and red areas that indicate height. Notice that the number of pits initially grew in number from t_0 to t_2 (4 h), while the pits grew in area connecting with neighbors from t_3 to t_5.

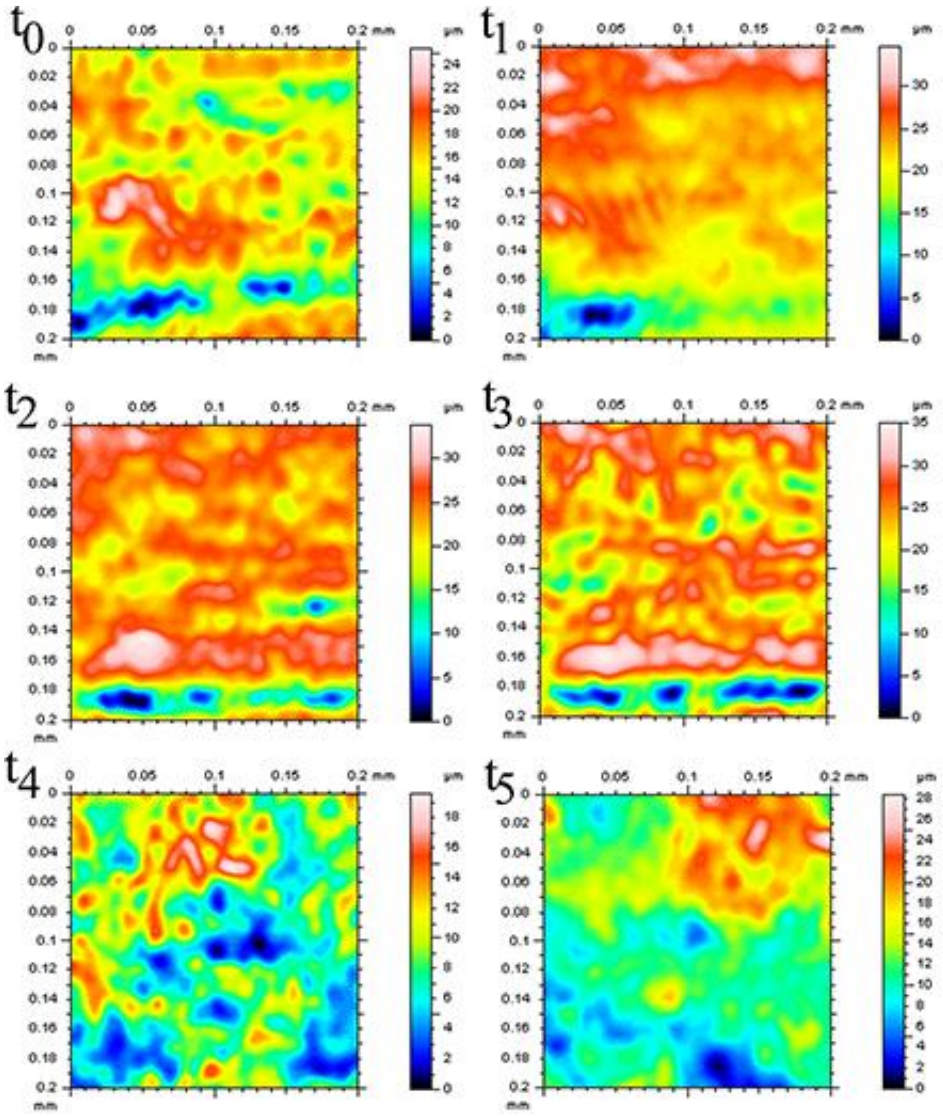

Figure 2.11 2-D Laser Profilometry of the immersion surface over 60 hours.

All spots were examined over a 30 μm x 30 μm area. Height measurements were made from the lowest point, shown as dark blue and listed as zero in the legend, to pink and red areas that indicate height. Notice that the number of pits did not grow much from t_0 to t_3 (12 h). Following t_3, the pits began increasing in size.

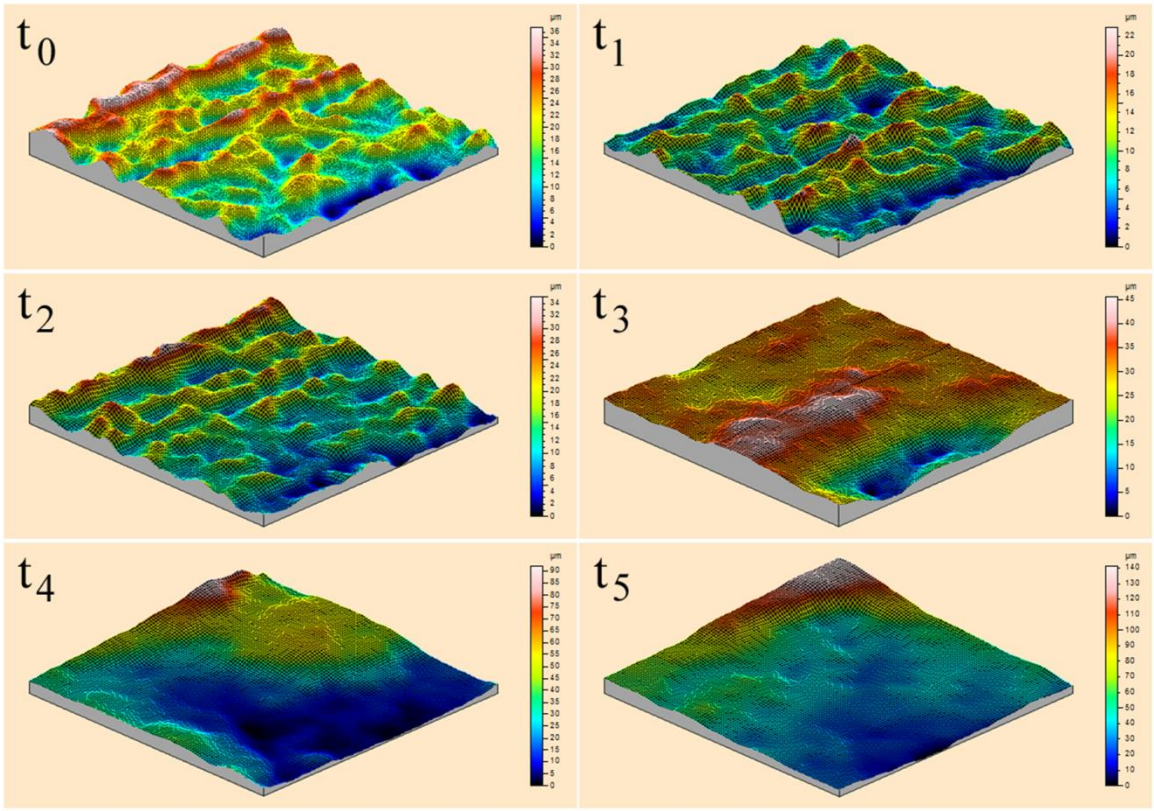

Figure 2.12 3-D Laser Profilometry of the salt spray surface over 60 hours.

All spots were examined over a 30 µm x 30 µm area. Height measurements were made from the lowest point, shown as dark blue and listed as zero in the legend, to pink and red areas that indicate height. Notice that the number of pits initially grew in number from t_0 to t_2 (4 h), while the pits grew in area connecting with neighbors from t_3 to t_5.

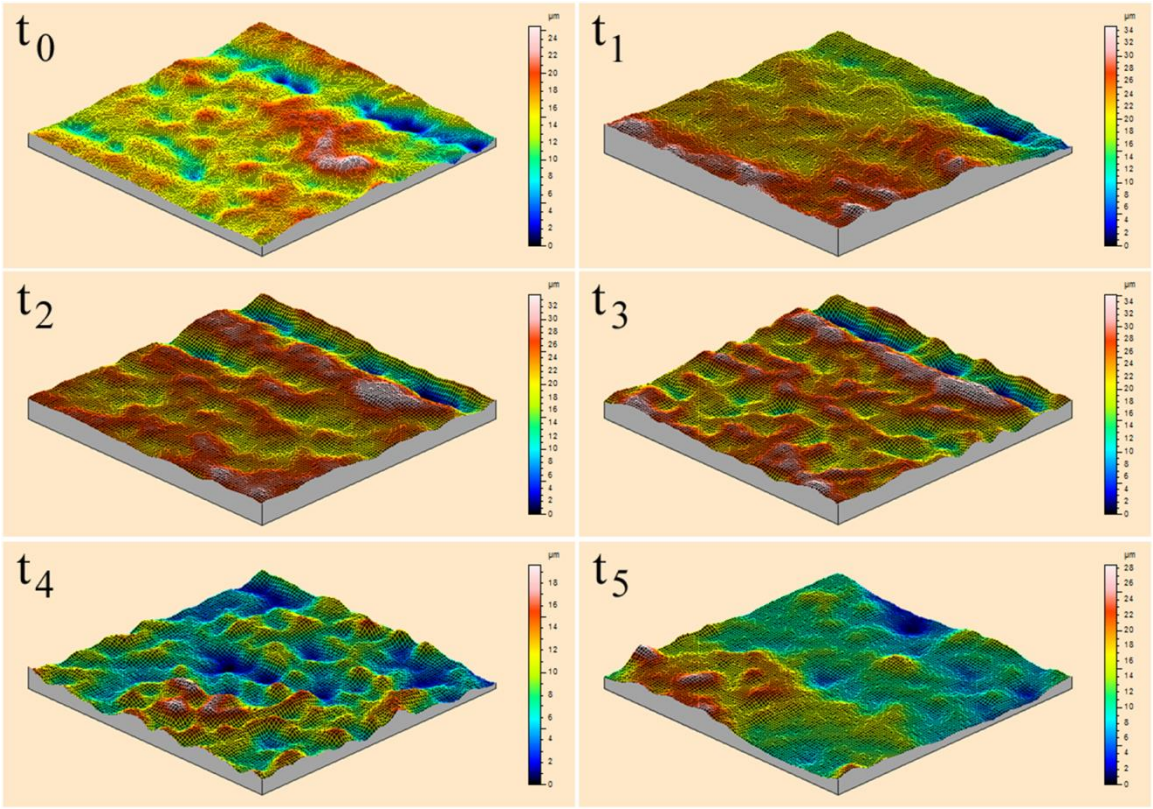

Figure 2.13 3-D Laser Profilometry of the immersion surface over 60 hours.

All spots were examined over a 30 µm x 30 µm area. Height measurements were made from the lowest point, shown as dark blue and listed as zero in the legend, to pink and red areas that indicate height. Notice that the number of pits did not grow much from t_0 to t_3 (12 h). Following t_3, the pits began increasing in size.

Figures 2.14-2.15 are micrographs that show the changes in surface characteristics using micrographs over 60 hours for both the salt spray environment and the immersion environment, respectively. The figures are arranged to show the changes between the surfaces covering an area of 1 mm by 1 mm with the scale bars of 1000 µm for each of the times examined, where $t_0 = 0$, $t_1 = 1$ h, $t_2 = 4$ h, $t_3 = 12$ h, $t_4 = 36$ h, and $t_5 = 60$ h, and to show the differences in the pits between the salt spray and immersion environments. The black lines running horizontal in the micrographs on both samples are a result of the extrusion process. The surfaces were not polished to examine the effects of the extruded

condition. When examining the salt spray surface, pits began to form between t_0 and t_2 as shown by the black areas forming on the surface. At t_3, one can see that the pits began to grow in size. Coalescence across the surface was observed at t_4 and t_5. When examining the immersion surface, intergranular corrosion was observed to occur between time t_0 and t_1 indicated by pit growth along grain boundaries. After t_1, general corrosion began to occur at t_2. Following t_2, pitting across the surface was noticeable. The blurry white areas are where NaCl has collected in the pits.

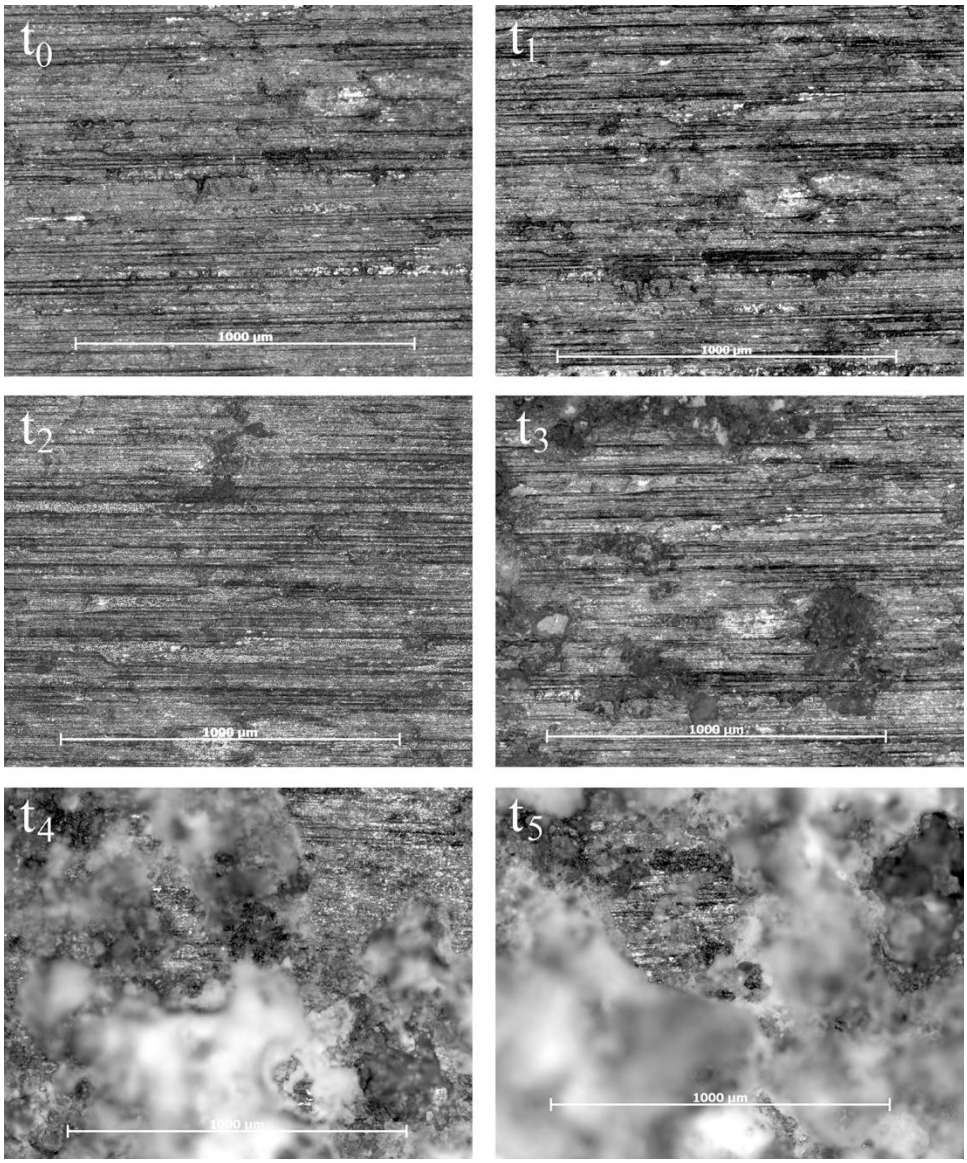

Figure 2.14 Micrographs of the salt spray surface over 60 hours.

All spots were examined over a 1 mm x 1 mm area, with scale bars of 1000 µm each. The darker areas indicate pit formation and coalescence, while the lighter areas indicate surfaces closer to the light and those affected by general corrosion. Notice that the pits grew in number through t_2 (4 h), decreasing in number following t_2. Also, notice the pits grew in area through t_5 (60 h).

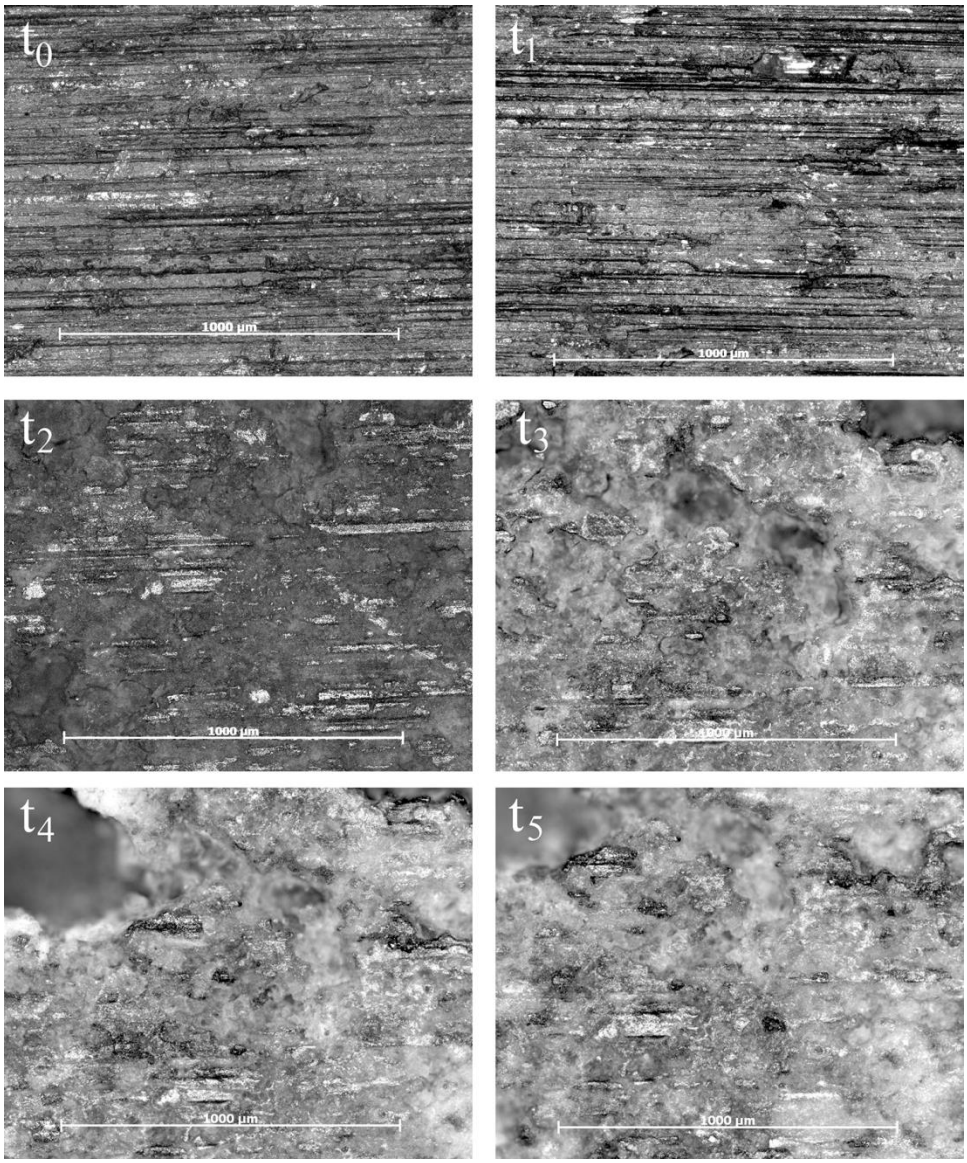

Figure 2.15 Micrographs of the immersion surface over 60 hours.

All spots were examined over a 1 mm x 1 mm area, with scale bars of 1000 µm each. The darker areas indicate pit formation and coalescence, while the lighter areas indicate surfaces closer to the light and those affected by general corrosion. Notice that the pits grew in number and area through t_1 (1 h), while decreasing in number following t_1 but increasing in size and depth through t_5.

2.4 Discussion

2.4.1 General Corrosion

Figures 2.1 and 2.2 show the overall changes within the bulk material of the specimens based on the two environments, immersion and salt spray. The weight change, illustrated in Figure 2.1, shows that the specimens exposed to the immersion environment experienced a decrease in weight. The continuous presence of water allowed the corrosion by-products to dissolve, as $Mg(OH)_2$ is water soluble, and also kept the salt suspended. The inability of the pit debris and salt residuals to remain on the surface meant that material was removed (general corrosion) from the Mg surfaces, leading to a decrease in weight. Conversely, the salt spray environment coupons experienced an increase in weight. For this change, more salt residuals or corrosion by-products are left on the surface than $Mg(OH)_2$ being removed from the surfaces after drying. An approximate one to one "replacement" of $Mg(OH)_2$ and NaCl, as a mole of each weighs 58.22 g and 58.44 g, respectively [51], explains the minimal change in the weight of the salt spray coupons from t_0-t_2. Once pits began to grow in size, more NaCl was able to collect within the pits. In fact, an increase in the presence of salt on the surface was observed at t_4 and t_5 in Figure 2.14. The coupons were not chemically cleaned, only rinsed with distilled water, to ensure that the surface remained unchanged. The cleaning method could allow corrosion by-products and salt to remain attached to the surface increasing the weight. In addition, because the material was extruded, "channels" were observed on the virgin surface (Figure 2.12). The channels and the pits formed during the tests are areas in which the salt could collect and subsequently, cause the weight to increase.

The thickness changes of the specimens shown in Figure 2.2 confirm that general corrosion took place on surfaces exposed to both environments. Although both trends show a decrease in thickness as a function of time, the salt spray surfaces lost approximately three times as much thickness as compared to the immersion environment (approximately 0.1 mm compared to 0.03 mm, respectively). In this study, qualitative observations showed more pitting corrosion along the edges of the salt spray coupons when compared to immersion coupons. This increase in corrosion along the edges could lead to measurement errors. The salt spray coupons were hung at a 20° angle to the horizontal, which allowed the water containing salt to run off the edges and down to the bottom of the coupons. The high concentration of chloride ions increases the rate in which pitting can occur while drying, thereby reducing the thickness. Those measurement errors, due to caliper placement, would lead to a greater thickness loss than on the immersion samples, where general corrosion took place equally on the entire surface.

2.4.2 Pitting Corrosion

In other Mg literature, localized corrosion is the most commonly used terminology to study pit evolution [15]. Localized corrosion includes both pitting corrosion and intergranular corrosion [13]. For this research, localized corrosion is split into pitting corrosion and intergranular corrosion for the sake of model development and implementation and will be referred to individually for the remainder of the discussion. The individual pit characteristics of depth, surface area, and volume are shown in Figures 2.3-2.5, respectively. When looking at the pit depth changes (Figure 2.3) for the two environments, the slight increasing and decreasing trends of the salt-spray and immersion

environments, respectively, on the graph show that general corrosion occurred. Once the surface had been corroded away, pits then began to grow deeper into the coupons surfaces. One can notice that the salt spray mean and max pit depth started to increase at a greater rate approximately 15 hours after corroding away the surface and reacting with the bulk material. The immersion environment trends slightly decreased over the 60 hours of testing. The decreasing trends indicated that general corrosion was the major factor in the immersion environment. However, the large error bars at t_4 and t_5 show that the pit depth varied greatly, indicating that new pits formed with small pit depths, while the existing pits grew deeper. The pit surface area (Figure 2.4) for both environments showed a constant increase throughout the 60 hours. The two trend lines are almost identical indicating that the areas of the pits were increasing at approximately the same rate in both environments. Unlike the pit depth, large variations at t_3 and t_5 showed up only in the immersion environment. These variations are due to the averaging of the new pits, which have smaller areas, and the well-established pits, which have larger areas. Looking at the pit volume graph (Figure 2.5), one can see that a very small increase occurs throughout the exposure time. Between t_4 and t_5, the salt spray environment had a harsher effect on the surface than the immersion environment.

Generally speaking, major differences are observed between the salt spray surfaces and the immersion surfaces for Figure 2.3-2.5. The differences between the pit characteristics on the two surfaces can be explained by the exposure environment. For the salt spray environment, chloride ions were only exposed to the surface briefly during the salt spray phase of the cycle compared to the immersion surfaces. The chloride ions could react with the surface only during that cycle phase. Following a “pollution” cycle,

the wet phase (humidity) introduced salt-free water to the surface. The humidity phase helped the pits grow, as well as aided in the removal of residual chloride ions and loose Mg from the surface. The humid environment causes condensation, which removed some chloride ions, but the condensed water could also diffuse into the pits without being able to diffuse out. The presence of the water and chloride ions continued to react with the Mg even during the drying phase, allowing the pits to grow unabated, even without additional chloride ions. The drying phase also stopped general corrosion and dried any corrosion and pit debris onto the surface, trapping the chloride ions inside the pits. The chloride ions continued to react underneath the pit debris, leading to an increase in pit characteristics due to the autocatalytic reaction [70]. On the other hand, immersion surfaces were continually exposed to both chloride ions and water which enabled pits to form wherever possible. This means that the pit depth would not be affected as much compared to the salt spray environment which is demonstrated by Figure 2.3. The smaller pit characteristics on the immersion surface as compared with the salt spray surface are a result of this interaction.

2.4.3 Surface Characteristics and Modeling

Figures 2.6-2.9 show the changes in the surface characteristics of pit number density, pit area, NND, and ICAF, respectively. These surface characteristics are used to examine the evolution of corrosion damage in a similar manner to the model developed for mechanical energy dissipation [35]. Also, the corrosion model by Martin *et al*. [49] will be later modified to describe the damage associated with extruded AZ31.

When comparing Figures 2.6 and 2.7, one can see that the pit number density (η_p – Figure 2.6) and pit area (v_p – Figure 2.7) are inversely related. As the pit number

density decreases due to pit coalescence, the pit area increases. Looking at the pit number density graph, the data points initially increase for both the salt spray and immersion environments although the trend decreases. This happens because when the coupons are exposed to the corrosive environment, more pits form in a finite area on the surface. Throughout the exposure time, pits begin to grow until they approach nearby pits. Eventually, these pits coalesce with each other, decreasing the pit number density. The pit number density is also inversely related to the NND (*c* – Figure 2.8). As more pits become present on the surface, the distance between the pits decreases. So as the pits grow larger, the distance between the pits decreases, causing the NND to decrease. Once the closest pits coalesce, forming one larger pit, the NND increases, as the distance between the newly formed, large pits increases.

In addition to the NND, another function related to the coalescence of the pits is the ICAF (Figure 2.9). The ICAF is related to the coalescence of the pits, because pits typically form along the α-phase Mg grains and the β-phase ($Mg_{17}Al_{12}$) precipitate boundaries [71]. As the pits grow and coalesce, they would degrade the area separating the grains and the β-phase precipitate boundaries, increasing intergranular corrosion area fraction, or the portion of the area covered by the corrosion of the α-phase Mg grain – β-phase precipitate boundary. The trend for the ICAF is a second-order polynomial increasing until about 25 and 35 hours before decreasing for the immersion and salt spray environments, respectively. If one were to take a look at ICAF graph, one can notice a sharp increase from 0-4 hours showing that the immersion environment increased at a higher rate. This indicates that intergranular corrosion was a dominating factor early in the tests. With intergranular corrosion dominating, an increase of pits are noticed on the

surfaces, which explains the initial decrease in the NND trends. The reduction and then decreasing trends of the ICAF indicates that pit growth away from the grain boundaries began to dominate. One can notice this when comparing Figure 2.3 (Pit Depth) and Figure 2.9 from approximately 12 hours until the end of the exposure time. Also, when comparing the thickness (Figure 2.2) and ICAF (Figure 2.9), one can notice that as the intergranular corrosion rate increased, the thicknesses of the coupons for both environments decreased. After the intergranular and general corrosion mechanisms have removed some of the shallow pits, the thickness does not change much but deeper pits (Figure 2.3) are noticed.

When comparing the pit number density between the immersion and salt spray environments (Figure 2.6), the salt spray coupons had a slightly lower number of pits present during the exposure time due to the cyclic nature of the Q-Fog test chamber. In Figure 2.6, it is evident that the pit number density in the immersion environment was slightly greater than the salt spray environment. Like the pit characteristics in Figures 2.3-2.5, the pit number density is a function of the exposure environment. The immersion environment enables pit nucleation during the entire exposure time. Pit nucleation in the salt spray environment can only happen when the Q-Fog cycles through the saltwater spray cycle. The saltwater spray provides the chloride ions necessary for pitting corrosion but is then followed by the humidity cycle, which allows for the development of a protective $Mg(OH)_2$ film without the chloride ions necessary for pit initiation. The drying cycle then stops general corrosion, but the pit debris present allows for the pits to continue growing through this part of the cycle, due to the autocatalytic nature of pit formation [49,70].

When comparing the pit area between the immersion and salt spray environments, one can notice that the salt spray environment trend was only slightly below the immersion environment trend (Figure 2.7). The lower deviation between the two trends is observed at 12 hours into the experiment. During that time, coalescence of pits was taking place at a higher rate on the immersion surfaces compared to the salt spray surfaces. The pit area is based on two main factors: pit number density and pit size. Pit area combines the small area covered by the individual pits nucleating at various exposure times and the larger area covered by the well-formed pits that are growing radially outwards. The immersion environment allows for the higher pit number, thereby allowing for higher pit area. While the pit area is higher on the immersion surface, though, general corrosion would reduce some of the pit area. The pit area on the salt spray surface is similar to the immersion surface, even with a smaller pit number density. Unlike the immersion environment, where general corrosion can reduce the size of the pits growing outward, general corrosion cannot reduce the size of the pits on the salt spray surface as easily, because of the drying phase. This means that the pits grow larger on the salt spray surface, thereby offsetting the smaller number of pits. However, because of the smaller number of pits on the salt spray surface, even as these pits get larger, the pit area would still be larger on the immersion surface.

When comparing the NND (Figure 2.8) between the two environments, one can see that initially the distance between pits was approximately the same for both the salt spray and immersion environments. As time progresses through the tests, the distance between the pits on the salt spray surfaces increased faster than the pits on the immersion environment surfaces. The increase in distance between the pits demonstrates that the

salt spray surface is dominated by pit growth, as there are fewer pits on the salt spray surface, as shown in Figures 2.10, 2.12, and 2.14. In Figure 2.12, one can notice that between t_4 and t_5 the pit eventually grows from a depth of approximately 90 μm to 140 μm. Figure 2.14 shows that pits were trying to form around t_2 but then become very noticeable around t_3. By t_4 and t_5, larger pits have consumed most of the surface examined by the microscope. When looking at the immersion environment, there were more pits to start with, so the pits were closer together shown in Figures 2.11, 2.13, and 2.15. The micrographs in Figures 2.15 confirm that the immersion surface experienced a higher number of pits forming throughout the experiments. When comparing the micrographs (Figure 2.14 and 2.15) at t_2, one can see that the immersion surface has darker areas, which indicate more pit areas than the salt-spray surface. Also, we notice larger pits forming at t_3 on the immersion surface compared to t_4 on the salt spray surfaces. Even as the pits coalesced, thereby increasing the distance between them, there were still more pits, so the distance between the pits would be less than the salt spray surface. The increase in distance between the pits on the immersion surface show that coalescence is not dominated by either pit number density or pit area, but instead is a function of both.

2.4.4 Comparison between extruded AZ31 and AZ61

When comparing the data from extruded AZ31 presented here with data from extruded AZ61 previously published [51], one can see that there are many differences between both the individual pit characteristics and the surface characteristics used in developing the model. When comparing the individual pit characteristics of maximum and mean pit depth, pit surface area, and pit volume, one can see that the pit depth was

larger on the AZ31 surfaces as compared to the AZ61, except at the final time for the immersion surface of AZ31 [51]. When examining the pit surface area, one can see that the immersion surface of AZ31 has the highest pit surface area while the immersion surface of AZ61 has the lowest pit surface area [51]. The pit surface area on the salt spray surfaces alternates between the two AZ alloys, with AZ31 ending with a slightly higher pit surface area than AZ61 at 60 h [51]. Lastly, when comparing the pit volume, both AZ31 surfaces had larger pit volumes than the AZ61 surfaces [51]. Unlike the pit depth and pit surface area, though, the salt spray surfaces followed almost the same second-order trend, with close to 4000 μm^3 difference throughout the entire experimentation time, while the immersion surfaces followed almost the same linear trend [51]. The differences in pit depth, pit surface area, and pit volume, which were all larger on the AZ31 surfaces as compared to the AZ61 surfaces, are likely attributed to the composition of the alloy, as the extruded surface was the same. It has been shown that up to 9% Al increases the corrosion resistance of Mg [13,15]. Because Al works to decrease corrosion when it is finely divided, and increases corrosion when it is clustered [13,15,18,71,72], one would suspect that a higher percentage of Al, 6% in AZ61 versus 3% in AZ31, would lead to a higher corrosion resistance because more Al is present to be finely divided throughout the grain boundaries and within the grains. This research supports this supposition, demonstrated by the smaller pits that formed on the AZ61 alloy surfaces.

In addition to the individual pit characteristics, the surface characteristics of pit number density, pit area, NND, and intergranular corrosion area fraction are important in determining how these to AZ alloys corrode over time. When looking at the pit number

density, one can see that both AZ61 surfaces had much higher amounts of formed pits than the AZ31 surfaces [51]. Unlike AZ31 surfaces, which saw a decrease in pit number density throughout the entire 60 hours of test, the AZ61 surfaces initially increased until approximately 30 h before decreasing to 60 h [32]. The final AZ61 salt spray surface ended at approximately the same pit number density as both AZ31 surfaces, while the final AZ61 immersion surface ended with a much higher pit number density than the other three surfaces [51]. When looking at the pit area, which is the 2-D area examined on the micrographs as compared to the 3-D surface area produced by the Talysurf and considered an individual pit characteristics, both AZ31 surfaces had much higher pit areas than both AZ61 surfaces [51]. The pit area on the AZ31 surfaces were larger than those on AZ61 surfaces by an initial value of 1000 μm^2, which increased to a final difference of 16500 μm^2 [51]. The NND for AZ31 was smaller for both surfaces as compared to the AZ61 surfaces [71]. Finally, comparing ICAF, one can see that the AZ31 surfaces have slightly higher amounts of intergranular corrosion than the AZ61 surfaces, although both surfaces end at approximately the same percentage after 60 h [51]. The AZ31 surfaces start off initially much higher than the AZ61 surfaces and decrease to 60 h while the AZ61 surfaces increase to 60 h [51].

As with the individual pit characteristics, the percentage of Al plays a role in the amount of corrosion experienced by the AZ31 surfaces versus the AZ61 surfaces. The AZ61 surfaces, which had larger pit number densities but smaller pit areas, experienced an attack on the surfaces by the chloride ions but were able to withstand it due to the 6% Al, resulting in a number of pits formed but those pits were unable to grow. The AZ31 surfaces, on the other hand, had a small number of pits form, but those pits were able to

grow unabated due to the small amount of Al present in the alloy. The effect of low percentages of Al can best be detailed when comparing the NNDs between the two alloys. One would suspect that the NND of the two AZ alloys should be similar, since the NND measures the distance between pits, combining the pit number density, higher on the AZ61 surfaces, with the pit area, higher on the AZ31 surfaces. Because the NND is lower on the AZ31 surfaces, meaning the pits are closer together, this indicates that the area covered by the pits formed on the AZ31 surfaces are much larger than the number of pits that formed on the AZ61 surfaces. The NND demonstrates that the AZ31 surfaces experienced more corrosion than the AZ61 surfaces.

Lastly, when comparing ICAF, the higher amounts of corrosion experienced by AZ31 is demonstrated, as the AZ31 surfaces experienced more ICAF throughout the experimentation time. Since AZ31 could not withstand the corrosive attack, the ICAF eventually was reduced as general corrosion removed the surface of the material, meaning the ICAF decreased over time. Since AZ61 was able to withstand the corrosive attack more easily, the ICAF increased because not as much surface from the material was removed, meaning the ICAF was not affected by general corrosion. The differences between both the individual pit characteristics and the surface characteristics strongly support that the percentage of Al plays an important role in the ability of the pits to form, grow, and damage the material. Within this research, it has been shown that the higher the percentage of Al, the better the corrosion resistance of the AZ alloy, regardless of environment.

2.5 Conclusions

This research focused on the differences in the corrosion mechanisms on an extruded AZ31 Mg alloy under two different environments: cyclical salt spray and immersion. The corrosion mechanisms being examined at various times were general corrosion, pitting corrosion, and intergranular corrosion. The general corrosion rate with respect to thickness was greater by approximately three times for the salt spray when compared to the immersion surfaces, likely due to some measurement error. The pit and surface characteristics on the salt spray surfaces were affected by the cycling of the water, which did not continuously remove the pit debris, and encouraged the trapping of chloride ions, which allowed the pits to grow deeper and wider by the end of the 60 hours. The pit surface area and pit number density rates were greater for the immersion surfaces than the salt spray surfaces, due to the continuous presence of water which allowed the pits to form and grow more easily. The NND of pits was higher for the salt spray environment than the immersion environment. The immersion surface had a lower NND, because of the higher pit number density on the surfaces. The intergranular corrosion mechanism shows to dominate early in the immersion and salt spray environments. The ICAF for the immersion environment was initially higher than the salt spray environment, but around 48 hours and on, the salt spray ICAF was higher.

CHAPTER III

FORMULATION OF A MACROSCALE CORROSION DAMAGE INTERNAL STATE VARIABLE MODEL

3.1 Introduction

To capture the corrosion behavior in a macroscale continuum model, the kinematics, thermodynamics, and kinetics of the ISVs must be coupled together to have a consistent theory that captures the entire process. The proposed model will capture the degradation effects as a scalar variable. A scalar damage variable which represents a strength decrease was first introduced by Kachanov [73]. Kachanov postulated that the loss of stiffness and integrity attributed to micro cracks can be measured by a deterministic, macroscopic damage parameter and its change may be defined by the evolution of an ISV that depends on the expected value of the micro-defect density [73,74]. Essentially, the damage state can be thought of as the void volume fraction (or void area fraction).

Although the complex interactions of pit nucleation, pit growth, and pit coalescence as related to surface effects are recognized, no hydrogen bulk effects are addressed. For example, in a deleterious corrosive environment, hydrogen ions can diffuse into the Mg lattice and induce what is often called HE [75,76]. By reviewing prior work [53], the overall reaction for the corrosion of pure Mg is shown as

$$Mg + 2H_2O \rightarrow Mg(OH)_2 + H_2 \qquad \text{(Eq. 3.1)}$$

This shows the production of hydrogen gas from the system which, in its ionic state, in-turn can absorb, and desorb, into the matrix of the Mg [76]. General corrosion under stress is quite different from stress-free conditions [77]. The combined action of corrosion and stress can cause premature failure compared to the failure rate of the two loading cases separately. The conceptual interrelationship of corrosion, stress effects, and HE play a huge role in the understanding all of the key mechanisms. The most serious practical situation is when all three phenomena interact. The prominent damage mechanism explaining the interaction of Mg alloys under simultaneous corrosion and stress environments is called stress corrosion cracking (SCC) [75]. SCC is broken down into two main forms: intergranular stress corrosion cracking (IGSCC) and transgranular stress corrosion cracking (TGSCC) [78,79]. IGSCC is typically caused by a continuous second phase along grain boundaries where TGSCC is caused by an interaction of hydrogen with the microstructure [78]. The transformation in physical-mechanical properties and microstructure of a solid under the influence of chemical reactions, including HE, which proceed on specimen surfaces causing additional dislocation flux is called the chemomechanical effect [80]. Hence, the influence of active and aggressive environment on mechanically induced stress manifests itself through the influence on the dislocation evolution observed in the form of chemomechanical effect [80]. The kinetics behind this phenomenon will not be addressed in this study.

The research presented here is the first of its kind in creating a physically-based macroscale ISV inelasticity model for corrosion. The corrosion ISVs are essentially added to the thermomechanical plasticity-damage model of Bammann [32–34] and

Horstemeyer [35,40] but includes electrochemical environments using conservation laws and empirical relationships. The kinematics, thermodynamics, and kinetics of the surface corrosion progression are introduced in a self-consistent manner.

3.2 Kinematics

From standard continuum mechanics, all equations are written in the current configuration. Any motion, $\boldsymbol{x}$, maps a particle from its initial position, $\boldsymbol{X}$, in the reference configuration to its position in the current configuration can be represented by the deformation gradient, $\boldsymbol{F}$.

$$\boldsymbol{F} = \frac{\partial \boldsymbol{x}}{\partial \boldsymbol{X}} \qquad \text{(Eq. 3.2)}$$

The deformation gradient assumes a sufficient continuity, where the local deformation at $\boldsymbol{X}$ is characterized as the gradient of the motion, which is a second order, two-point tensor. From here the Green elastic strain tensor, $\boldsymbol{E}$, or Lagrangian strain tensor, is defined with respect to the reference coordinates as

$$\boldsymbol{E} = \frac{1}{2}\left(\boldsymbol{F}^{T}\boldsymbol{F} - \boldsymbol{I}\right) \qquad \text{(Eq. 3.3)}$$

where $\boldsymbol{I}$ is the identity matrix. The Almansi strain tensor, $\boldsymbol{B}$, or Eulerian strain tensor, can also be expressed with respect to current coordinates as

$$\boldsymbol{B} = \frac{1}{2}\left(\boldsymbol{I} - \left(\boldsymbol{F}\boldsymbol{F}^{T}\right)^{-1}\right) \qquad \text{(Eq. 3.4)}$$

For small strains, $\boldsymbol{E} = \boldsymbol{B}$ but will differ once the rotational degrees of freedom start to influence the strain response. The two strain tensors give a measure of how the lengths

of line elements and angles between line elements change between configurations. When adding inelasticity into the kinematics for large strains, one can follow closely the original works of Davison et al. [81], Bammann and Aifantis [22], and Horstemeyer et al. [35]. The kinematics of motion combines elastic straining, inelastic flow, and formation and growth of damage, which is captured by the multiplicative decomposition of the deformation gradient. The deformation can be decomposed into the elastic, $\boldsymbol{F}_e$, damage, $\boldsymbol{F}_\phi$, and plastic, $\boldsymbol{F}_p$, deformation gradients given as the following,

$$\boldsymbol{F} = \boldsymbol{F}_e \boldsymbol{F}_\phi \boldsymbol{F}_p \qquad \text{(Eq. 3.5)}$$

Eq. (3.5) assumes that the motion of the body is described by a smooth displacement function. This precludes the initiation of discrete failure surfaces but still allows a continuum description of damage. The elastic deformation gradient, $\boldsymbol{F}_e$, represents lattice displacements from equilibrium. The volumetric inelastic deformation gradient, $\boldsymbol{F}_\phi$, represents a continuous distribution of corrosion and mechanical damage throughout the specimen. By this notion, the damage deformation gradient then can be decomposed by the chemical, $\boldsymbol{F}_{\phi_c}$, and mechanical , $\boldsymbol{F}_{\phi_m}$, deformation gradients as shown in the following:

$$\boldsymbol{F}_\phi = \boldsymbol{F}_{\phi_c} \boldsymbol{F}_{\phi_m} \qquad \text{(Eq. 3.6)}$$

The finite strain deformation gradient (Eq. 3.5) can then be rewritten as

$$\boldsymbol{F} = \boldsymbol{F}_e \boldsymbol{F}_{\phi_c} \boldsymbol{F}_{\phi_m} \boldsymbol{F}_p \qquad \text{(Eq. 3.7)}$$

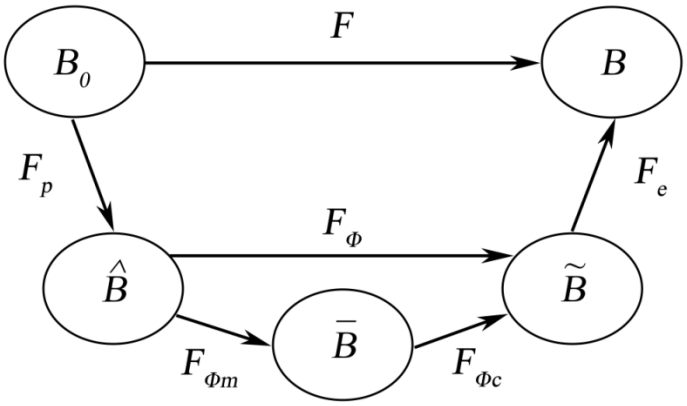

Figure 3.1 Multiplicative decomposition of the deformation gradient into the plastic, chemical damage, mechanical damage, and elastic parts.

Figure 3.1 shows the modified finite strain deformation gradient described in Eq. (3.7). The elastic deformation gradient is written first because we want our material to unload elastically through $\boldsymbol{F}_e^{-1}$ to an inelastically damaged material state. The Jacobian, J, of the deformation gradient can be written as

$$J = \det \boldsymbol{F} = \det \boldsymbol{F}_p \det \boldsymbol{F}_{\phi_m} \det \boldsymbol{F}_{\phi_c} \det \boldsymbol{F}_e \qquad \text{(Eq. 3.8)}$$

The Jacobian of the volumetric damage deformation gradient is related to the change in volume or change in density for constant mass [35] as

$$J_\phi = \det \boldsymbol{F}_\phi = \frac{\tilde{V}}{\hat{V}} \qquad \text{(Eq. 3.9)}$$

and must be positive. The change in volume from the reference configuration (B_0) to the intermediate configurations ($\bar{B}$ and $\hat{B}$) or the current configuration (B) is $\hat{V} = V_0 + V_{voids} + V_c$. The volume in the reference configuration is given by V_0. In transforming the configuration from B_0 to $\bar{B}$, an added volume from the corrosion

effects, V_c, is introduced to the total volume. Damage can be defined as the ratio of the change in volume of an element in the elastically unloaded state $\widetilde{B}$ from its volume in the initial reference state to its volume in the elastically unloaded state; here we assume that elastic volumetric deformation is minimal compared to the corrosion and thus assume that the volume does not change from the intermediate configuration and current configuration,

$$\phi = \frac{V_c}{\widetilde{V}} \qquad \text{(Eq. 3.10)}$$

From this definition, we get

$$V_0 = (1-\phi)\widetilde{V} \qquad \text{(Eq. 3.11)}$$

where now the determinant is determined by the damage parameter as

$$\det \boldsymbol{F}_{\phi} = \frac{1}{1-\phi} \qquad \text{(Eq. 3.12)}$$

Consequently, the restriction that damage is assumed to produce isotropic dilatation gives the volumetric part of the deformation gradient as

$$\boldsymbol{F}_{\phi} = \frac{1}{(1-\phi)^{1/3}}\boldsymbol{I} \qquad \text{(Eq. 3.13)}$$

The total strain can be obtained by pulling the intermediate configurations all back to the configuration $\boldsymbol{x}$

$$\boldsymbol{E} = \boldsymbol{E}_e + \boldsymbol{E}_{\phi_c} + \boldsymbol{E}_{\phi_m} + \boldsymbol{E}_p \qquad \text{(Eq. 3.14)}$$

The corresponding Lagrangian strain tensors may be written as

$$\boldsymbol{E} = \frac{1}{2}(\boldsymbol{C} - \boldsymbol{I}),\ \boldsymbol{E}_p = \frac{1}{2}(\boldsymbol{C}_p - \boldsymbol{I}),\ \widetilde{\boldsymbol{E}}_{\phi_c} = \frac{1}{2}(\overline{\boldsymbol{C}}_{\phi_c} - \boldsymbol{I}),$$
$$\overline{\boldsymbol{E}}_{\phi_m} = \frac{1}{2}(\widetilde{\boldsymbol{C}}_{\phi_m} - \boldsymbol{I}),\ \hat{\boldsymbol{E}}_e = \frac{1}{2}(\hat{\boldsymbol{C}}_e - \boldsymbol{I}) \qquad \text{(Eq. 3.15)}$$

where the stretch tensors, $\boldsymbol{C}$, are defined as

$$\boldsymbol{C} = \boldsymbol{F}^T\boldsymbol{F},\ \boldsymbol{C}_p = \boldsymbol{F}_p^T\boldsymbol{F}_p,\quad \widetilde{\boldsymbol{C}}_{\phi_c} = \boldsymbol{F}_{\phi_c}^T\boldsymbol{F}_{\phi_c},$$
$$\overline{\boldsymbol{C}}_{\phi_m} = \boldsymbol{F}_{\phi_m}^T\boldsymbol{F}_{\phi_m},\quad \hat{\boldsymbol{C}}_e = \boldsymbol{F}_e^T\boldsymbol{F}_e \qquad \text{(Eq. 3.16)}$$

Each Cauchy-Green deformation tensors in Eq. 16 can undergo a spectral decomposition of the form

$$\boldsymbol{C} = \sum_{i=1}^{3} \lambda_i^2 \boldsymbol{n}_i \otimes \boldsymbol{n}_i \qquad \text{(Eq. 3.17)}$$

where λ_i is each positive eigenvalue which corresponds to each orthonormal eigenvector, $\boldsymbol{n_i}$. The positive eigenvalues represent the principle stretches. Each deformation gradient has a polar decomposition of the form

$$\boldsymbol{F}_\bullet = \boldsymbol{R}_\bullet \boldsymbol{U}_\bullet \qquad \text{(Eq. 3.18)}$$

where $\boldsymbol{R}$ is the rotation tensor, $\boldsymbol{U}$ is the right stretch tensor, and $(\bullet)$ can be any of the configuration $(e,\ \phi_c\ ,\ \phi_m\ , p)$. The relationship between $\boldsymbol{C}$ and $\boldsymbol{U}$ is

$$\boldsymbol{U} = \sqrt{\boldsymbol{C}} = \sum_{i=1}^{3} \lambda_i \boldsymbol{n}_i \otimes \boldsymbol{n}_i \qquad \text{(Eq. 3.19)}$$

The velocity gradient associated with the deformation gradient in the current configuration separated into the elastic, corrosion, mechanical, and plastic parts is given by

$$\boldsymbol{l} = \dot{\boldsymbol{F}}\boldsymbol{F}^{-1} = \boldsymbol{l}_e + \boldsymbol{l}_{\phi_c} + \boldsymbol{l}_{\phi_m} + \boldsymbol{l}_p \qquad \text{(Eq. 3.20)}$$

where

$$\dot{\boldsymbol{F}} = \dot{\boldsymbol{F}}_e\boldsymbol{F}_{\phi_c}\boldsymbol{F}_{\phi_m}\boldsymbol{F}_p + \boldsymbol{F}_e\dot{\boldsymbol{F}}_{\phi_c}\boldsymbol{F}_{\phi_m}\boldsymbol{F}_p + \boldsymbol{F}_e\boldsymbol{F}_{\phi_c}\dot{\boldsymbol{F}}_{\phi_m}\boldsymbol{F}_p + \boldsymbol{F}_e\boldsymbol{F}_{\phi_c}\boldsymbol{F}_{\phi_m}\dot{\boldsymbol{F}}_p \qquad \text{(Eq. 3.21)}$$

$$\boldsymbol{F}^{-1} = \boldsymbol{F}_p^{-1}\boldsymbol{F}_{\phi_m}^{-1}\boldsymbol{F}_{\phi_c}^{-1}\boldsymbol{F}_e^{-1} \qquad \text{(Eq. 3.22)}$$

This leaves

$$\begin{aligned}\boldsymbol{l} = {} & \dot{\boldsymbol{F}}_e\boldsymbol{F}_e^{-1} + \boldsymbol{F}_e\dot{\boldsymbol{F}}_{\phi_c}\boldsymbol{F}_{\phi_c}^{-1}\boldsymbol{F}_e^{-1} + \boldsymbol{F}_e\boldsymbol{F}_{\phi_c}\dot{\boldsymbol{F}}_{\phi_m}\boldsymbol{F}_{\phi_m}^{-1}\boldsymbol{F}_{\phi_c}^{-1}\boldsymbol{F}_e^{-1} \\ & + \boldsymbol{F}_e\boldsymbol{F}_{\phi_c}\boldsymbol{F}_{\phi_m}\dot{\boldsymbol{F}}_p\boldsymbol{F}_p^{-1}\boldsymbol{F}_{\phi_m}^{-1}\boldsymbol{F}_{\phi_c}^{-1}\boldsymbol{F}_e^{-1}\end{aligned} \qquad \text{(Eq. 3.23)}$$

With the relationship described in Eq. (3.20), this means

$$\boldsymbol{l}_e = \dot{\boldsymbol{F}}_e\boldsymbol{F}_e^{-1}$$

$$\boldsymbol{l}_{\phi_c} = \boldsymbol{F}_e\dot{\boldsymbol{F}}_{\phi_c}\boldsymbol{F}_{\phi_c}^{-1}\boldsymbol{F}_e^{-1}$$

$$\boldsymbol{l}_{\phi_m} = \boldsymbol{F}_e\boldsymbol{F}_{\phi_c}\dot{\boldsymbol{F}}_{\phi_m}\boldsymbol{F}_{\phi_m}^{-1}\boldsymbol{F}_{\phi_c}^{-1}\boldsymbol{F}_e^{-1}$$

$$\boldsymbol{l}_p = \boldsymbol{F}_e\boldsymbol{F}_{\phi_c}\boldsymbol{F}_{\phi_m}\dot{\boldsymbol{F}}_p\boldsymbol{F}_p^{-1}\boldsymbol{F}_{\phi_m}^{-1}\boldsymbol{F}_{\phi_c}^{-1}\boldsymbol{F}_e^{-1}$$

As with the strain tensor, similar additive equation holds for the velocity gradient with respect to every configuration. By pulling back the above equation through the inverse of the elastic deformation gradient, the velocity gradient in the intermediate configuration results,

$$\tilde{\boldsymbol{l}} = \tilde{\boldsymbol{l}}_e + \tilde{\boldsymbol{l}}_{\phi_c} + \tilde{\boldsymbol{l}}_{\phi_m} + \tilde{\boldsymbol{l}}_p \qquad \text{(Eq. 3.24)}$$

where

$$\tilde{\boldsymbol{l}}_e = \boldsymbol{F}_e^{-1}\dot{\boldsymbol{F}}_e$$

$$\tilde{\boldsymbol{l}}_{\phi_c} = \dot{\boldsymbol{F}}_{\phi_c} \boldsymbol{F}_{\phi_c}^{-1}$$

$$\tilde{\boldsymbol{l}}_{\phi_m} = \boldsymbol{F}_{\phi_c} \dot{\boldsymbol{F}}_{\phi_m} \boldsymbol{F}_{\phi_m}^{-1} \boldsymbol{F}_{\phi_c}^{-1}$$

$$\tilde{\boldsymbol{l}}_{p} = \boldsymbol{F}_{\phi_c} \boldsymbol{F}_{\phi_m} \dot{\boldsymbol{F}}_{p} \boldsymbol{F}_{p}^{-1} \boldsymbol{F}_{\phi_m}^{-1} \boldsymbol{F}_{\phi_c}^{-1}$$

The velocity gradient then can be decomposed into skew, $\boldsymbol{w}$, and symmetric, $\boldsymbol{d}$, parts in any configuration

$$\boldsymbol{l} = \boldsymbol{d} + \boldsymbol{w} \qquad \text{(Eq. 3.25)}$$

where

$$\boldsymbol{d} = sym(\boldsymbol{l}) = \frac{1}{2}\left(\boldsymbol{l} + \boldsymbol{l}^T\right), \qquad \boldsymbol{w} = skew(\boldsymbol{l}) = \frac{1}{2}\left(\boldsymbol{l} - \boldsymbol{l}^T\right)$$

The volumetric part of the velocity gradient is then given by

$$\tilde{\boldsymbol{l}}_{\phi} = \dot{\boldsymbol{F}}_{\phi} \boldsymbol{F}_{\phi}^{-1} = \frac{\dot{\phi}}{3(1-\phi)} \boldsymbol{I} \qquad \text{(Eq. 3.26)}$$

which defines the volumetric rate of deformation as

$$\boldsymbol{d}_{\phi} = \frac{\dot{\phi}}{3(1-\phi)} \boldsymbol{I} \,. \qquad \text{(Eq. 3.27)}$$

The trace of the volumetric part, Eq. (3.27), is given as

$$tr\left(\boldsymbol{d}_{\phi}\right) = \frac{\dot{\phi}}{(1-\phi)}, \qquad \text{(Eq. 3.28)}$$

so that the damage parameter directly relates to the volumetric rate of deformation. The elastic rate of deformation relates to the volumetric rate of deformation by the additive decomposition of the deformation rates,

$$\boldsymbol{d}_e = \boldsymbol{d} - \boldsymbol{d}_\phi - \boldsymbol{d}_p . \qquad \text{(Eq. 3.29)}$$

Similarly, the rotation rates of deformation would be

$$\boldsymbol{w}_e = \boldsymbol{w} - \boldsymbol{w}_\phi - \boldsymbol{w}_p \qquad (30)$$

Considering that corrosion will only induce inelastic volumetric changes not deviatoric inelastic changes, we will assume that no plasticity is occurring. As a result, we can assume for small strains, the anti-symmetric component of the velocity gradient is zero, therefore, the strain rate tensors can be written as:

$$\dot{\boldsymbol{\varepsilon}} = \dot{\boldsymbol{\varepsilon}}_e + \dot{\boldsymbol{\varepsilon}}_\phi + \dot{\boldsymbol{\varepsilon}}_p \qquad \text{(Eq. 3.31)}$$

where $\dot{\boldsymbol{\varepsilon}}_e$, $\dot{\boldsymbol{\varepsilon}}_p$, and $\dot{\boldsymbol{\varepsilon}}_\phi$ are the elastic, plastic and damage-induced volumetric strain, respectively. Based on [35,81], we assume that damage-induced deformation is isotropic, and damage-induced strain may be written as

$$\dot{\boldsymbol{\varepsilon}}_\phi = \frac{1}{3}(1-\phi)^{-1}\dot{\phi}\boldsymbol{I} \qquad \text{(Eq. 3.32)}$$

3.3 Thermodynamics

The First Law of Thermodynamic in the local form is given by Malvern [82],

$$\rho\dot{u} = \boldsymbol{S} : \boldsymbol{d} + \rho r - \nabla \cdot \boldsymbol{q} \qquad \text{(Eq. 3.33)}$$

where u is the internal energy per unit mass, $\boldsymbol{S}$ is the Kirchhoff stress tensor, r is the specific heat generation rate, $\boldsymbol{q}$ is the heat flux vector, and ρ is the density. The First Law can be defined in the intermediate configuration by pushing forward the symmetric part of the velocity gradient to the tilde configuration.

$$\tilde{\rho}\dot{\tilde{u}} = \tilde{\boldsymbol{S}} : \boldsymbol{F}_e^T \boldsymbol{dF}_e + \rho r - \nabla \cdot \boldsymbol{q} \qquad \text{(Eq. 3.34)}$$

For the isothermal deformation being considered, the First Law can be simplified to the following:

$$\tilde{\rho}\dot{\tilde{u}} = \tilde{\boldsymbol{S}} : \boldsymbol{F}_e^T \boldsymbol{dF}_e \qquad \text{(Eq. 3.35)}$$

Also, using a small strain assumption

$$\dot{\tilde{\boldsymbol{E}}}_e = \boldsymbol{F}_e^T \boldsymbol{d}_e \boldsymbol{F}_e = \boldsymbol{F}_e^T \boldsymbol{dF}_e - \tilde{\boldsymbol{d}}_{\boldsymbol{\phi}} - \tilde{\boldsymbol{d}}_p - \left(\tilde{\boldsymbol{l}}^T - \tilde{\boldsymbol{l}}_e^T\right)\tilde{\boldsymbol{E}}_e - \tilde{\boldsymbol{E}}_e\left(\tilde{\boldsymbol{l}} - \tilde{\boldsymbol{l}}_e\right) \qquad \text{(Eq. 3.36)}$$

$$\tilde{\boldsymbol{d}} = \boldsymbol{F}_e^T sym(\tilde{\boldsymbol{l}})\boldsymbol{F}_e = \boldsymbol{F}_e^T \boldsymbol{dF}_e \qquad \text{(Eq. 3.37)}$$

Eq. (3.35) can be written as

$$\tilde{\rho}\dot{\tilde{u}} = \tilde{\boldsymbol{S}} : \boldsymbol{F}_e^T sym(\tilde{\boldsymbol{l}})\boldsymbol{F}_e \qquad \text{(Eq. 3.38)}$$

By employing the ISV formulation of Coleman and Gurtin [38], we can assume an isothermal Helmholtz free energy per unit mass, $\tilde{\psi}$, as the following

$$\tilde{\psi} = \tilde{u}, \quad \dot{\tilde{u}} = \dot{\tilde{\psi}} \qquad \text{(Eq. 3.39)}$$

By rearranging and substituting Eq. (3.36) and (3.39) into Eq. (3.38), we obtain a modified Clausius-Duhem inequality:

$$-\tilde{\rho}\dot{\tilde{\psi}} + \tilde{\boldsymbol{S}} : \left[\dot{\tilde{\boldsymbol{E}}}_e + \tilde{\boldsymbol{d}}_{\boldsymbol{\phi}} + \tilde{\boldsymbol{d}}_p + \left(\tilde{\boldsymbol{l}}^T - \tilde{\boldsymbol{l}}_e^T\right)\tilde{\boldsymbol{E}}_e + \tilde{\boldsymbol{E}}_e\left(\tilde{\boldsymbol{l}} - \tilde{\boldsymbol{l}}_e\right)\right] \geq 0 \qquad \text{(Eq. 3.40)}$$

The free energy, $\tilde{\psi}$, may be defined as a function of a local state that may be characterized by observable variables such elastic strain, $\tilde{\boldsymbol{E}}_e$, a set of *i* number of strain-

like variables, $\widetilde{\boldsymbol{A}}_i$, with ISVs such as thermodynamic displacement caused by damage, ϕ. The power, *n*, describes the strength of damage, or how fast the moduli will degrade.

$$\widetilde{\psi} = \hat{\widetilde{\psi}}(\widetilde{\boldsymbol{E}}_e \widetilde{\boldsymbol{C}}_{\boldsymbol{\phi}_m}^{-\boldsymbol{n}}, \widetilde{\boldsymbol{E}}_e \widetilde{\boldsymbol{C}}_{\boldsymbol{\phi}_c}^{-\boldsymbol{n}}, \widetilde{\boldsymbol{A}}_i) \qquad \text{(Eq. 3.41)}$$

$$\widetilde{\boldsymbol{A}}_i = \widetilde{\varepsilon}_s \widetilde{t}_d, \widetilde{\boldsymbol{\beta}} \widetilde{\boldsymbol{C}}_{\boldsymbol{\phi}_m}^{-\boldsymbol{n}}, \widetilde{\boldsymbol{\beta}} \widetilde{\boldsymbol{C}}_{\boldsymbol{\phi}_c}^{-\boldsymbol{n}} \qquad \text{(Eq. 3.42)}$$

where $\widetilde{t}_d = \dfrac{tr\widetilde{\boldsymbol{C}}_{\boldsymbol{\phi}}}{3}$ and $\widetilde{\varepsilon}_s = b\sqrt{\widetilde{\rho}_s}$. So

$$\widetilde{\psi} = \hat{\widetilde{\psi}}(\widetilde{\boldsymbol{E}}_e \widetilde{\boldsymbol{C}}_{\boldsymbol{\phi}_m}^{-\boldsymbol{n}}, \widetilde{\boldsymbol{E}}_e \widetilde{\boldsymbol{C}}_{\boldsymbol{\phi}_c}^{-\boldsymbol{n}}, \widetilde{\varepsilon}_s \widetilde{t}_d, \widetilde{\boldsymbol{\beta}} \widetilde{\boldsymbol{C}}_{\boldsymbol{\phi}_m}^{-\boldsymbol{n}}, \widetilde{\boldsymbol{\beta}} \widetilde{\boldsymbol{C}}_{\boldsymbol{\phi}_c}^{-\boldsymbol{n}}) \qquad \text{(Eq. 3.43)}$$

Taking the time derivative of $\widetilde{\psi}$ to get the following,

$$\begin{aligned}
\dot{\widetilde{\psi}} = {} & \frac{\partial \widetilde{\psi}}{\partial\left(\widetilde{\boldsymbol{E}}_e \widetilde{\boldsymbol{C}}_{\boldsymbol{\phi}_m}^{-\boldsymbol{n}}\right)} : \dot{\widetilde{\boldsymbol{E}}}_e \widetilde{\boldsymbol{C}}_{\boldsymbol{\phi}_m}^{-\boldsymbol{n}} + \widetilde{\boldsymbol{E}}_e \left(-n\widetilde{\boldsymbol{C}}_{\boldsymbol{\phi}_m}\right)^{(-n-1)} \frac{\partial \widetilde{\psi}}{\partial\left(\widetilde{\boldsymbol{E}}_e \widetilde{\boldsymbol{C}}_{\boldsymbol{\phi}_m}^{-\boldsymbol{n}}\right)} : \widetilde{\boldsymbol{E}}_e \dot{\widetilde{\boldsymbol{C}}}_{\boldsymbol{\phi}_m}^{-\boldsymbol{n}} \\
& + \frac{\partial \widetilde{\psi}}{\partial\left(\widetilde{\boldsymbol{E}}_e \widetilde{\boldsymbol{C}}_{\boldsymbol{\phi}_c}^{-\boldsymbol{n}}\right)} : \dot{\widetilde{\boldsymbol{E}}}_e \widetilde{\boldsymbol{C}}_{\boldsymbol{\phi}_c}^{-\boldsymbol{n}} + \widetilde{\boldsymbol{E}}_e \left(-n\widetilde{\boldsymbol{C}}_{\boldsymbol{\phi}_c}\right)^{(-n-1)} \frac{\partial \widetilde{\psi}}{\partial\left(\widetilde{\boldsymbol{E}}_e \widetilde{\boldsymbol{C}}_{\boldsymbol{\phi}_c}^{-\boldsymbol{n}}\right)} : \widetilde{\boldsymbol{E}}_e \dot{\widetilde{\boldsymbol{C}}}_{\boldsymbol{\phi}_c}^{-\boldsymbol{n}} + \frac{\partial \widetilde{\psi}}{\partial \widetilde{\varepsilon}_s \widetilde{t}_d} : \dot{\widetilde{\varepsilon}}_s \widetilde{t}_d \\
& + \frac{\partial \widetilde{\psi}}{\partial \widetilde{\varepsilon}_s \widetilde{t}_d} : \widetilde{\varepsilon}_s \dot{\widetilde{t}}_d + \frac{\partial \widetilde{\psi}}{\partial \widetilde{\boldsymbol{\beta}} \widetilde{\boldsymbol{C}}_{\boldsymbol{\phi}_m}^{-\boldsymbol{n}}} : \dot{\widetilde{\boldsymbol{\beta}}} \widetilde{\boldsymbol{C}}_{\boldsymbol{\phi}_m}^{-\boldsymbol{n}} + \widetilde{\boldsymbol{\beta}} \left(-n\widetilde{\boldsymbol{C}}_{\boldsymbol{\phi}_m}\right)^{(-n-1)} \frac{\partial \widetilde{\psi}}{\partial \widetilde{\boldsymbol{\beta}} \widetilde{\boldsymbol{C}}_{\boldsymbol{\phi}_m}^{-\boldsymbol{n}}} : \widetilde{\boldsymbol{\beta}} \dot{\widetilde{\boldsymbol{C}}}_{\boldsymbol{\phi}_m}^{-\boldsymbol{n}} \\
& + \frac{\partial \widetilde{\psi}}{\partial \widetilde{\boldsymbol{\beta}} \widetilde{\boldsymbol{C}}_{\boldsymbol{\phi}_c}^{-\boldsymbol{n}}} : \dot{\widetilde{\boldsymbol{\beta}}} \widetilde{\boldsymbol{C}}_{\boldsymbol{\phi}_c}^{-\boldsymbol{n}} + \widetilde{\boldsymbol{\beta}} \left(-n\widetilde{\boldsymbol{C}}_{\boldsymbol{\phi}_c}\right)^{(-n-1)} \frac{\partial \widetilde{\psi}}{\partial \widetilde{\boldsymbol{\beta}} \widetilde{\boldsymbol{C}}_{\boldsymbol{\phi}_c}^{-\boldsymbol{n}}} : \widetilde{\boldsymbol{\beta}} \dot{\widetilde{\boldsymbol{C}}}_{\boldsymbol{\phi}_c}^{-\boldsymbol{n}}
\end{aligned} \qquad \text{(Eq. 3.44)}$$

By substituting Eq. (3.44) into Eq. (3.40), we get

$$
\begin{aligned}
&\left[\widetilde{\boldsymbol{S}}-\widetilde{\rho}\frac{\partial\widetilde{\psi}}{\partial\left(\widetilde{\boldsymbol{E}}_e\widetilde{\boldsymbol{C}}_{\boldsymbol{\phi}_m}^{-n}\right)}\left(\widetilde{\boldsymbol{C}}_{\boldsymbol{\phi}_m}^{-n}\right)^T-\widetilde{\rho}\frac{\partial\widetilde{\psi}}{\partial\left(\widetilde{\boldsymbol{E}}_e\widetilde{\boldsymbol{C}}_{\boldsymbol{\phi}_c}^{-n}\right)}\left(\widetilde{\boldsymbol{C}}_{\boldsymbol{\phi}_c}^{-n}\right)^T\right]:\dot{\widetilde{\boldsymbol{E}}}_e\\
&+\widetilde{\boldsymbol{S}}:\left[\widetilde{\boldsymbol{d}}_{\boldsymbol{\phi}}+\widetilde{\boldsymbol{d}}_p+\left(\widetilde{\boldsymbol{l}}^T-\widetilde{\boldsymbol{l}}_e^T\right)\widetilde{\boldsymbol{E}}_e+\widetilde{\boldsymbol{E}}_e\left(\widetilde{\boldsymbol{l}}-\widetilde{\boldsymbol{l}}_e\right)\right]\\
&-\widetilde{\rho}\left[\widetilde{\boldsymbol{E}}_e\left(-n\widetilde{\boldsymbol{C}}_{\boldsymbol{\phi}_m}\right)^{(-n-1)}\frac{\partial\widetilde{\psi}}{\partial\left(\widetilde{\boldsymbol{E}}_e\widetilde{\boldsymbol{C}}_{\boldsymbol{\phi}_m}^{-n}\right)}:\widetilde{\boldsymbol{E}}_e\dot{\widetilde{\boldsymbol{C}}}_{\boldsymbol{\phi}_m}^{-n}\right]\\
&-\widetilde{\rho}\left[\widetilde{\boldsymbol{E}}_e\left(-n\widetilde{\boldsymbol{C}}_{\boldsymbol{\phi}_c}\right)^{(-n-1)}\frac{\partial\widetilde{\psi}}{\partial\left(\widetilde{\boldsymbol{E}}_e\widetilde{\boldsymbol{C}}_{\boldsymbol{\phi}_c}^{-n}\right)}:\widetilde{\boldsymbol{E}}_e\dot{\widetilde{\boldsymbol{C}}}_{\boldsymbol{\phi}_c}^{-n}\right]-\widetilde{\rho}\frac{\partial\widetilde{\psi}}{\partial\widetilde{\varepsilon}_s\widetilde{t}_d}:\dot{\widetilde{\varepsilon}}_s\widetilde{t}_d\\
&-\widetilde{\rho}\frac{\partial\widetilde{\psi}}{\partial\widetilde{\varepsilon}_s\widetilde{t}_d}:\widetilde{\varepsilon}_s\dot{\widetilde{t}}_d-\widetilde{\rho}\frac{\partial\widetilde{\psi}}{\partial\widetilde{\boldsymbol{\beta}}\widetilde{\boldsymbol{C}}_{\boldsymbol{\phi}_m}}:\dot{\widetilde{\boldsymbol{\beta}}}\widetilde{\boldsymbol{C}}_{\boldsymbol{\phi}_m}-\widetilde{\rho}\left[\widetilde{\boldsymbol{\beta}}\left(-n\widetilde{\boldsymbol{C}}_{\boldsymbol{\phi}_m}\right)^{(-n-1)}\frac{\partial\widetilde{\psi}}{\partial\widetilde{\boldsymbol{\beta}}\widetilde{\boldsymbol{C}}_{\boldsymbol{\phi}_m}^{-n}}:\widetilde{\boldsymbol{\beta}}\dot{\widetilde{\boldsymbol{C}}}_{\boldsymbol{\phi}_m}^{-n}\right]\\
&-\widetilde{\rho}\frac{\partial\widetilde{\psi}}{\partial\widetilde{\boldsymbol{\beta}}\widetilde{\boldsymbol{C}}_{\boldsymbol{\phi}_c}}:\dot{\widetilde{\boldsymbol{\beta}}}\widetilde{\boldsymbol{C}}_{\boldsymbol{\phi}_c}-\widetilde{\rho}\left[\widetilde{\boldsymbol{\beta}}\left(-n\widetilde{\boldsymbol{C}}_{\boldsymbol{\phi}_c}\right)^{(-n-1)}\frac{\partial\widetilde{\psi}}{\partial\widetilde{\boldsymbol{\beta}}\widetilde{\boldsymbol{C}}_{\boldsymbol{\phi}_c}^{-n}}:\widetilde{\boldsymbol{\beta}}\dot{\widetilde{\boldsymbol{C}}}_{\boldsymbol{\phi}_c}^{-n}\right]\geq 0
\end{aligned}
\qquad \text{(Eq. 3.45)}
$$

The constitutive law for $\widetilde{\boldsymbol{S}}$ is obtained as

$$
\widetilde{\boldsymbol{S}}=\widetilde{\rho}\frac{\partial\widetilde{\psi}}{\partial\left(\widetilde{\boldsymbol{E}}_e\widetilde{\boldsymbol{C}}_{\boldsymbol{\phi}_m}^{-n}\right)}\left(\widetilde{\boldsymbol{C}}_{\boldsymbol{\phi}_m}^{-n}\right)^T+\widetilde{\rho}\frac{\partial\widetilde{\psi}}{\partial\left(\widetilde{\boldsymbol{E}}_e\widetilde{\boldsymbol{C}}_{\boldsymbol{\phi}_c}^{-n}\right)}\left(\widetilde{\boldsymbol{C}}_{\boldsymbol{\phi}_c}^{-n}\right)^T \qquad \text{(Eq. 3.46)}
$$

Thus, the dissipation can be simplified as:

$$
\begin{aligned}
&\widetilde{\boldsymbol{S}}:\begin{bmatrix}\widetilde{\boldsymbol{d}}_{\boldsymbol{\phi}}+\widetilde{\boldsymbol{d}}_p+\left(\widetilde{\boldsymbol{l}}^T-\widetilde{\boldsymbol{l}}_e^T\right)\widetilde{\boldsymbol{E}}_e\\+\widetilde{\boldsymbol{E}}_e\left(\widetilde{\boldsymbol{l}}-\widetilde{\boldsymbol{l}}_e\right)\end{bmatrix}-\widetilde{\rho}\left[\widetilde{\boldsymbol{E}}_e\left(-n\widetilde{\boldsymbol{C}}_{\boldsymbol{\phi}_m}\right)^{(-n-1)}\frac{\partial\widetilde{\psi}}{\partial\left(\widetilde{\boldsymbol{E}}_e\widetilde{\boldsymbol{C}}_{\boldsymbol{\phi}_m}^{-n}\right)}:\widetilde{\boldsymbol{E}}_e\dot{\widetilde{\boldsymbol{C}}}_{\boldsymbol{\phi}_m}^{-n}\right]\\
&-\widetilde{\rho}\left[\widetilde{\boldsymbol{E}}_e\left(-n\widetilde{\boldsymbol{C}}_{\boldsymbol{\phi}_c}\right)^{(-n-1)}\frac{\partial\widetilde{\psi}}{\partial\left(\widetilde{\boldsymbol{E}}_e\widetilde{\boldsymbol{C}}_{\boldsymbol{\phi}_c}^{-n}\right)}:\widetilde{\boldsymbol{E}}_e\dot{\widetilde{\boldsymbol{C}}}_{\boldsymbol{\phi}_c}^{-n}\right]-\widetilde{\rho}\frac{\partial\widetilde{\psi}}{\partial\widetilde{\varepsilon}_s\widetilde{t}_d}:\dot{\widetilde{\varepsilon}}_s\widetilde{t}_d\\
&-\widetilde{\rho}\frac{\partial\widetilde{\psi}}{\partial\widetilde{\varepsilon}_s\widetilde{t}_d}:\widetilde{\varepsilon}_s\dot{\widetilde{t}}_d-\widetilde{\rho}\frac{\partial\widetilde{\psi}}{\partial\widetilde{\boldsymbol{\beta}}\widetilde{\boldsymbol{C}}_{\boldsymbol{\phi}_m}}:\dot{\widetilde{\boldsymbol{\beta}}}\widetilde{\boldsymbol{C}}_{\boldsymbol{\phi}_m}-\widetilde{\rho}\left[\widetilde{\boldsymbol{\beta}}\left(-n\widetilde{\boldsymbol{C}}_{\boldsymbol{\phi}_m}\right)^{(-n-1)}\frac{\partial\widetilde{\psi}}{\partial\widetilde{\boldsymbol{\beta}}\widetilde{\boldsymbol{C}}_{\boldsymbol{\phi}_m}^{-n}}:\widetilde{\boldsymbol{\beta}}\dot{\widetilde{\boldsymbol{C}}}_{\boldsymbol{\phi}_m}^{-n}\right]\\
&-\widetilde{\rho}\frac{\partial\widetilde{\psi}}{\partial\widetilde{\boldsymbol{\beta}}\widetilde{\boldsymbol{C}}_{\boldsymbol{\phi}_c}}:\dot{\widetilde{\boldsymbol{\beta}}}\widetilde{\boldsymbol{C}}_{\boldsymbol{\phi}_c}-\widetilde{\rho}\left[\widetilde{\boldsymbol{\beta}}\left(-n\widetilde{\boldsymbol{C}}_{\boldsymbol{\phi}_c}\right)^{(-n-1)}\frac{\partial\widetilde{\psi}}{\partial\widetilde{\boldsymbol{\beta}}\widetilde{\boldsymbol{C}}_{\boldsymbol{\phi}_c}^{-n}}:\widetilde{\boldsymbol{\beta}}\dot{\widetilde{\boldsymbol{C}}}_{\boldsymbol{\phi}_c}^{-n}\right]\geq 0
\end{aligned}
\qquad \text{(Eq. 3.47)}
$$

The first term is the external work from deviatoric plastic deformation; the second term represents external work from damage-induced volumetric expansion, and the third term is the dissipation from internal work from the dislocations. The third term is related to ISVs.

3.4 Kinetics

3.4.1 Moduli Degradation

The development of the continuum damage mechanics began with the introduction of a scalar damage variable [73] that represents the degradation of strength in a one-dimensional tensile bar due to creep. Bammann et al. [32] extended the idea to the so-called Unified Creep-Plasticity (UCP) framework. Similar to Bammann and Solanki [74], we can consider a uniform bar subjected to a uniaxial tensile stress, σ, as shown in Figure 3.2.

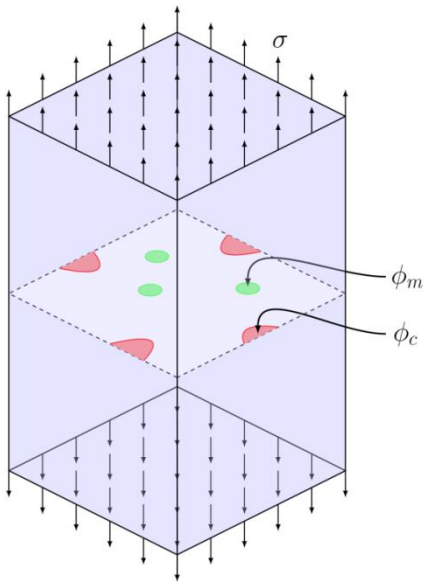

Figure 3.2 A square bar subjected to uniaxial tension with damage effects from mechanical and chemical interactions.

The uniaxial case can easily be expressed using the formula

$$\sigma = \frac{P}{A} \qquad \text{(Eq. 3.48)}$$

where P is the applied load and A is the cross sectional area. In order to use the principles of continuum damage mechanics, the following expression for the effective uniaxial stress [73,83] is derived such that:

$$\sigma_D = \frac{P}{A(1-\phi)} \qquad \text{(Eq. 3.49)}$$

where damage is defined as the loss of cross-sectional area or a decrease of load carrying capacity. For our case, the total damage is based off an additive decomposition of mechanical, ϕ_m, and corrosion, ϕ_c, interactions and is defined as the following:

$$\phi = \phi_m + \phi_c \qquad \text{(Eq. 3.50)}$$

The effective stress tensor, $\boldsymbol{\sigma}_D$, and the nominal stress tensor, $\boldsymbol{\sigma}$, for the isotropic damage case can then be rewritten as follows:

$$\boldsymbol{\sigma}_D = \frac{\boldsymbol{\sigma}}{(1-\phi_m-\phi_c)} \qquad \text{(Eq. 3.51)}$$

For Hookean elasticity, we get

$$\boldsymbol{\sigma}_D = E(1-\phi_m-\phi_c)\boldsymbol{\varepsilon}_e \qquad \text{(Eq. 3.52)}$$

where damage tends to degrade the elastic moduli. A detailed three dimensional approximation was derived by Budiansky and O'Connell [84] using self-consistent techniques. They found the elastic moduli were degraded according to

$$\boldsymbol{\sigma}_D = \left(K(\phi) - \frac{2}{3}\mu(\phi) \right) \boldsymbol{I} + 2\mu(\phi)\boldsymbol{\varepsilon}_e \qquad \text{(Eq. 3.53)}$$

where the bulk modulus coefficient $K(\phi) = K_0 \left[1 - \frac{3(1-v_0)}{2(1-2v_0)}\phi \right]$ and the shear modulus coefficient $\mu(\phi) = \mu_0 \left[1 - \frac{15(1-v_0)}{7-5v_0}\phi \right]$ as discussed in Bammann and Solanki [74].

3.4.2 Damage Evolution

The damage due to the mechanical loading effects follows the Horstemeyer et al. [35,85] model where

$$\phi_m = \eta v c \qquad \text{(Eq. 3.54)}$$

In an effort to create a consistent, physically-based model describing the corrosion of a material, we have employed conservation laws and empirical relationships for the following proposed model. The total corrosion damage is as follows:

$$\phi_c = \phi_{gc} + \phi_{pc} + \phi_{ic} \qquad \text{(Eq. 3.55)}$$

where ϕ_{gc} is the damage from general corrosion, ϕ_{pc} is the damage from pitting corrosion, and ϕ_{ic} is the damage from intergranular corrosion. To calculate the corrosion due to pitting, a similar model to Horstemeyer et al. [35] mechanically induced defects was developed and can be expressed as the following:

$$\phi_{pc} = \eta_p v_p c_p \qquad \text{(Eq. 3.56)}$$

where η_p is the pit number density related to nucleation of pits (number per unit area), v_p is the area of pit growth related to growth of the pits, and c_p is a function of the NND

related to the coalescence of the pits. The generalized rate form for the total damage then can be written as the following:

$$\dot{\phi}_c = \dot{\phi}_{gc} + \dot{\phi}_{pc} + \dot{\phi}_{ic} \qquad \text{(Eq. 3.57)}$$

The assumption here is that the corrosion damage rate at any given time due to these mechanisms is only a surface effect.

3.4.2.1 General Corrosion Rate

General corrosion will be referred to corrosion dominated by uniform thinning that proceeds without appreciable localized attack [86]. For the general corrosion rate, $\dot{\phi}_{gc}$, a modified Faraday's Law of Electrolysis to summarize mass loss based on the total electric charge of the substance is presented. Faraday's Law [87] is expressed as the following:

$$m = \frac{QM}{Fz} \qquad \text{(Eq. 3.58)}$$

where m is the mass of the substance liberated at an electrode in grams, Q is the total electric charge that passed through the substance, F is the Faraday constant = $96{,}485\,\text{C/mol}$, M is the molar mass of the substance, and z is the valence number of ions of the substance. For mass loss, a linear relationship with respect to time was assumed, $m = C_1 t$. Rearranging Eq. (3.58), we arrive at the following relationship for general corrosion

$$\dot{\phi}_{gc} = \dot{Q}(t) = \frac{C_1 Fzt}{M} \qquad \text{(Eq. 3.59)}$$

where C_1 is a material constant. The relationship ensures that in combination with the chemical balance equations that conservation of mass is realized.

3.4.2.2 Pitting Corrosion Rate

In the Mg literature, "localized corrosion" is commonly used as pitting [15]. Since we are using a Mg alloy for our application, we relate localized corrosion to pitting. Also, pitting corrosion can occur in either a passive or a nonpassive manner [86]. The generalized pitting corrosion rate can be expressed as the following:

$$\dot{\phi}_{pc} = \dot{\eta}_p v_p c_p + \eta_p \dot{v}_p c_p + \eta_p v_p \dot{c}_p \qquad \text{(Eq. 3.60)}$$

The damage evolution of the pit nucleation mechanism follows a piecewise power and exponential trend. The relationship can be expressed as the following,

$$\dot{\eta}_p(t) = \begin{cases} C_2 t^{C_3} & \text{if } t < t_y \\ \eta_{sat} + C_4 t^{C_5} & \text{if } t \geq t_y \end{cases} \qquad \text{(Eq. 3.61)}$$

where t_y is the transition time between nucleation and coalescence dominated damage; η_{sat} is the saturation level of the number density; and C_2, C_3, C_4, and C_5 are material constants. The transition occurs when pits begin to coalescence at a faster rate than they nucleate across the surface. This causes the relationship to initially increase when pit nucleation is dominant, and then decrease towards the saturation level when coalescence is dominant.

The pit growth rate, $\dot{v}_p$, can be described by the following power law equation,

$$\dot{v}_p(t) = C_6 t^{C_7} \qquad \text{(Eq. 3.62)}$$

where C_6 and C_7 are material constants. This signifies the area fraction at which pits are growing across the surface. Physical measurements of the nucleation density are a number count per unit area, so the void growth area must be used. One could employ a void volume measurement instead of the void area measurement, but then the number density in Eq. (3.61) would need to be per unit volume and not per unit area. Either choice can work; they just have to be consistent.

The coalescence rate, $\dot{c}$, is assumed to relate to Coulomb's Law [88] and Maxwell's stress. Both represent an electrostatic interaction between two charged particles with respect to the force on the body. In our study, we focus on the electrochemical interaction between two pits (with some electric charge) on the surface, so we assume an averaged charged value in the region as a continuum point; hence, for coalescence we assume two continuum points. The scalar form of Coulomb's Law is the following,

$$F = \frac{k_e q_1 q_2}{r^2} \qquad \text{(Eq. 3.63)}$$

where r is the separation distance, k_e is the proportionality constant = 8.987×10^9 $\mathrm{Nm^2/C^2}$, q_1 and q_2 are point charges, and F is the force interaction between the points. For a foundation to this model, the point charges will be equivalent to the elementary charge ($e = 1.602 \times 10^{-19}$ C) of an electron [89,90]. The separation distance, r, will be defined as the NND. As the NND approaches zero, the force of interaction reaches its maximum potential. In combination with Maxwell's stress, if we take the relationship and rearrange to get a rate form of the coalescence, we arrive at the following rate equation,

$$\dot{c}_p(t) = \frac{k_e q_1 q_2}{\pi \varepsilon_0 \left(N\dot{N}D(t)\right)^4} \qquad \text{(Eq. 3.64)}$$

where ε_0 is the electric constant = 8.854×10^{-12} F/m and $N\dot{N}D(t) = \begin{cases} C_8 t^{C_9} & \text{if } t < t_y \\ C_{10} t^{C_{11}} & \text{if } t \geq t_y \end{cases}$

with material constants of C_8, C_9, C_{10}, and C_{11}.

3.4.2.3 Intergranular Corrosion Rate

The definition of intergranular corrosion is localized corrosion that occurs at the grain boundaries caused by precipitates and segregation leading to the formation of microgalvanic cells [86]. For the intergranular corrosion rate, $\dot{\phi}_{ic}$, we postulate the following equation,

$$\dot{\phi}_{ic} = IC\dot{A}F(t)\left(\frac{MO}{MO_0}\right)^{z_{ic}} \qquad \text{(Eq. 3.65)}$$

where $IC\dot{A}F(t) = \begin{cases} C_{12} t^{C_{13}} & \text{if } t < t_c \\ C_{14} t^{C_{15}} & \text{if } t \geq t_c \end{cases}$ and t_c is the transition time at which intergranular corrosion reaches its maximum rate. C_{12}, C_{13}, C_{14}, and C_{15} are material constants. $(MO/MO_0)^{z_{ic}}$ is a misorientation factor that represents galvanic cells formed. A fundamental aspect of corrosion of Mg alloys is the role of second phase particles. The particles cause the galvanic cells [15] that induce a faster corrosion rate at the grain boundary than within the matrix material, and Eq. (3.65) accounts for that phenomenon.

3.5 Corrosion Cases

The following section describes different corrosion scenarios in which each mechanism presented above is the dominant mechanism. Figure 3.3 illustrates five cases in comparison with a baseline reference (dotted line) to help visualize the differences.

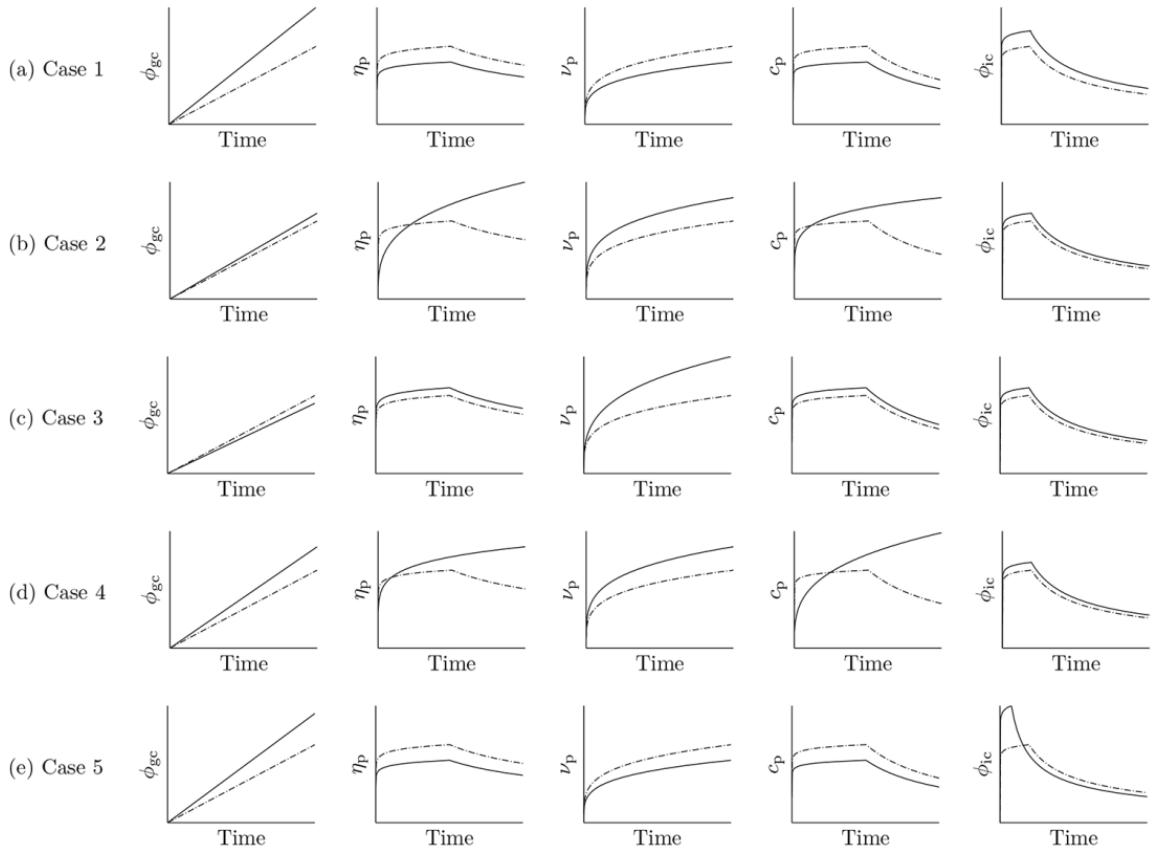

Figure 3.3 Theoretical corrosion scenarios.

The scenarios depict cases in which the respective (a) general corrosion, (b) pit nucleation, (c) pit growth, (d) pit coalescence, and (e) intergranular corrosion mechanism dominates. The dotted line shows a baseline reference to help visualize and compare the different cases. The solid black line represents the predicted response.

3.5.1 Case 1: General Corrosion is Dominant

When general corrosion is dominant (Figure 3.3a), the rate of general corrosion, $\dot{\phi}_{gc}$, will be greater than the other rates ($\dot{\phi}_{pc}$ and $\dot{\phi}_{ic}$). In this case, the thickness reduces faster than pit nucleation, pit growth, pit coalescence, and intergranular corrosion rates. Since general corrosion removes material that otherwise would account for the pit nucleation, growth, and coalescence, one might not experimentally see many pits. This does not mean that pitting corrosion would not occur, but only that the general corrosion occurs so much faster that pitting is minimized.

3.5.2 Case 2: Pit Nucleation is Dominant

When pit nucleation is dominant (Figure 3.3b), the pit nucleation rate, $\dot{\eta}_p$, is greater so more pits will be prevalent as opposed to more pits growing. Also, the thickness reduction will be lesser allowing more pits to form, and the pits will nucleate around particles faster than between the grain boundaries. Again, this does not mean that pit growth, pit coalescence, general corrosion, or intergranular corrosion are not occurring, but just that they are occurring at a lesser rate than the pit nucleation rate.

3.5.3 Case 3: Pit Growth is Dominant

When pit growth is dominant (Figure 3.3c), the in-plane or depth pit growth rate, $\dot{v}_p$, is more prevalent than general corrosion, pit nucleation, and pit coalescence. Pit growth can occur by growing deep into the material, by spreading across the surface, or both. If this were to occur, then one would expect to observe the greatest pit growth over time compared to the other cases. Because the general corrosion rate would be lesser than the pit growth rate, not much thickness loss would occur comparatively. When

comparing Case 2 to Case 3, one would expect that the alloying elements are less diffusely distributed for Case 3 to allow greater pit growth. Alternatively, the alloying elements would be more involved in the intermetallics or second phase particles for Case 2 to be more prevalent (pit nucleation being more dominant than pit growth).

3.5.4 Case 4: Pit Coalescence is Dominant

When pit coalescence is dominant (Figure 3.3d), the pit coalescence rate, $\dot{c}_p$, between pits is more prevalent than general corrosion, pit nucleation, and pit growth. Pit coalescence occurs as pits join together (decrease in NND) and is characterized many times by transgranular corrosion. If this were to occur, then one would expect to see the highest values over time compared to the other cases.

3.5.5 Case 5: Intergranular Corrosion is Dominant

When intergranular corrosion is dominant (Figure 3.3e), the rate of intergranular corrosion, $\dot{\phi}_{ic}$, is greater than the other rates ($\dot{\phi}_{pc}$ and $\dot{\phi}_{gc}$). As such, the corrosion along grain boundaries occurs at a faster rate than pit nucleation, pit growth, pit coalescence, and general corrosion. With a rapid deterioration of the grain boundaries, one might also expect to see an influence on general corrosion as well.

3.6 Conclusions

In this chapter, we present a corrosion constitutive model that is internally consistent with the thermodynamics, kinematics, and kinetics based upon the original works of Coleman Gurtin [38], Bammann [22,32–34], and Horstemeyer [35] who created a model in a thermomechanical damage framework. This will enable the prediction of

coupled mechanical and corrosion history effects often called SCC. The model distinguishes between the functional and rate forms of each mechanism and is physically motivated by empirically observed and quantified relationships. This theoretical framework presented here is easily extendable to the addition of other damage mechanisms (not shown here), and can be generalized to the development of consistent coupled equations. A tensor ISV is introduced into the model that will affect the evolution of geometrically necessary dislocations and statistically stored dislocations due to the chemomechanical fundamental mechanism.

CHAPTER IV

APPLICATION OF THE CORROSION DAMAGE MODEL TO MAGNESIUM ALLOYS

4.1 Introduction

In this study, the application of a novel approach in modeling the macroscopic corrosion damage evolution is considered. Experimentally quantified data on mass loss, pit nucleation, pit growth, pit NND, and intergranular corrosion effects similar to prior work (e.g. [7,49–51,91,92]) must be available to validate the model. The ability of the model to predict aspects of the corrosion process (general, pitting, and intergranular corrosion) are illustrated by comparison with experimental data of extruded (AZ31, AZ61, AM30) and as-cast (AM60 and AE44) Mg alloys. The application of the corrosion damage model presented in Chapter 3 to a broad range of alloys confirms a generalized form has been presented.

4.2 Boundary Conditions

Since the model distinguishes between the functional and rate forms of each mechanism and is physically motivated by empirically observed and quantified relationships, each will required boundary condition calculations to normalize the damage state with respect to time. For example in the general corrosion mechanism, the maximum mass loss ($\dot{m} = C_1 t$) would be equivalent to the mass of the specimen in which

the quantification data was garnered. Using the rate form, the time at which the upper boundary condition would be met can be solved. The time then could be inputted into the functional and rate forms of the damage mechanisms ($\phi_{gc}, \eta_p, v_p, c_p,$ and ϕ_{ic}) to obtain the upper bound, respectively.

4.3 Results and Discussion

As part of the studies on the damage evolution of general, pitting, and intergranular corrosion, the weight loss, pit number density per unit area, pit area fraction, pit nearest neighbor distance, and intergranular corrosion area fraction measurements were made for the AZ31, AZ61, AM30, AM60, and AE44 magnesium alloys. The alloys were exposed to salt spray and immersion environments in a 3.5 wt% NaCl solution. They are also differentiated by the two forms in which they were created: extruded (AZ31, AZ61, AM30) and as-cast (AM60 and AE44). The measurements are all shown as a function of exposure time in comparison with the predictions of the corrosion damage model in Figures 4.1-4.6.

4.3.1 Application to AZ Series Alloys

Figure 4.1 and 4.2 show a comparison of the model to (a) change in mass, (b) pit number density, (c) pit area fraction, (d) pit nearest neighbor distance, (e) intergranular corrosion area fraction, and (f) the total corrosion damage for extruded AZ31 and AZ61 magnesium alloys exposed to salt spray and immersion environments, respectively. When looking at the individual damage mechanisms from the figures (a)-(e), the model shows to be in good agreement with the experimental data. Notice on both the pit number density and pit nearest neighbor distance graphs for both environments that the

transition time between nucleation and coalescence dominated damage was attained. The AZ31 and AZ61 reached the transition time in the salt spray environment at approximately 4 hours of exposure. In the immersion environment, the transition time was approximately 4 and 12 hours of exposure for the AZ31 and AZ61 alloys, respectively. When examining the total corrosion damage for the specimens, we can confirm the notion that as aluminum percentage increases in the alloying system that it improves corrosion resistance. For the salt spray environment, the corrosion rate for the AZ31 was initially higher compared to the AZ61 alloy. This can be described by the high pit nucleation rate between 0 hours and 4 hours of exposure. Once coalescence began to dominate on the AZ61 surface, the nucleation rate decreased significantly throughout the entire 60 hours of exposure. Although, there is only a slight difference in the AZ31 and AZ61 rates for the salt spray environment, the immersion environment (Figure 4.2) shows a large difference between responses for the two alloys. For the AZ31, the mechanism transition times, t_y and t_c, both occurred at 4 hours of exposure. For AZ61, t_y occurred at approximately 12 hours of exposure but t_c did not occur within the 60 hour testing matrix. This indicates that the pit formation and intergranular corrosion damage was occurring on the AZ31 faster than the AZ61. Hence, the resulting corrosion damage illustrated in Figure 4.2f shows a significant difference between the two alloys.

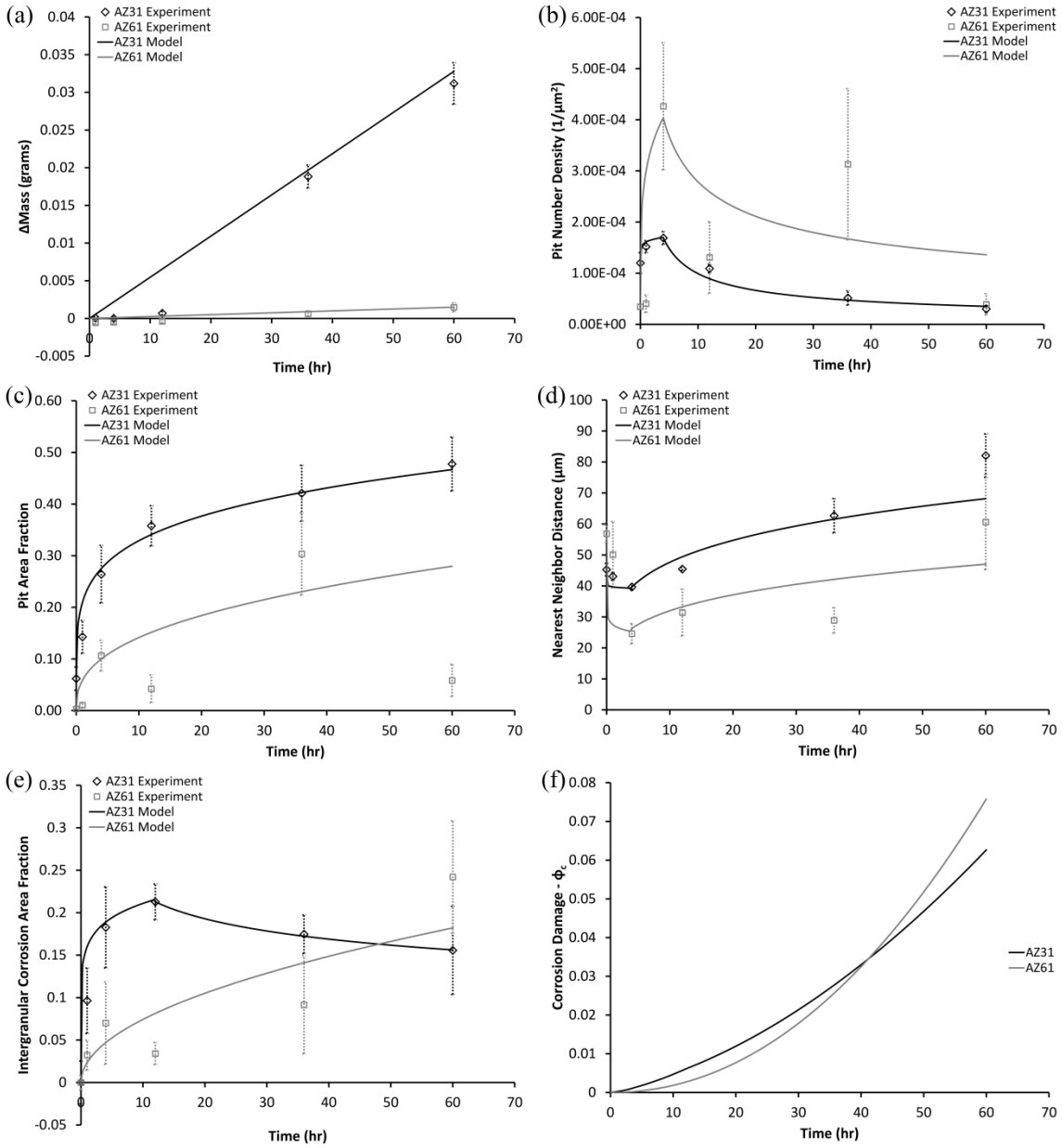

Figure 4.1 Model application for extruded AZ31 and AZ61 exposed to a 3.5 wt% NaCl salt spray environment.

The figure shows experimental data versus the model for (a) change in mass, (b) pit number density, (c) pit area fraction, (d) pit nearest neighbor distance, (e) intergranular corrosion area fraction, and (f) the total corrosion damage. The error bars were one standard deviation in each direction.

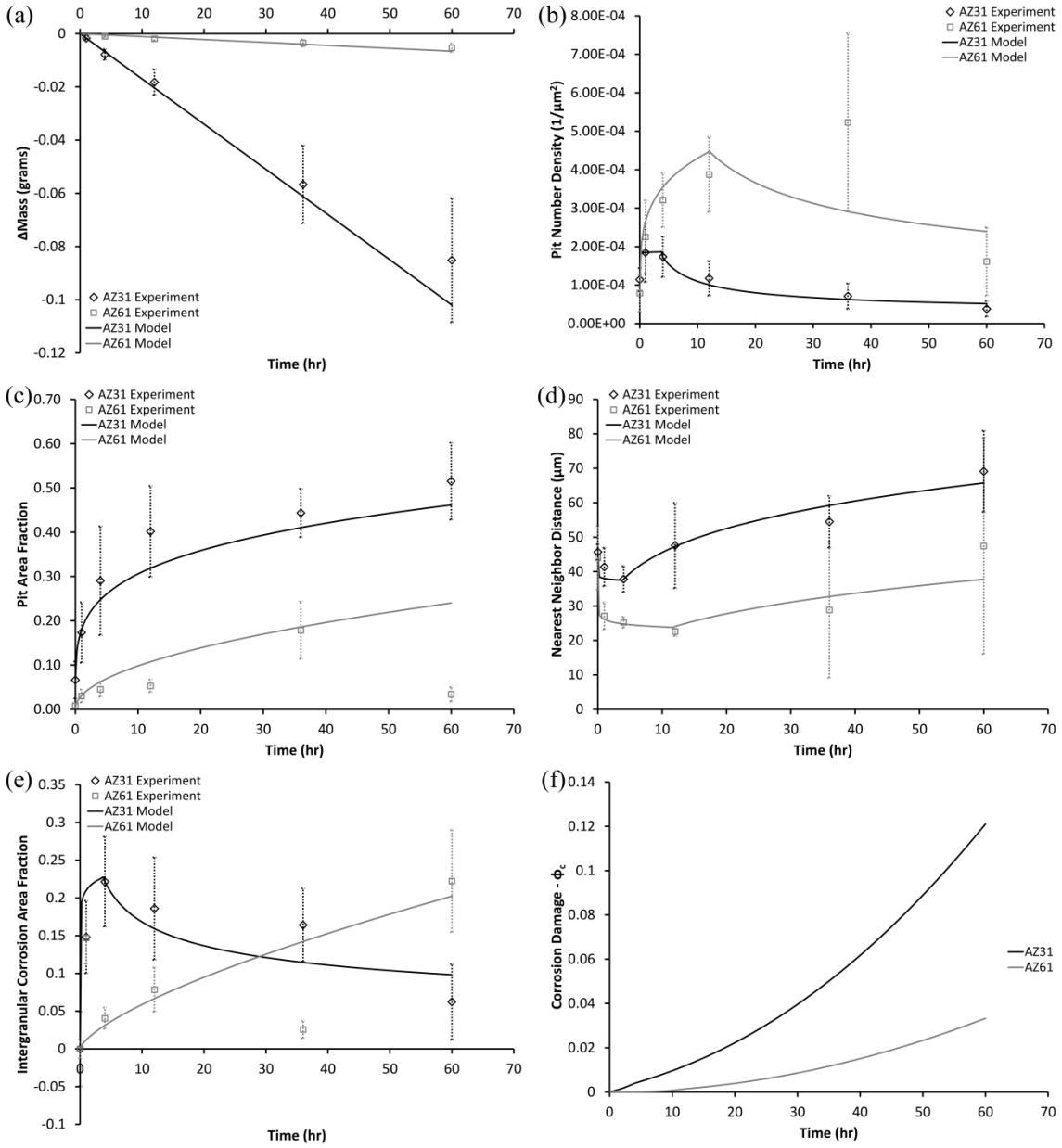

Figure 4.2 Model application for extruded AZ31 and AZ61 exposed to a 3.5 wt% NaCl immersion environment.

The figure shows experimental data versus the model for (a) change in mass, (b) pit number density, (c) pit area fraction, (d) pit nearest neighbor distance, (e) intergranular corrosion area fraction, and (f) the total corrosion damage. The error bars were one standard deviation in each direction.

4.3.2 Application to AM Series Alloys

Figure 4.3 and 4.4 show a comparison of the model to (a) change in mass, (b) pit number density, (c) pit area fraction, (d) pit nearest neighbor distance, (e) intergranular corrosion area fraction, and (f) the total corrosion damage for extruded AM30 and as-cast AM60 magnesium alloys exposed to salt spray and immersion environments, respectively. When looking at the individual damage mechanisms from the figures (a)-(e), the model shows to be in good agreement with the experimental data. One major difference seen between the AM30 and AM60 data sets is the transition time, t_y (Figure 4.3b and 4.3d). For the AM30 alloy in the salt spray environment, there is no observed transition time, but rather an immediate decrease in the pit number density and immediate increase in nearest neighbor distance. There are two options that can describe such an observed response. First, the transition could have been between 0 and 1 hour of exposure. In this case, the time was missed based on the chosen experimental observation times. Second, this could indicate that pit growth was the dominated damage mechanism for the alloy. Conversely, the AM30 in the immersion environment shows the transition time to be approximately at 12 hours of exposure. Examining the AM60 alloy in the salt spray environment, t_y was not observed. Also, pit growth did not exceed 5% of the surface area in both the salt spray and immersion environments which is very low compared to any alloy presented in this article. The overall corrosion rates are significantly different based on the environment in which the alloys were exposed. In the salt spray case (Figure 4.3f), the AM30 showed a significant higher corrosion rate than the AM60 alloy. Conversely for the immersion case (Figure 4.4f), the AM60 experienced a fast corrosion rate. Initial conclusions for the differences between the data

could be explained by the difference in Al content, but since microstructure studies during the corrosion testing were not complete, we cannot confirm that conclusion.

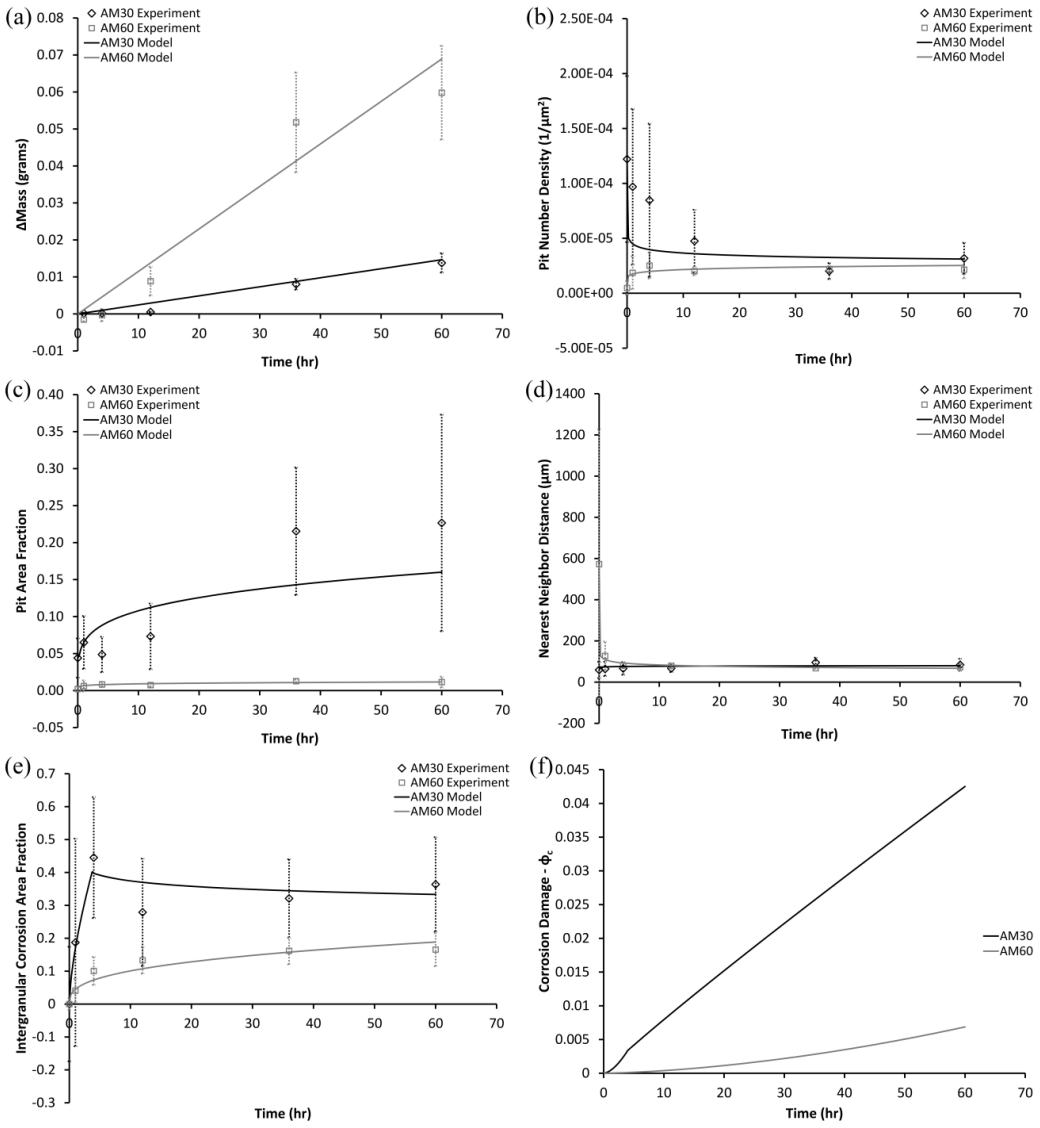

Figure 4.3 Model application for extruded AM30 and cast AM60 exposed to a 3.5 wt% NaCl salt spray environment.

The figure shows experimental data versus the model for (a) change in mass, (b) pit number density, (c) pit area fraction, (d) pit nearest neighbor distance, (e) intergranular corrosion area fraction, and (f) the total corrosion damage. The error bars were one standard deviation in each direction.

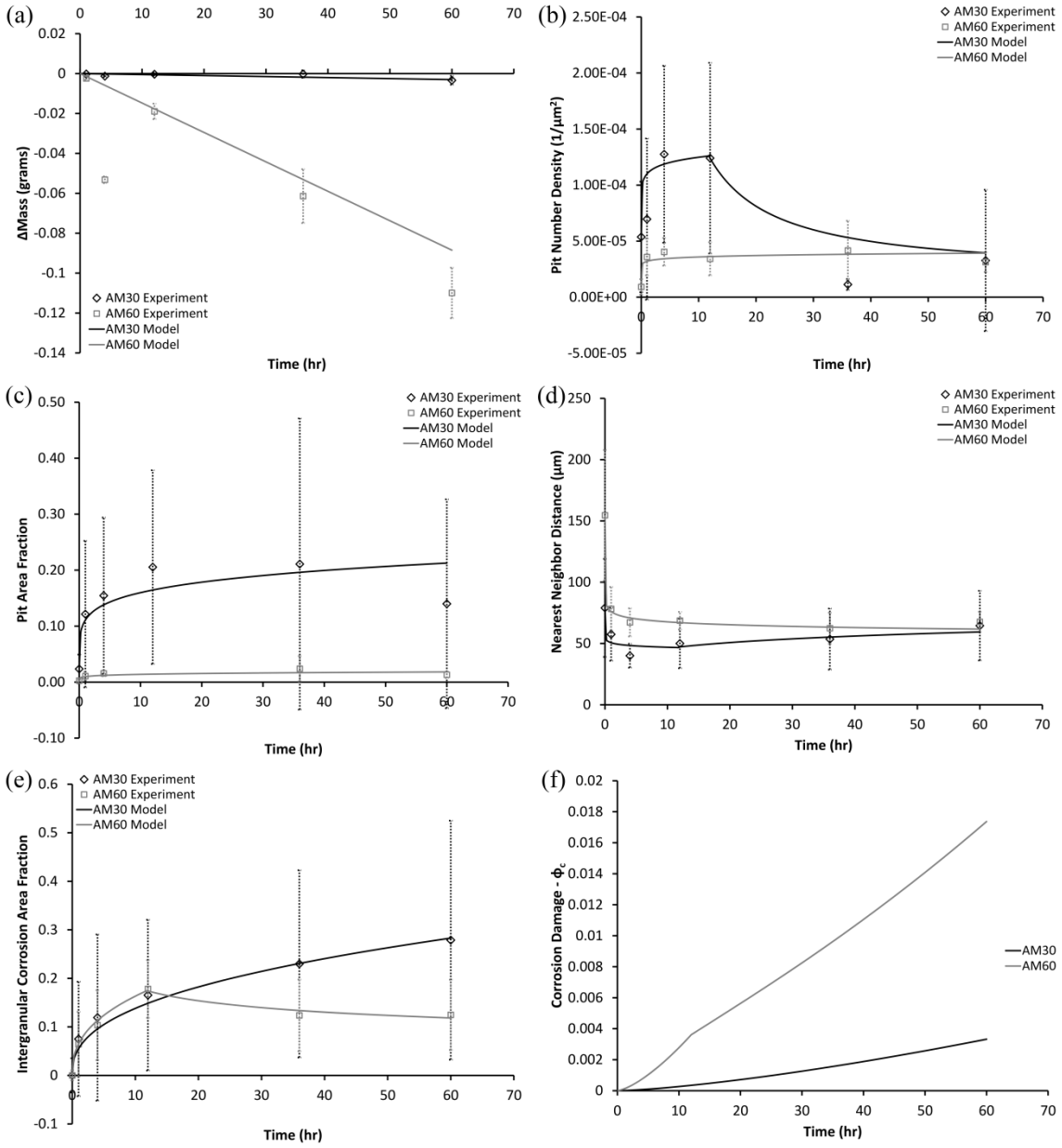

Figure 4.4 Model application for extruded AM30 and cast AM60 exposed to a 3.5 wt% NaCl immersion environment.

The figure shows experimental data versus the model for (a) change in mass, (b) pit number density, (c) pit area fraction, (d) pit nearest neighbor distance, (e) intergranular corrosion area fraction, and (f) the total corrosion damage. The error bars were one standard deviation in each direction.

4.3.3 Application to an AE Series Alloy

Figure 4.5 and 4.6 show a comparison of the model to (a) change in mass, (b) pit number density, (c) pit area fraction, (d) pit nearest neighbor distance, (e) intergranular corrosion area fraction, and (f) the total corrosion damage for an as-cast AE44 magnesium alloy exposed to salt spray and immersion environments, respectively. The model shows to be in good agreement with the experimental data illustrated by the individual damage mechanisms in figures (a)-(e). The AE44 alloy reached the transition time, t_y, in the salt spray environment at approximately 4 hours of exposure. In the immersion environment, the transition time, t_y, was approximately 12 hours of exposure.

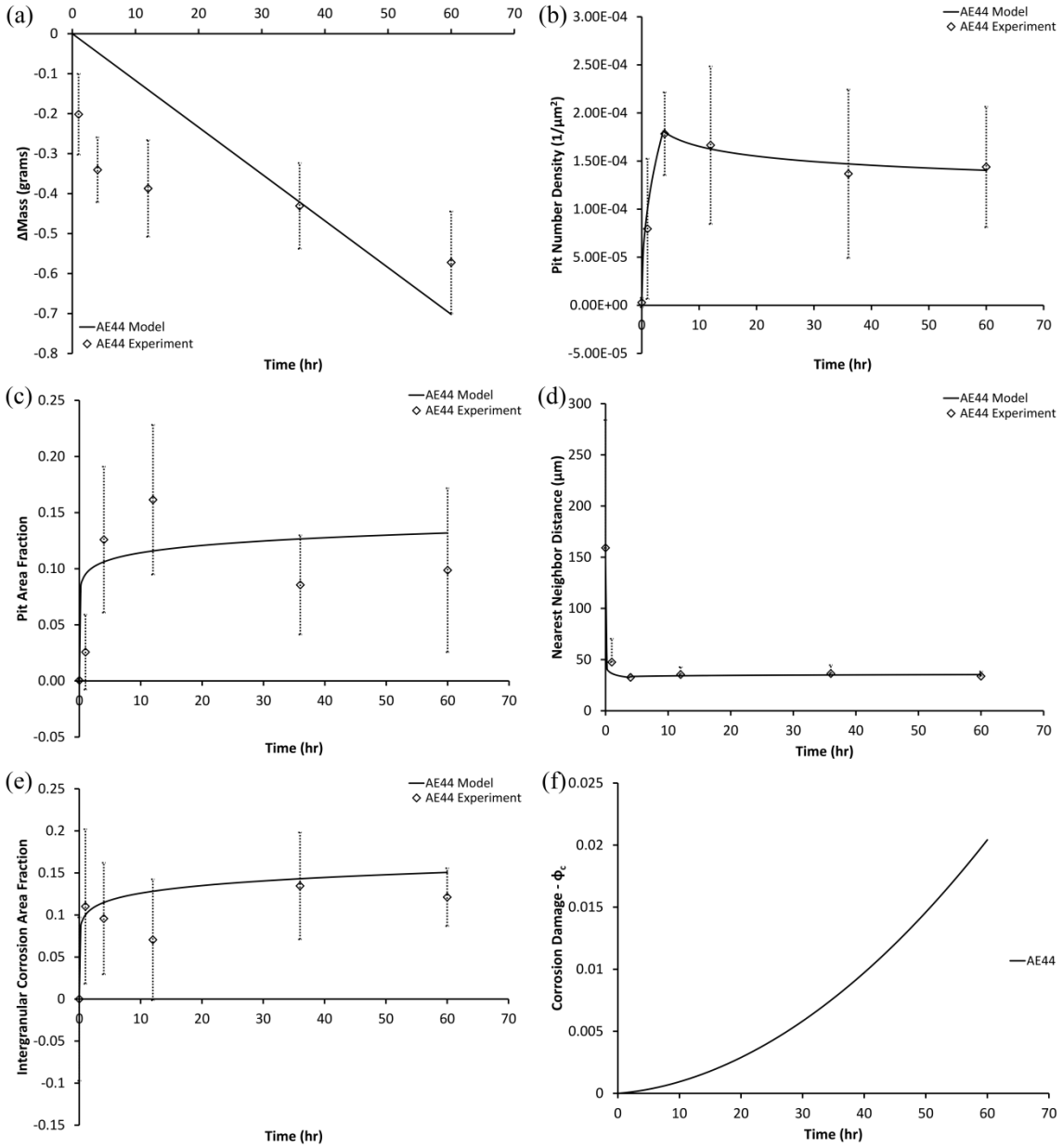

Figure 4.5 Model application for cast AE44 exposed to a 3.5 wt% NaCl salt spray environment.

The figure shows experimental data versus the model for (a) change in mass, (b) pit number density, (c) pit area fraction, (d) pit nearest neighbor distance, (e) intergranular corrosion area fraction, and (f) the total corrosion damage. The error bars were one standard deviation in each direction.

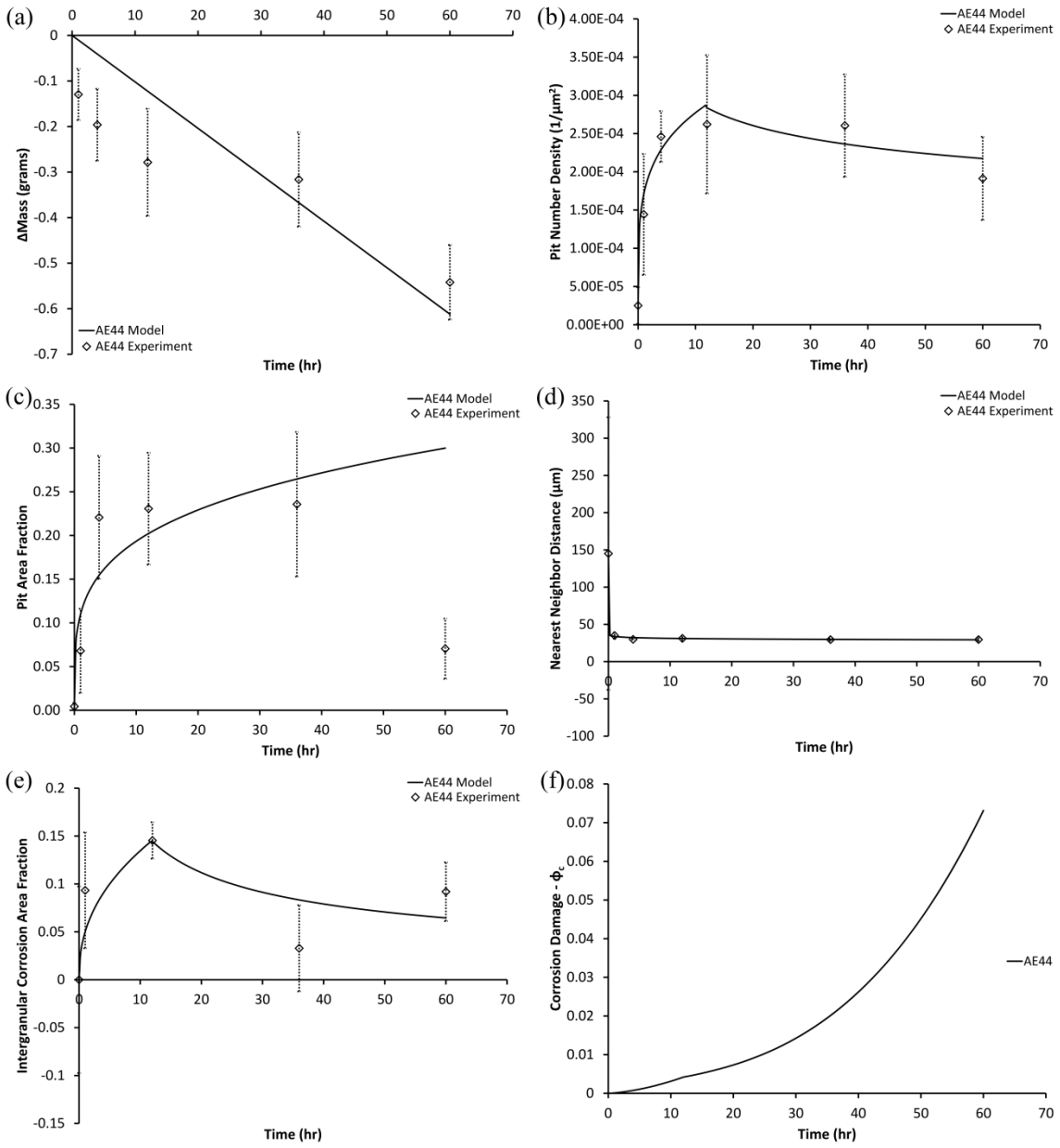

Figure 4.6 Model application for cast AE44 exposed to a 3.5 wt% NaCl salt spray environment.

The figure shows experimental data versus the model for (a) change in mass, (b) pit number density, (c) pit area fraction, (d) pit nearest neighbor distance, (e) intergranular corrosion area fraction, and (f) the total corrosion damage. The error bars were one standard deviation in each direction.

4.4 Conclusions

In this chapter, macroscopic corrosion damage presented in Chapter 3 was applied to five structural magnesium alloys exposed to an immersion and salt spray environment with a 3.5 wt% NaCl solution. The alloys studied were either extruded (AZ31, AZ61, AM30) or cast (AM60 and AE44). This chapter focused on the kinetics of the corrosion damage model that captured the effects of general corrosion, pitting corrosion (nucleation, growth, and coalescence), and intergranular corrosion. The material constants were determine based on a fitting-routine and shows that the model was able to appropriately produce a scalar damage variable that can be used for implementation into finite element code. In addition, it was shown that the proposed model is capable of predicting mass loss, pit number density per unit area, pit area growth, pit nearest neighbor distance, and the intergranular corrosion area fraction. The model's predictions were found to be mostly in good agreement with experimental observations. Moreover, macroscopic corrosion damage was successfully modeled.

CHAPTER V

CORROSION STRESS RELAXATION OF AN EXTRUDED AZ31 ALLOY

5.1 Introduction

As described in Chapter 3, the damage mechanism currently describing Mg alloys under simultaneous corrosion and stress environments is called SCC. The understanding of SCC is urgently needed because Mg alloys are being increasingly used in load bearing applications; many common Mg alloys have a threshold stress for SCC of half the yield stress in common environments including high-purity water [78]. Early reviews in the 1960s reported that alloying addition such as Al and Zn to wrought Mg alloys promoted SCC; thus wrought AZ alloys are susceptible to SCC for intermittent exposure to 0.01% NaCl and to the weather [78]. For AZ31, the SCC threshold stress is 40% of the yield stress in a rural atmosphere [78].

A literature review of Mg corrosion stress relaxation found little published material. Unigovski et al. [80] studied the effect of environment, stress, and test temperature on stress relaxation in pure Mg and die-cast Mg alloys (AZ91D, AM50, and AS21) where they found that pure Mg shows a crucial corrosion stress relaxation in 3.5 % NaCl solution at room temperature. Trojanová et al. in 2007 [93] studied the stress relaxation phenomena in AJ51 (Mg-5Al-0.6Sr) and AX41 (Mg-4Al-1Ca) Mg alloys. Trojanová et al. [94] followed that work with research on the AZ63 Mg alloy. The work

was primarily focused on analyzing the stress relaxation curves as a function of the internal stress at the beginning of the relaxation and the test temperature.

It is generally accepted for many metals that pit evolution under a corrosive solution is the dominant source for crack initiation and propagation. This is reasonable because pits cause local stress concentrations that increase the driving force for cracking. Because this assumption has fundamental significance for modeling, experiments have been conducted to investigate pit initiation and evolution for the AZ31 Mg alloy under 3.5% wt. NaCl aqueous solution. A cyclical salt spray test and immersion techniques were employed under a simultaneous stress relaxation deformation in an effort to expose the AZ31 Mg alloy to an environment similar to that experienced by automotive engine cradles. The experimental aims for this study were to determine the relaxation behavior of the AZ31 alloy under corrosive environments and to find direct or indirect evidence to support the assumption that pit evolution can lead to the crack initiation and material failure.

5.2 Materials and Methods

5.2.1 Set-up

Thirty-six AZ31 specimens were cut from an extruded sheet in the longitudinal direction. Table 1 lists the nominal [95] and specimen chemical composition by weight percent. The Fe pickup during the extrusion process is noticed, but is expected to have minimal effect with respect to the corrosion and mechanical properties. A schematic of the specimen geometry is illustrated in Figure 5.1a. In this study, corrosion was localized to one side of the specimen's gauge length. The corrosion surface of the specimens were left untreated, with no surface grinding or polishing, to test the corrosion effects on an as-

extruded AZ31 Mg alloy. The other side of the specimens were equipped with strain gauges to monitor an applied strain (Figure 5.1b). After the strain gauges were attached, all surfaces (excluding the corrosion surface) were covered with beeswax to prevent corrosion during the tests. For both environments (salt spray and immersion), three specimens per test environment were pinned in stress relaxation fixtures covered in beeswax (Figure 5.2). The specimens then were deformed to a true strain of approximately 80% of tensile yield stress.

Table 5.1 Nominal elemental composition of AZ31 versus the extruded alloy composition (in weight percent) used in this study

	Al	Zn	Mn	Si	Cu	Fe	Mg
Nominal AZ31 [95]	2.5-3.5	0.6-1.4	>=0.2	<=0.1	<=0.05	<=0.005	97
AZ31 Specimens	2.78	1.02	0.345	0.0063	0.0062	0.024	95.6

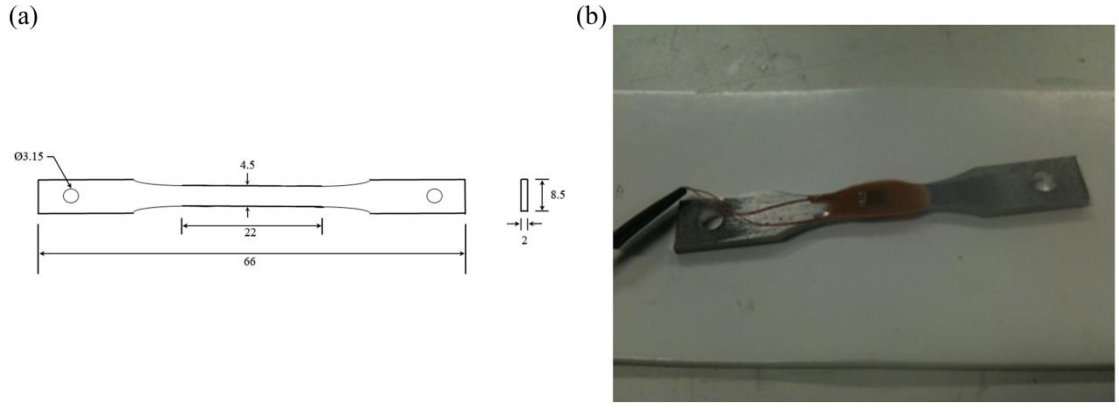

Figure 5.1 Specimen geometry and set up.

(a) Schematic of specimen used in this study and (b) a specimen equipped with strain gauge. All dimensions are in millimeters.

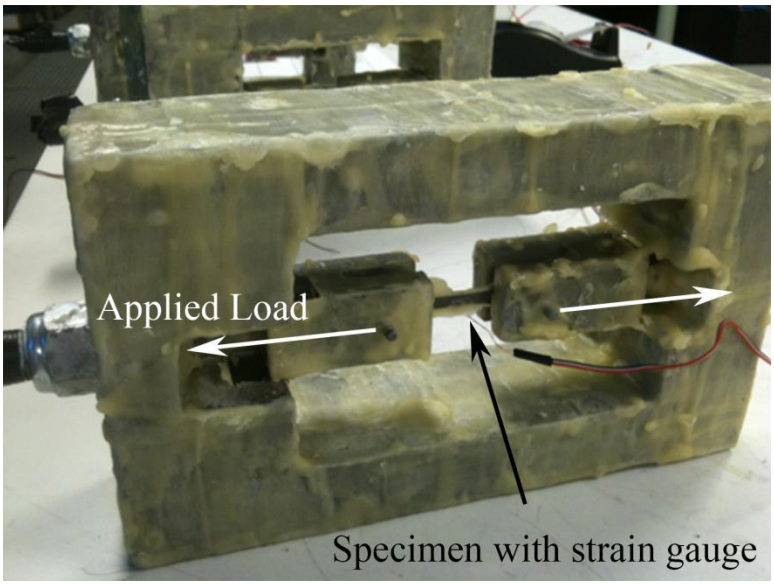

Figure 5.2 Experimental corrosion stress relaxation fixture setup.

The figure shows the load direction and specimen equipped with a strain gauge to monitor applied strain.

5.2.2 Environmental Exposure

Immediately following the applied strain, the specimens were exposed to the two different test environments for various times (t_0= 0 h, t_1= 1 h, t_2= 4 h, t_3= 12 h, t_4= 36 h, and t_5= 60 h), rinsed with distilled water to remove excess salt, and dried in a dessicator. For the cyclic salt spray testing, a Q-Fog CCT (Q-Panel Lab Products, Cleveland, OH) was used to cycle through three stages set at equal times, including a 3.5 wt.% NaCl spray at 35 °C, 100% humidity using distilled water at 35 °C, and a drying purge at 35 °C. For immersion testing, an aquarium filled with 3.5 wt.% NaCl solution at room temperature was used. For the tests, one set of immersion and salt spray specimens were exposed to the test environment for 1 h, removed, rinsed with distilled water to remove excess salt, dried, and then examined under an optical microscope. Following the optical analysis, the coupons were then placed back into the test environment for an additional 3

h, an additional 8 h, an additional 24 h, and another 24 h; the samples were removed, cleaned, and examined after each time period. These times allowed for a longitudinal study to follow pit growth and surface changes over time.

5.2.3 Surface Analysis and Fractography

Optical microscopy with an inverted light was used to take multiple images of the resulting corrosion surface at 10x magnification (Axiovert 200M Mat, Carl Zeiss Imaging Solutions, Thornwood, NY). The 10x magnification was used to pictorially show the changes over the six cycles. Scanning electron microscopy (FEG-SEM, Zeiss SUPRA 40) coupled with energy dispersed X-Ray spectroscopy (EDS) was used to examine the resulting tension tests fracture surfaces, the localized corrosion pits, and corrosion products.

5.2.4 Data Analysis and Fractography

Due to the inability to monitor load while the specimens were in the immersion and salt spray environments, the stress relaxation data points were gathered at the given interval times following tension testing. This meaning that stress calculations during the relaxation tests were not done, but were interpolated based off of the known strain value on the stress-strain relationship. Since the applied strain for the relaxation tests was in the elastic regime of the AZ31 stress-strain relationship, backing out the stress at the given strain after reloading should theoretically give an accurate stress picture over time. It is important to note that one might expect slightly different results when comparing intermittent loading (capturing stress following unload) with continuous loading (monitoring stress while exposed) due to plastic microdeformation in the relaxation

process. A baseline, or control, specimen was run in air for the 60 hour time for comparison, but with an Instron electromechanical test machine recording stress over time.

After the combine corrosion and stress relaxation tests, tensile tests were performed using an electromechanical Instron 5882 machine at a constant strain rate of 0.001/s. The machine was equipped with a 5 kN load cell. For each tested time and environment, stress-strain data was garnered for three specimens, for a total of six samples per time. For the cross-sectional area used for true stress calculations, corrosion damage was taken into consideration. A thickness loss and average pit depth measurement allowed for an approximation of the cross-sectional area at the interval times. The stress-strain data gathered was analysed using the Data Averager (v. 2.5) developed by Mississippi State University to determine average stress-strain plots. The Data Averager was set to interpolate over 2000 strain values to get the most accurate curve.

5.3 Results

5.3.1 Corrosion Stress Relaxation and Monotonic Tension Testing

Corrosion stress relaxation tests were carried out for 60 hours on the AZ31 Mg alloy specimens. Figure 5.3 shows the normalized time-dependent stress ($\sigma(t)/\sigma_0$) decrease for the 60 hour testing matrix. $\sigma(t)$ is the current relaxation stress and σ_0 (t=0) is the initial value of stress. This represents the stress relaxation relationship for the air (control), salt spray environment, and immersion environment specimens. The control specimen ran at room temperature shows a relaxation effect but begins to reach a steady-

state around 20 hours. The salt spray environment shows an approximate 60% reduction of static strength over the 60 hours. In the salt spray environment, the stress percent drop is not as significant as in the immersion environment. The immersion environment has a stronger deleterious effect immediately. After one hour, notice that there is approximately a 25% reduction of static strength. After the 60 hours, the specimens exposed to the immersion environment were completely corroded through the thickness. To compare the salt spray and immersion environment, the normalized stress against the wet time in the salt chamber has been plotted. Also, the stress relaxation of pure Mg in air [80] is plotted for comparison to the AZ31 alloy in air. Notice that pure Mg and AZ31 closely follow the same trend.

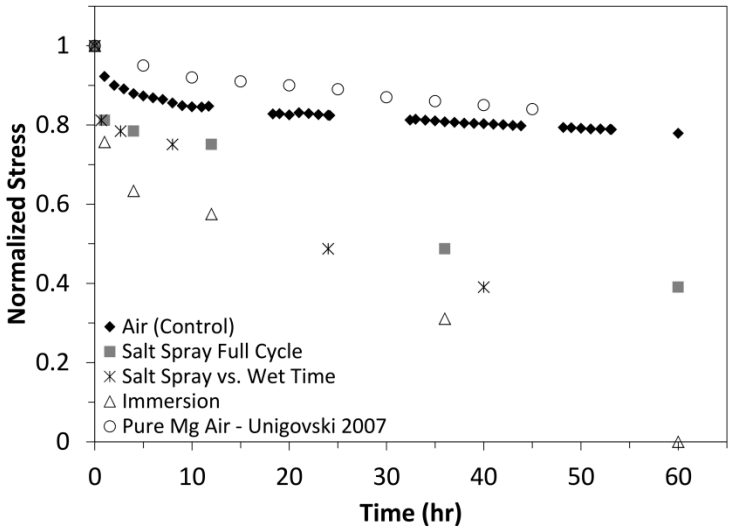

Figure 5.3 Normalized stress relaxation of AZ31 Mg alloy specimens at room temperature in air (control), a 3.5 wt.% NaCl salt spray fog environment, and a 3.5 wt.% NaCl immersion environment.

The constant strain value was approximately 80% of the tensile yield strength. The salt spray data versus wet time in the salt chamber has been plotted for comparison. Stress relaxation data of pure Mg in air under a constant strain of 70% of the tensile yield strength is plotted for comparison [Y. Unigovski et al., 2007].

Following the corrosion stress relaxation, tensile tests until failure were performed. Figure 5.4 illustrates the average stress-strain relationship curves for the salt spray (Figure 5.4a) and immersion (Figure 5.4b) environments compared to the stress-strain response of AZ31 in air. Since the immersion specimens tested 60 hours corroded through the thickness, no plot is available. Notice that the salt spray environment had a minimal effect on the tensile yield strength and elongation to failure. The difference between the curves was less than 10% for all averaged curves. On the other hand, a noticeable reduction of both tensile yield strength and elongation to failure is illustrated in the immersion environment stress-strain plots.

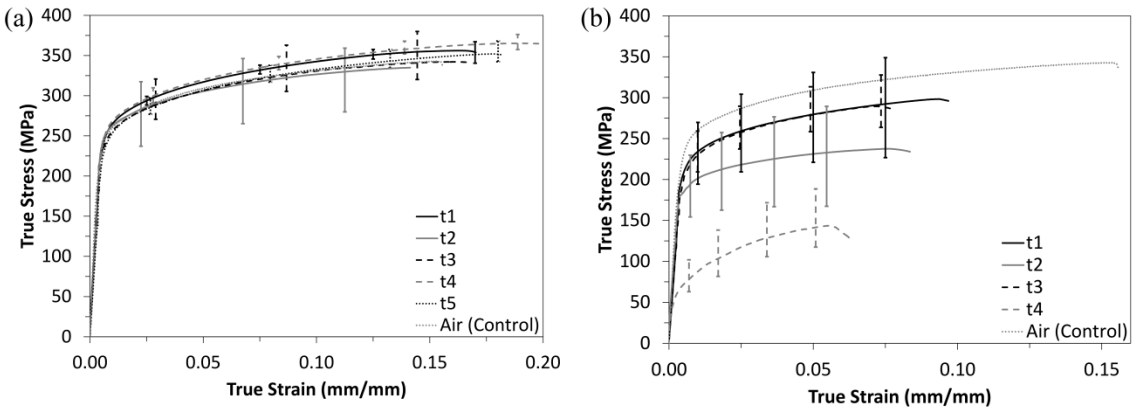

Figure 5.4 Monotonic tensile true stress-true strain response of the AZ31 Mg alloy following corrosion stress relaxation testing in the (a) salt spray and (b) immersion environments at t_1= 1 h, t_2= 4 h, t_3= 12 h, t_4= 36 h, and t_5= 60 h.

A benchmark control specimen was run in laboratory air for comparison. All tests were run at room temperature and a strain rate of 0.001/s.

5.3.2 Fractography

Following the tension tests, the failure surfaces were imaged using SEM to examine the effects of pit formation with respect to fracture. Figure 5.5a shows the

fracture surface of a salt spray specimen at t_1. It is evident that pit formation had begun to occur at the corrosion surface and was a contributing factor in failure during the tension test. Figure 5.5b shows one of the pits magnified. For the salt spray specimen at t_2 (not shown), the failure mode was in a very similar manner to t_1.

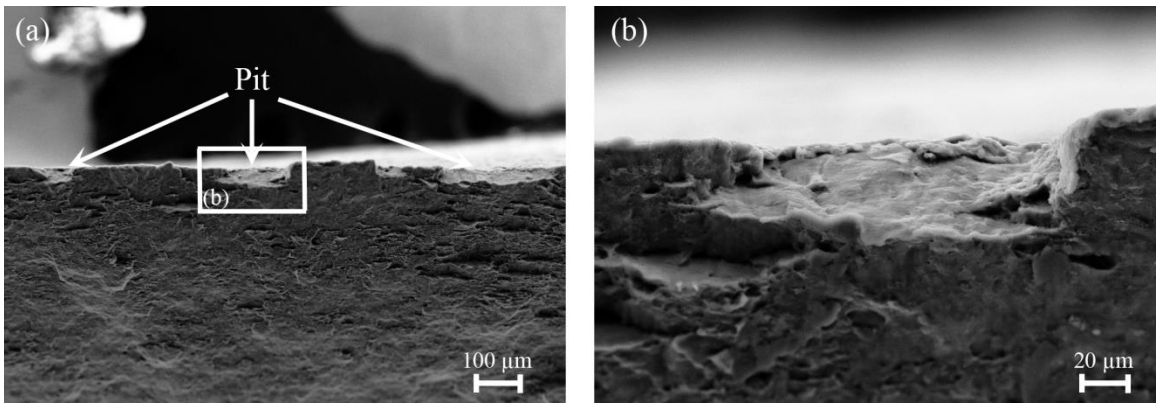

Figure 5.5 SEM micrographs of a salt spray corrosion-stress relaxation specimen (t_1 = 1 h) fracture surface.

The figure shows (a) pits across the corrosion surface and (b) a magnified image of one of the pits. Notice that no cracking is evident in the micrographs.

Figure 5.6 shows the fracture surface of a salt spray specimen at t_3. The initiation site of this fracture was due to a combined corrosion pit formation and Al-Mn intermetallic particles at the corner of the specimen. Similarly, the salt spray t_4 (not shown) specimen failure initiated at a pit and could have been influenced by the Al-Mn intermetallic particles as well. As time increase with the salt spray specimens, pit formation did not increase as fast as the immersion specimens but corrosion products were observed on the corrosion surfaces.

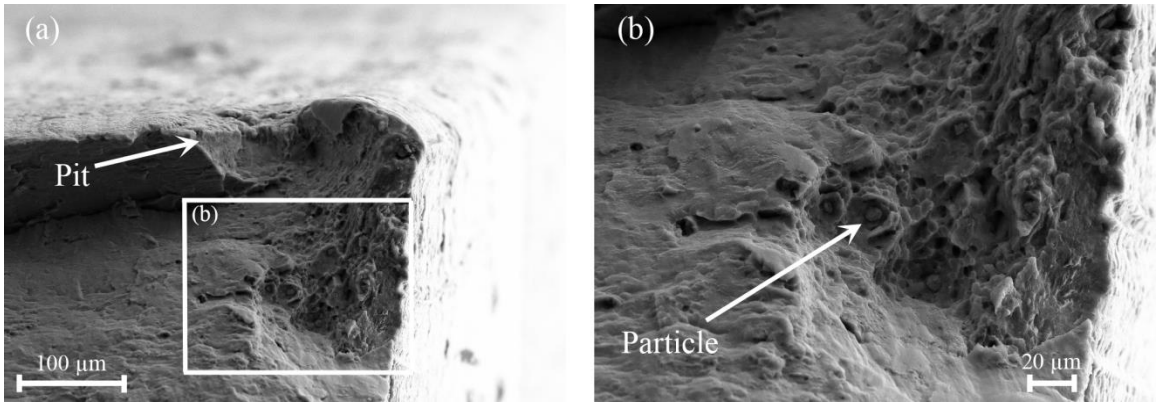

Figure 5.6 SEM micrographs of a salt spray corrosion-stress relaxation specimen (t_3 = 12 h) fracture surface.

The figure shows (a) the pit at the corner of the specimen in which failure initiated and (b) Al-Mn intermetallic particles trapped within the AZ31 Mg matrix material which aided the fracture at this point.

Figure 5.7 shows the fracture surface of a salt spray specimen at t_5. The corrosion product can be seen in Figure 5.7a and the pit formed in Figure 5.7b.

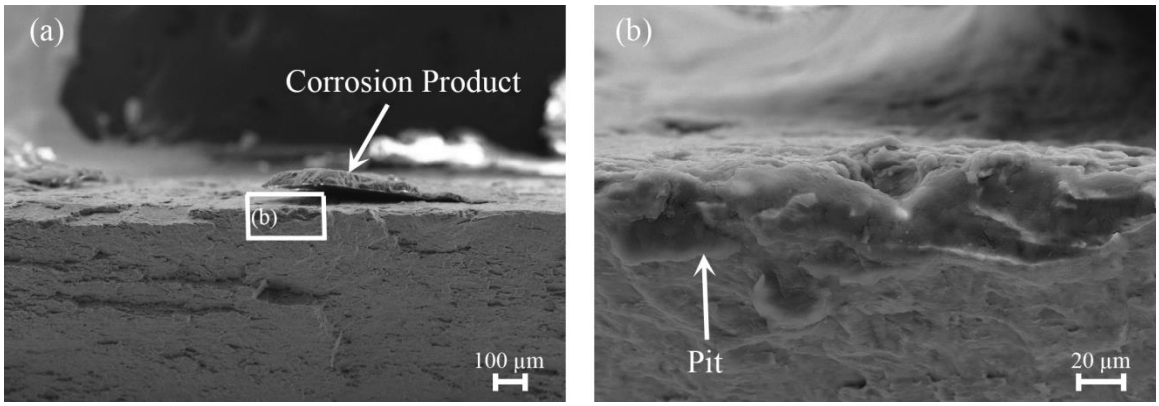

Figure 5.7 SEM micrographs of a salt spray corrosion-stress relaxation specimen (t_5 = 60 h) fracture surface.

The figure shows (a) a pit on the edge and corrosion reaction product on the corroded surface. The pit formed below the product is shown at a (b) higher magnification.

Similar SEM imaging was complete for the immersion fracture surfaces. Figure 5.8 shows the fracture surface for an immersion environment specimen at t_1. Pit formation was seen at the corrosion surface fracture edge (Figure 5.8a). The failure of this specimen was caused by the stress concentrations added by the defects on the surface. Cleavage fracture at the corner of the corrosion surface and the surface covered in beeswax (Figure 5.8b) showed to be the initiation site of this failure.

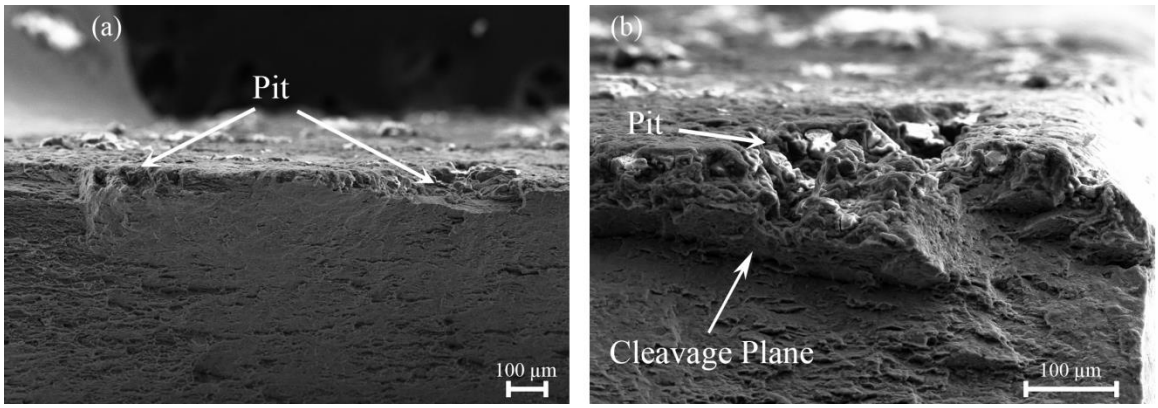

Figure 5.8 SEM micrographs of an immersion corrosion-stress relaxation specimen (t_1 = 1 h) fracture surface.

showing (a) pits across the edge and (b) a pit at the corner of the specimen where failure initiated.

Figure 5.9 shows the fracture surface of an immersion specimen at t_2. Oxide film (corrosion product) rupture was observed within the pits and shown in Figure 5.9b.

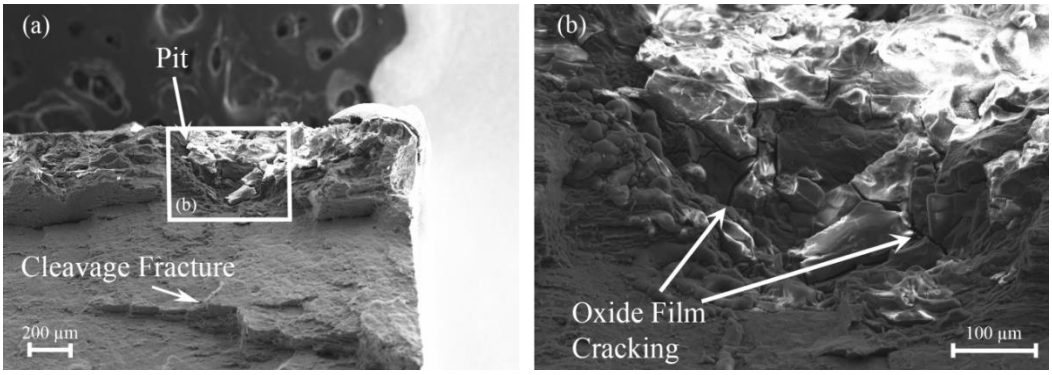

Figure 5.9 SEM micrographs of an immersion corrosion-stress relaxation specimen (t_2 = 4 h) fracture surface.

The figure shows (a) the pit at the corner of the specimen where failure initiated and (b) evidence of the oxide film cracking within the pits. This confirms that pitting-induced hydrogen embrittlement begins to affect the Mg alloy in the immersion environment.

Figure 5.10 shows the fracture surface of an immersion specimen at t_3. The damage seen was concentrated at the corners of the specimens caused by pits. Looking into a pit as shown in Figure 5.10a, oxide film rupture and a possible vent for entrapped gases is observed. The vent-like structure in the pit is highlighted and magnified in Figure 5.10b.

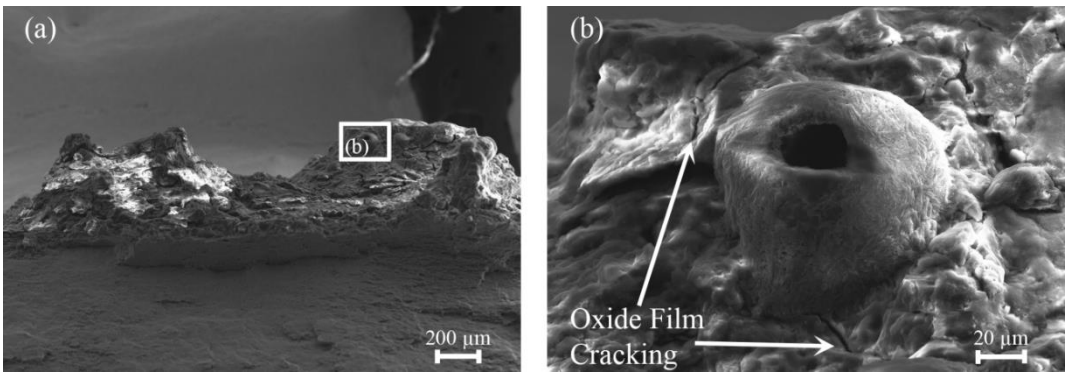

Figure 5.10 SEM micrographs of an immersion corrosion-stress relaxation specimen (t_3 = 12 h) fracture surface.

The figure shows (a) the strong effects of general and pitting corrosion over time and (b) a vent-like structure formed to release trapped gas within the AZ31 Mg matrix material.

Figure 5.11a shows the overall fracture surface of an immersion specimen at t_4 which shows the degradation (general corrosion) of the specimen very well. One can notice that the specimen edges corroded away while some of the bulk material stayed attached. Figure 5.11b shows that oxide film cracking was observed at this time. Figure 5.11c and 5.11d provides evidence of SCC on the fracture surface. As stated before, the specimens at t_5 corroded completely through the thickness so no imaging was performed.

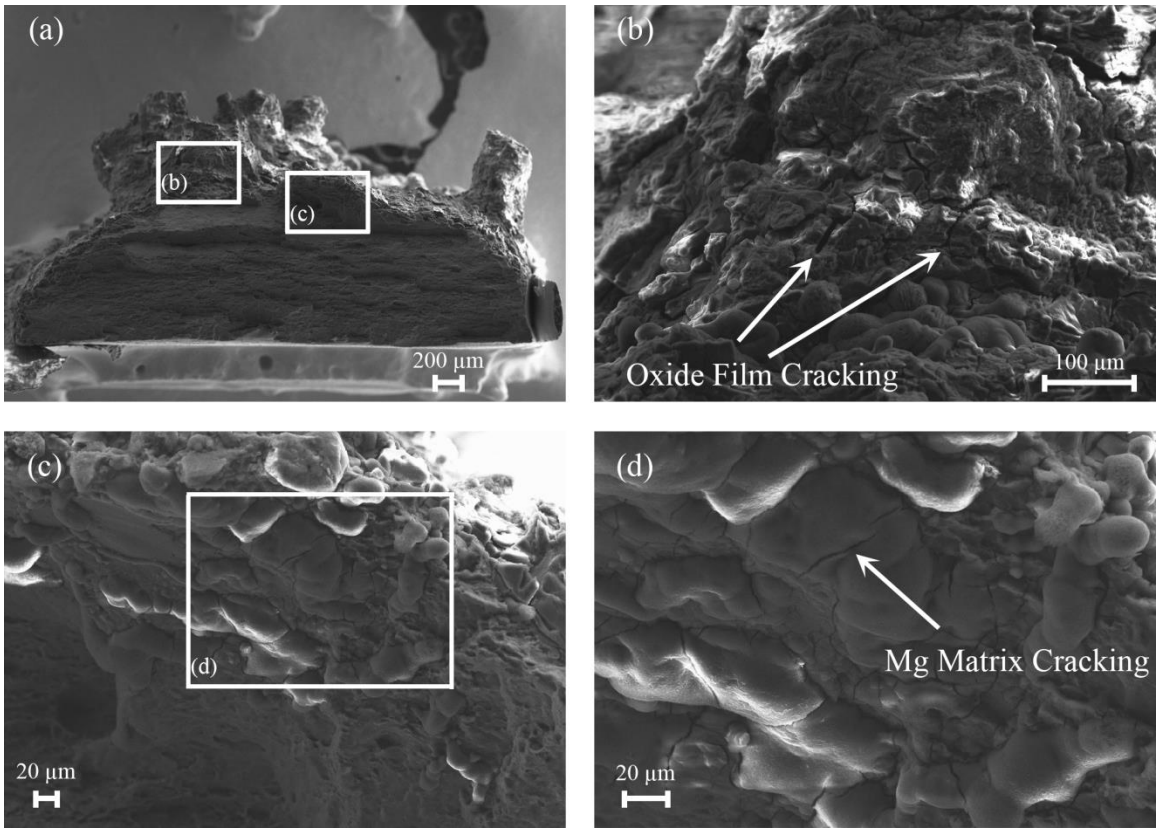

Figure 5.11 SEM micrographs of an immersion corrosion-stress relaxation specimen (t_4 = 36 h) fracture surface.

The figure shows (a) the overall specimen cross-sectional area, (b) evidence of the oxide film cracking in a large corrosion pit, and (c) evidence of stress corrosion cracking within the AZ31 matrix material magnified in (d). Notice that approximately half of the cross-sectional area has been corroded which in turn reduces the amount of load bearing area during the tensile test.

5.3.3 Corrosion Surface Morphology

Figure 5.12 and 5.13 pictorially shows the changes in surface characteristics using micrographs over 60 hours for both the salt spray environment and the immersion environment, respectively. The figures are arranged to show the changes between the surfaces covering an area of approximately 1 mm by 1 mm with the scale bars of 1000 μm for each of the time examined, where t_0= 0, t_1= 1 h, t_2= 4 h, t_3= 12 h, t_4= 36 h, and t_5= 60 h, and to show the differences in the pits between the salt spray and immersion environments. The black lines running vertically in the micrographs on both samples were a result of the extrusion process. The surfaces were not polished to examine the effects of the as-extruded condition. When examining the salt spray surface, pits began to form between t_0 and t_2 shown by the black areas forming on the surface. From t_3-t_5, one can see that the pits began to grow in size. When examining the immersion surface, general and intergranular corrosion was observed between time t_0 and t_1 indicated by pit growth along grain boundaries. This is evidence of IGSCC. After t_1, pits grew in size significantly through t_3. Following t_3, a new surface was noticeable by the disappearance of the extrusion lines on the micrographs. No surface was available at t_5. The blurry white areas are where NaCl collected in the pits and all other blurry areas are pits. The larger pits are blurry due to the depth of field on the microscope not being large enough at such magnification.

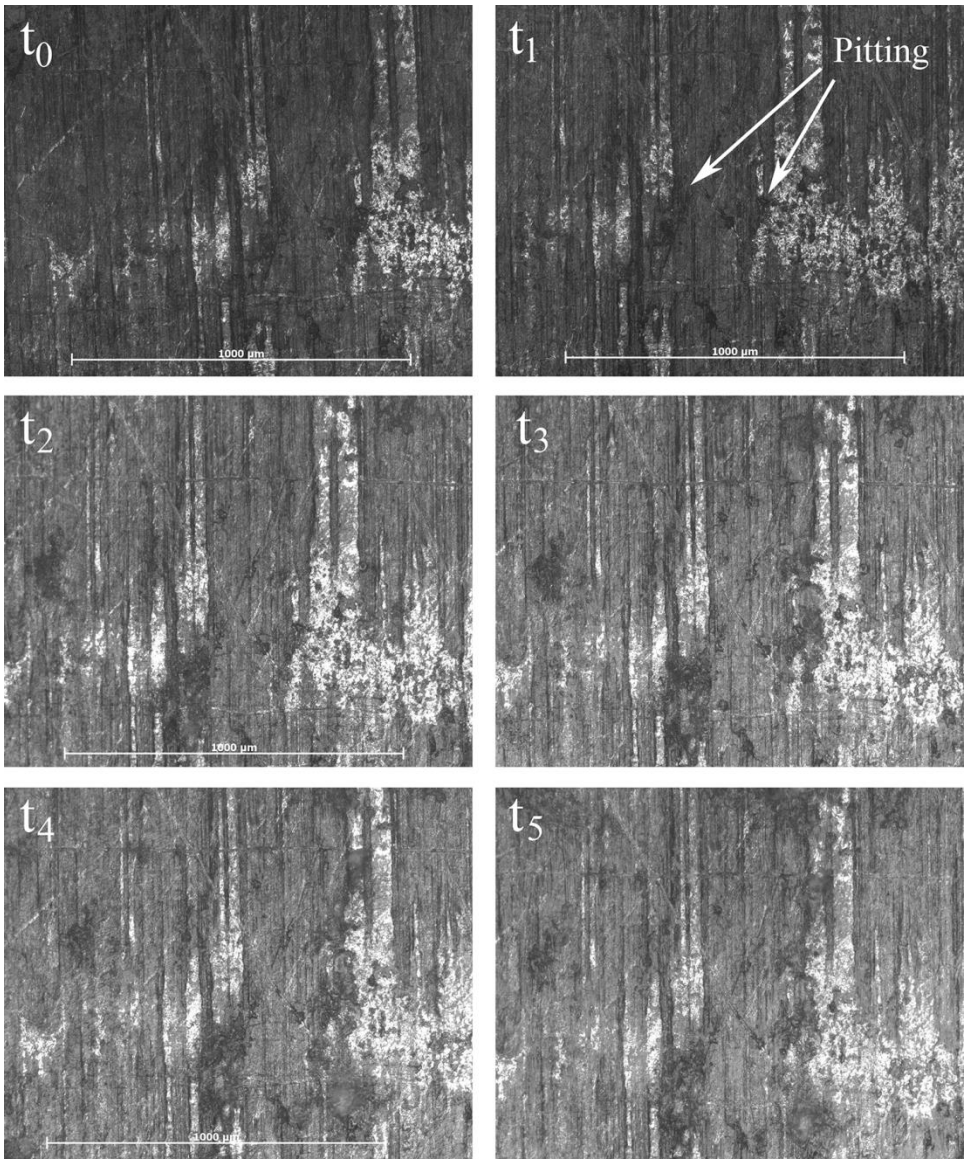

Figure 5.12 Micrographs of the corrosion-stress relaxation salt spray surface over 60 hours.

All spots were examined over approximately 1 mm x 1 mm area, with scale bars of 1000 µm each. The darker areas indicate pit formation and coalescence.

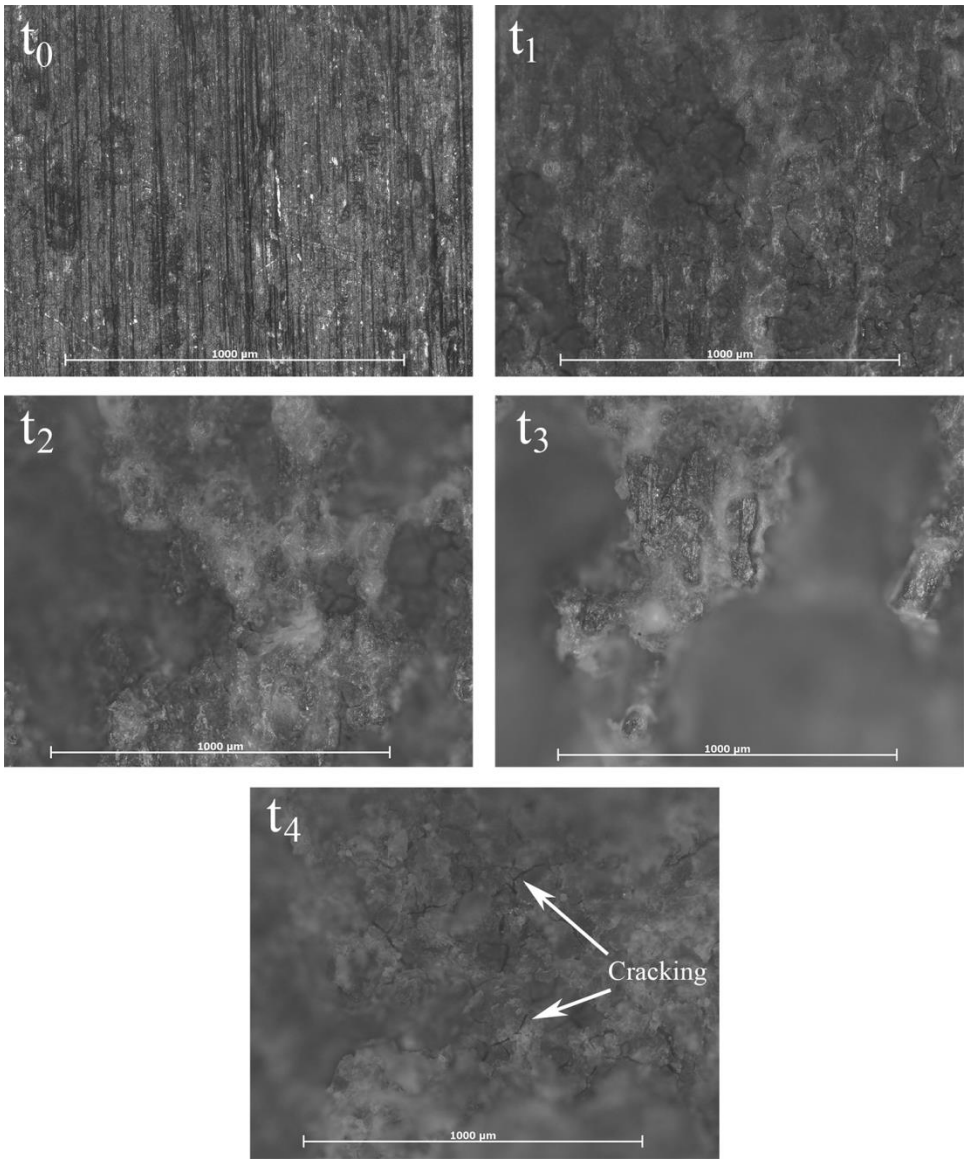

Figure 5.13 Micrographs of the corrosion-stress relaxation immersion surface over 36 hours.

All spots were examined over approximately 1 mm x 1 mm area, with scale bars of 1000 µm each. The darker areas indicate pit formation and coalescence, while the lighter areas indicate surfaces closer to the light and those affected by general corrosion. Notice that the pits grew in number and area through t_1.

5.4 Discussion

Stress relaxation of a material is typically defined as a decrease in stress under constant strain and constant temperature. For Mg, this is primarily due to slip in the basal plane [96]. As the microstructure dislocation density increases, the stress needed to hold the specimen at a given strain decreases. Unigovski et al. proposed [80] a connection between the stress relaxation mechanism and the evolution of dislocation substructure at the expense of relieving inner stresses by plastic microdeformations. When simultaneously exposing the material to corrosion and mechanical loading, this behavior is expected to increase the relaxation rate (slope of the curve at any point). The change in physical-mechanical properties and fine microstructure of a solid under the influence of chemical reactions, including HE, which proceed on specimen surfaces causing additional dislocation flux is called the chemomechanical effect [80]. The additional dislocation flux results from the dissolution of surface atoms, which promotes the dislocation relaxation process and additional plasticity [97]. Figure 5.3 shows the normalized stress of the specimens versus time for the salt spray, immersion, and air environments. In all of the tested environments, a reduction of static stress over time was observed. The effect of the two different corrosion environments, salt spray and immersion, was captured. As a benchmark, a relaxation test was run at room temperature in laboratory air. The control specimen relaxation rate appears to be similar to polycrystalline magnesium (99.9653% Mg) stress relaxation reported by Unigovski et al. [80]. The differences between the curves can be explained by the material used (pure versus alloyed Mg) and applied strain. Unigovski et al. [80] applied a strain of approximately 70% of the tensile yield strength. In this study, specimens were loaded to

80% of the tensile yield strength. The stress continually decreases for the control specimen, but at a very slow rate compared to the salt spray and immersion environments. Also, after 60 hours the applied stress on the specimen was approximately 80 percent of the initial stress. Conversely, the salt spray and immersion environments normalized stress decreased rapidly throughout the 60 hours. This indicates that the corrosion environments have a major effect on the strength of the material over time. The immersion environment has a more deleterious effect compared to the salt spray environment confirmed by the optical microscopy (Figures 5.12 and 5.13) and SEM imaging. The relaxation rate for the immersion environment as compared to the salt spray environment is greater.

For the immersion environment, the specimens corroded completely through by the end of the 60 hour testing matrix. The apparent very strong relaxation effect is a result of the nature of the immersion environment and confirms that the specimens experienced significant damage throughout the exposure time. The continuous presence of water allowed the corrosion by-products to dissolve, as $Mg(OH)_2$ is water soluble, and also kept the salt suspended [92]. The inability of the pit debris and salt residuals to remain on the surface meant that material was removed from the Mg surfaces.

Although the effect of the salt spray environment was less deleterious, a constant decrease in normalized stress was observed. For the environment, chloride ions were only exposed to the surface briefly during the salt spray phase of the cycle compared to the immersion surfaces. The chloride ions could react with the surface only during that cycle phase. Next, the humidity phase introduced salt-free water to the surface. The humidity phase helped pits grow by causing condensation, which removed some chloride

ions, but the condensed water could also diffuse into the pits without being able to diffuse out. The presence of the water and chloride ions continued to react with the Mg even during the drying phase, allowing the pits to grow unabated, even without additional chloride ions. The drying phase also stopped general corrosion and dried any corrosion and pit debris onto the surface, trapping the chloride ions inside the pits allowing pits to grow unabatedly. For comparison to the immersion environment, the salt spray versus wet time (pollution and humidity) was plotted (Figure 5.3). This shows that the effect of an aqueous environment over time.

When examining the tensile strength of the specimens, Figure 5.4 shows the average stress-strain response for the salt spray (Figure 5.4a) and immersion (Figure 5.4b) environments compared to the stress-strain response in air. The effect of the environments was clear in the stress-strain study. A limited effect was noticed for the salt spray specimens and can be supported by the micrographs (Figure 5.12). The micrographs show pits forming on the surface but with little growth into the surface. Over the 60 hours, pit growth on the surface is noticed but was not as significant as the previous AZ31 salt spray corrosion study completed by Walton et al. [92]. The major difference was the testing angle of the samples. Walton et al. [92] hung the specimens at 20° to horizontal compared to the stress relaxation cradle being set horizontal for this study. The stress relaxation cradle surrounding the specimen could have hindered the NaCl solution from reaching the surface during tests. If this occurred, that would explain why pits formed at a slower rate. Conversely for the immersion environment (Figure 5.4b), the time in the corrosion bath played a large role in the response. A noticeable reduction of both tensile yield strength and elongation to failure is illustrated by the

stress-strain plots except for t_3. From t_2 to t_3, an average tensile strength increase was observed. One would expect a decrease following a trend similar of the difference of t_1 and t_2. Notice the large error bars for t_3. This demonstrates that an outlier of the group of three specimens caused the plotted increase of strength. If the outlier is removed, the expected trend would be seen. Also, t_2 error bars show that the three specimens were in a wide range as well. The large variation within the data can be explained by the unpredictable corrosion nature of the environments with relation to the material microstructure. Although each specimen was cut from the same sheet of material, the smallest changes between microstructure can cause large strength changes. In addition, the extrusion process adds inherent defects on the surface which aided in large variations of results.

The stress-strain response for both environments is greatly influenced by the damage the specimens occurred over the testing time. The qualitative observation in this study showed evidence of multiple corrosion damage mechanisms. The most prominent fracture surface mechanism and characteristic for both environments was pitting at the corners of the specimens. The corner of the specimen is where the waxed and un-waxed surfaces meet. This is shown in Figures 5.6 and 5.8-5.11. The increase in chloride ion concentration along the edges would lead to an increase in corrosion and stress risers during tensile testing. The specimens were tested horizontally, which allowed the water containing salt to settle on the edges of the coupons. In addition to the salt build-up, Al-Mn particles (Figure 6b) within the Mg matrix material show to have a potential effect on the fracture location. In literature, Matsuoka et al. [98] reported that the addition of too much Mn resulted in a reduction of tensile properties due to the formation of large Al-Mn

particles. Another evident damage mechanism observed while looking at the fracture surfaces (cross-sectional area) was general corrosion. General corrosion in this manuscript is described as the thickness loss. General corrosion was seen mostly on the immersion specimens and explains the reduction of both tensile yield strength and elongation to failure. For example, looking at the immersion specimens from t_2 (Figure 5.9) to t_4 (Figure 5.11) shows that much of the bulk material was lost over the additional 32 hours immersed. Similar to the effects on the relaxation curve previously described, the continuous presence of water allowed the corrosion by-products to dissolve leading to the general corrosion of the Mg surfaces and the decrease in the observed thickness.

An important area of interest that was observed within the failure initiating corrosion pits for the immersion specimens (Figures 9b, 10b, and 11b) was rupture of the oxide film. As stated above, this oxide film dissolves over time. When the film ruptures or cracks, this becomes an area where corrosion is being localized at the underlying Mg matrix. For the immersion environment, this can cause larger pits and subsequently, higher stress risers during mechanical tests. For example, Figure 8b shows a vent-like structure formed within a pit. At the base of the structure, the film ruptured to release trapped gas but at the same time allow the NaCl solution to locally corrode at that location.

The last evident corrosion mechanism observed was SCC, both TGSCC and IGSCC. SCC is simply defined as the growth of cracks in a corrosive environment [99]. This mechanism showed to be the most important with respect to the strength and apparent plastic deformation. Within the failure initiating corrosion pits, cracking of the Mg matrix material can be seen (Figure 5.9-5.11) for the immersion specimens. The

hydrogen-induced cracking is typical for continuously-exposed samples [100]. SCC is described as an anodic dissolution assisted cracking which is accompanied by a hydrogen reduction reaction [100]. Hence, hydrogen ions are readily available for diffusion into the metal which can then lead to HE [100]. In previous research, Mg alloys have been susceptible to environmentally-assisted induced failure. Pardue et al. [101] reported that pitting corrosion in an AZ61 alloy induced cleavage cracks. Stampella et al. [102] suggested that atomic hydrogen in solid solution of Mg facilitates cleavage fracture as well. Figure 8b and 9a show evidence of pits and cleavage fracture. SCC was not observed until 36 hours of exposure in the immersion environment. On the fracture surface, directly below the corrosion surface, cracking in the Mg matrix material was noticed (Figure 11c). Figure 11d highlights a transgranular crack, but the micrograph shows evidence of many cracks in the matrix material.

Exposing the AZ31 alloy to corrosion environments clearly effects the relaxation and mechanical performance. When combining chemical and mechanical loading, one can observe degradation of the alloy due to macroscopic damage mechanisms (general corrosion, pitting corrosion, and SCC) and atomistic effects (hydrogen embrittlement). The damage incurred subsequently drives mechanical performance down. Although the immersion environment replicates the "worst-case" scenario, it shows that constant exposure to a corrosive aqueous solution can be detrimental to latter performance.

5.5 Conclusion

A synergistic effect of the corrosion and stress on the monotonic tensile properties using an extruded AZ31 Mg alloy was studied over 60 hours. This chapter focused on

the corrosion stress relaxation effects, corrosion damage mechanism effects, and surface fractography on an extruded AZ31 Mg alloy under two different environments: cyclical salt spray and immersion. The following conclusions can be taken from this study:

1. The corrosion-stress relaxation effect on the AZ31 Mg alloy is greater than that of pure Mg. This indicates that the composition of the alloying elements for this ternary do not enhance creep properties.
2. When examining environmental dependence, the relaxation rate for the immersion environment as compared to the salt spray environment is greater.
3. The salt spray environment showed a minimal stress-strain relationship effect due to the cyclic nature of the salt chamber potentially aided by the stress relaxation fixture. Conversely, the constant contact with the salt solution in the immersion environment during the 60 hours promoted significant reduction of strength and elongation to failure of the specimens.
4. It is suggested that the hydrogen enhanced dislocation mobility over time causes the noticeable reduction of strength in the stress-strain relationships.
5. The highest sensitivity to general corrosion (thickness loss) and SCC was observed in the immersion environment. Cracking of the Mg matrix material was noticed after 36 hours of exposure.

CHAPTER VI

SUMMARY

6.1 Research Observations

In summary, the differences in the corrosion mechanisms on an extruded AZ31 Mg alloy under two different environments, cyclical salt spray and immersion, were quantified using optical microscopy and laser profilometry techniques. The data garnered from the experimental corrosion testing of the AZ31 alloy, plus studies completed on four other Mg alloys (AZ61, AM30, AM60, and AE44) by our group, were used to calibrate and eventually validate the model. The corrosion model presented in this dissertation is the first of its kind. The corrosion ISVs are essentially added to the thermomechanical plasticity-damage model of Bammann [32–34] and Horstemeyer [35,40] but includes electrochemical environments using conservation laws and empirical relationships. The creation of this model will eventually allow researchers to implement environmental damage into complex FE codes. As a stepping stone for future work, chemomechanical testing was done on the AZ31 alloy to determine the simultaneous effects of mechanical and chemical loads. The test included a stress relaxation procedure where specimens were pulled to a strain of approximately 80% of the initial tensile yield strength then placed in the aggressive immersion and salt spray corrosion environments. Following the stress relaxation tests, the specimens were placed under a monotonic tensile test to failure

to determine the strength of the alloy over time. Also, SEM observations confirmed that AZ31 is highly susceptible to SCC.

6.2 Peer Reviewed Publications

- **C.A. Walton**, H.J. Martin, M.F. Horstemeyer, P.T. Wang. "Quantification of Corrosion Mechanisms Under Immersion and Salt-Spray Environments on an Extruded AZ31 Magnesium Alloy." *Corrosion Science* 56 (2012) 194-208.
- **C.A. Walton**, B.E. Nesbit, H.M. Candia, Z.A. Myers, W.R. Whittington, T.W. Stone. "Failure analysis and mechanical performance evaluation of a cast aluminum hybrid-iron golf club hosel." *Journal of Failure Analysis and Prevention* 13 (2013) 561-569.
- H.J. Martin, **C.A. Walton**, J. Danzy, M.F. Horstemeyer, P.T. Wang. "Quantification of Corrosion Mechanisms Under Immersion and Salt-Spray Environments on an As-Cast AZ91 Magnesium Alloy." *Corrosion*. In Review.
- W. Song, H.J. Martin, A. Hicks, D. Seely, **C.A. Walton**, W. Lawrimore, P.T. Wang, M.F. Horstemeyer. "Corrosion Behaviour of Extruded AM30 Magnesium Alloy under Salt-Spray and Immersion Environments." Accepted.
- **C.A. Walton**, H.J. Martin, M.F. Horstemeyer, W.R. Whittington, C.J. Horstemeyer, P.T. Wang. "Corrosion Stress Relaxation and Tensile

Strength Effects in an Extruded AZ31 Magnesium Alloy." Resubmitted after Revision 1.

- **C.A. Walton**, M.F. Horstemeyer, H.J. Martin. "Formulation of a Macroscale Corrosion Damage Internal State Variable Model – Application to Magnesium Alloys." Resubmitted after Revision 1.
- **C.A. Walton**, M.F. Horstemeyer, H.J. Martin. "Application of a Macroscale Corrosion Damage Internal State Variable Model to Magnesium Alloys of Different Ternaries and Forms." In Preparation.

6.3 ICME Cyber-Infrastructure Contributions

- Quantification of AZ31 Corrosion Mechanisms *https://icme.hpc.msstate.edu/mediawiki/index.php/Quantification_of_corrosion_mechanisms_on_an_extruded_AZ31_magnesium_alloy*
- Macroscale modeling section – metals/material modeling/add corrosion modeling

CHAPTER VII

FUTURE WORK

7.1 Model Implementation into Finite Element Code

As illustrated in Chapter III and IV, a fundamental model for macroscopic corrosion damage has been presented. It is suggested that the kinetics of the corrosion damage be coded in FORTRAN for easier implementation in the current MSU ISV Plasticity-Damage model that is coded for use in the Abaqus FE software. In addition, the corrosion model can be implemented using the Multiphysics Object Oriented Simulation Environment (MOOSE) with the Abaqus UMAT interface tool.

7.2 Additional Chemomechanical Testing and Modeling

As illustrated in Chapter V, chemomechanical testing determines the effects on simultaneous chemical and mechanical loading conditions. This type of testing will be very valuable when creating the appropriate link for the ISVs in the proposed model in Chapter III. As such, it is suggested that similar testing be completed for the four other Mg alloys (AZ61, AM30, AM60, and AE44) presented in Chapter IV.

REFERENCES

[1] E. Ghali, Magnesium and magnesium alloys, in: Uhligs Corros. Handb., 2000: p. 793.

[2] Y. Chen, Q. Wang, J. Peng, C. Zhai, W. Ding, Effects of extrusion ratio on the microstructure and mechanical properties of AZ31 Mg alloy, J. Mater. Process. Technol. 182 (2007) 281–285.

[3] M. Marya, L.G. Hector, R. Verma, W. Tong, Microstructural effects of AZ31 magnesium alloy on its tensile deformation and failure behaviors, Mater. Sci. Eng. 418 (2006) 341–356.

[4] A. Pardo, M.C. Merino, A.E. Coy, R. Arrabal, F. Viejo, E. Matykina, Corrosion behaviour of magnesium/aluminium alloys in 3.5 wt.% NaCl, Corros. Sci. 50 (2008) 823–834.

[5] K.B. Deshpande, Numerical modeling of micro-galvanic corrosion, Electrochimica Acta. 56 (2011) 1737–1745.

[6] S. Feliu Jr., C. Maffiotte, J.C. Galván, V. Barranco, Atmospheric corrosion of magnesium alloys AZ31 and AZ61 under continuous condensation conditions, Corros. Sci. 53 (2011) 1865–1872.

[7] R.B. Alvarez, H.J. Martin, M.F. Horstemeyer, M.Q. Chandler, N. Williams, P.T. Wang, et al., Corrosion relationships as a function of time and surface roughness on a structural AE44 magnesium alloy, Corros. Sci. 52 (2010) 1635–1648.

[8] A.N. Chamos, S.G. Pantelakis, V. Spiliadis, Fatigue behaviour of bare and pre-corroded magnesium alloy AZ31, Mater. Des. 31 (2010) 4130–4137.

[9] G.L. Song, A. Atrens, Corrosion mechanisms of magnesium alloys, Adv. Eng. Mater. 1 (1999) 11–33.

[10] R. Xin, B. Li, L. Li, Q. Liu, Influence of texture on corrosion rate of AZ31 Mg alloy in 3.5 wt.% NaCl, Mater. Des. 32 (2011) 4548–4552.

[11] Y. Unigovski, A. Eliezer, E. Abramov, Y. Snir, E.M. Gutman, Corrosion fatigue of extruded magnesium alloys, Mater. Sci. Eng. 360 (2003) 132–139.

[12] Z.Y. Nan, S. Ishihara, T. Goshima, Corrosion fatigue behavior of extruded magnesium alloy AZ31 in sodium chloride solution, Int. J. Fatigue. 30 (2008) 1181–1188.

[13] B.A. Shaw, Corrosion Resistance of Magnesium Alloys, in: L.J. Korb (Ed.), Asm Handb. Corros., Ninth Ed., ASM International Handbook Committee, Metals Park, 2003: p. 692.

[14] G.L. Makar, J. Kruger, Corrosion of magnesium, Int. Mater. Rev. 38 (1993) 138–153.

[15] G. Song, A. Atrens, Understanding Magnesium Corrosion—A Framework for Improved Alloy Performance, Adv. Eng. Mater. 5 (2003) 837–858.

[16] O. Lunder, T.K. Aune, K. Nisancioglu, Effect of Mn Additions on the Corrosion Behavior of Mould-Cast Magnesium Alloy AZ91, in: 1985: p. 383. 1–382. 6.

[17] R. Ambat, N.N. Aung, W. Zhou, Evaluation of microstructural effects on corrosion behaviour of AZ91D magnesium alloy, Corros. Sci. 42 (2000) 1433–1455.

[18] G. Song, Recent Progress in Corrosion and Protection of Magnesium Alloys, Adv. Eng. Mater. 7 (2005) 563–586.

[19] J.R. Rice, Inelastic constitutive relations for solids: An internal-variable theory and its application to metal plasticity, J. Mech. Phys. Solids. 19 (1971) 433–455.

[20] S. Murakami, Mechanical Modeling of Material Damage, J. Appl. Mech. Trans. Asme. 55 (1988) 280–286.

[21] S. Murakami, A continuum mechanics theory of anisotropic damage, in: J.P. Boehler (Ed.), Yielding Damage Fail. Anisotropic Solids, London, 1990: pp. 465–482.

[22] D.J. Bammann, E.C. Aifantis, A damage model for ductile metals, Nucl. Eng. Des. 116 (1989) 355–362.

[23] E.B. Marin, D.L. McDowell, Associative versus non-associative porous viscoplasticity based on internal state variable concepts, Int. J. Plast. 12 (1996) 629–669.

[24] P. Steinmann, I. Carol, A framework for geometrically nonlinear continuum damage mechanics, Int. J. Eng. Sci. 36 (1998) 1793–1814.

[25] G.Z. Voyiadjis, T. Park, Kinematics of damage for finite-strain elasto-plastic solids, Int. J. Eng. Sci. 37 (1999) 803–830.

[26] M. Brünig, Numerical analysis and elastic-plastic deformation behavior of anisotropically damaged solids, Int. J. Plast. 18 (2002) 1237–1270.

[27] R.A. Regueiro, D.J. Bammann, E.B. Marin, K. Garikipati, A nonlocal phenomenological anisotropic finite deformation plasticity model accounting for dislocation defects, J. Eng. Mater. Technol. Trans. Asme. 124 (2002) 380–387.

[28] K.N. Solanki, Physically Motivated Internal State Variable form of A Higher Order Damage Model for Engineering Materials with Uncertainty, Ph.D. Dissertation, Mississippi State University, 2008.

[29] B.A. Bilby, L.R.T. Gardner, A.N. Stroh, Continuous distributions of dislocations and the theory of plasticity, in: Extr. Actes Ixe Congr. Int. Mec. Appl., Brussels, 1957: pp. 35–44.

[30] E. Kröner, Allgemeine Kontinuums Theorie der Versetzungen und Eigenspannungen, Arch Rat Mech Anal. 4 (n.d.) 273–334.

[31] L. Davison, Kinematics of finite elastoplastic deformation, Mech. Mater. 21 (1995) 73–88.

[32] D.J. Bammann, M.L. Chiesa, M.F. Horstemeyer, L.I. Weingarten, Failure in Ductile Materials Using Finite Element Methods, in: Elsevier, Amsterdam, 1993.

[33] D.J. Bammann, M.L. Chiesa, G.C. Johnson, Modeling large deformation and failure in manufacturing processes, in: T. Tatsumi, E. Wanatabe, T. Kambe (Eds.), Theor. Appl. Mech., Elsevier Science, 1996: pp. 359–376.

[34] D.J. Bammann, A model of crystal plasticity containing a natural length scale, Mater. Sci. Eng. 309–310 (2001) 406–410.

[35] M.F. Horstemeyer, J. Lathrop, A.M. Gokhale, M. Dighe, Modeling stress state dependent damage evolution in a cast Al–Si–Mg aluminum alloy, Theor. Appl. Fract. Mech. 33 (2000) 31–47.

[36] J.D. Clayton, D.J. Bammann, D.L. McDowell, A geometric framework for the kinematics of crystals with defects, Philos. Mag. 85 (2005) 3983–4010.

[37] D.K. Francis, J.L. Bouvard, Y. Hammi, M.F. Horstemeyer, Formulation of a damage internal state variable model for amorphous glassy polymers, Int. J. Solids Struct. (n.d.).

[38] B.D. Coleman, M.E. Gurtin, Thermodynamics with Internal State Variables, J. Chem. Phys. 47 (1967) 597–613.

[39] M.F. Horstemeyer, D.J. Bammann, Historical review of internal state variable theory for inelasticity, Int. J. Plast. 26 (2010) 1310–1334.

[40] M.F. Horstemeyer, Integrated Computational Materials Engineering (ICME) for Metals: Using Multiscale Modeling to Invigorate Engineering Design with Science, John Wiley & Sons, 2012.

[41] H. Kwak, S. Chaudhuri, First-principles-based analysis on the role of RE doping on Mg alloy corrosion, in: Localized Corros. - Meas. Mech. Mitig., Columbus, Ohio, 2011.

[42] J. Xiao, H. Kwak, S. Chaudhuri, Understanding the role of intermetallic particles in localized corrosion: A multiscale modeling approach, in: Mater. Sci. Technol. Conf. Exhib. 2011 Ms T11, 2011: pp. 1374–1385.

[43] W. Dietzel, M. Pfuff, N. Winzer, Testing and mesoscale modelling of hydrogen assisted cracking of magnesium, Eng. Fract. Mech. 77 (2010) 257–263.

[44] M.C. Merino, A. Pardo, R. Arrabal, S. Merino, P. Casajús, M. Mohedano, Influence of chloride ion concentration and temperature on the corrosion of Mg–Al alloys in salt fog, Corros. Sci. 52 (2010) 1696–1704.

[45] R. Lindström, J.-E. Svensson, L.-G. Johansson, The Influence of Carbon Dioxide on the Atmospheric Corrosion of Some Magnesium Alloys in the Presence of NaCl, J. Electrochem. Soc. 149 (2002) B103–B107.

[46] R. Lindström, L.-G. Johansson, J.-E. Svensson, The influence of NaCl and CO2 on the atmospheric corrosion of magnesium alloy AZ91, Mater. Corros. 54 (2003) 587–594.

[47] M. Jönsson, D. Persson, D. Thierry, Corrosion product formation during NaCl induced atmospheric corrosion of magnesium alloy AZ91D, Corros. Sci. 49 (2007) 1540–1558.

[48] G. Ballerini, U. Bardi, R. Bignucolo, G. Ceraolo, About some corrosion mechanisms of AZ91D magnesium alloy, Corros. Sci. 47 (2005) 2173–2184.

[49] H.J. Martin, M.F. Horstemeyer, P.T. Wang, Comparison of corrosion pitting under immersion and salt-spray environments on an as-cast AE44 magnesium alloy, Corros. Sci. 52 (2010) 3624–3638.

[50] H.J. Martin, M.F. Horstemeyer, P.T. Wang, Effects of Variations in Salt-Spray Conditions on the Corrosion Mechanisms of an AE44 Magnesium Alloy, Int. J. Corros. 2010 (2010).

[51] H.J. Martin, M.F. Horstemeyer, P.T. Wang, Structure–property quantification of corrosion pitting under immersion and salt-spray environments on an extruded AZ61 magnesium alloy, Corros. Sci. 53 (2011) 1348–1361.

[52] G. Song, A. Atrens, D.S. John, X. Wu, J. Nairn, The anodic dissolution of magnesium in chloride and sulphate solutions, Corros. Sci. 39 (1997) 1981–2004.

[53] G. Song, A. Atrens, D. Stjohn, J. Nairn, Y. Li, The electrochemical corrosion of pure magnesium in 1 N NaCl, Corros. Sci. 39 (1997) 855–875.

[54] S. Mathieu, C. Rapin, J. Steinmetz, P. Steinmetz, A corrosion study of the main constituent phases of AZ91 magnesium alloys, Corros. Sci. 45 (2003) 2741–2755.

[55] S. Mathieu, C. Rapin, J. Hazan, P. Steinmetz, Corrosion behaviour of high pressure die-cast and semi-solid cast AZ91D alloys, Corros. Sci. 44 (2002) 2737–2756.

[56] G.L. Makar, J. Kruger, Corrosion Studies of Rapidly Solidified Magnesium Alloys, J. Electrochem. Soc. 137 (1990) 414–421.

[57] M. Santamaria, F. Quarto, S. Zanna, P. Marcus, Initial surface film on magnesium metal: A characterization by X-ray photoelectron spectroscopy (XPS) and photocurrent spectroscopy (PCS), Electrochim Acta. 53 (2007) 1314–1324.

[58] A. Pardo, M.C. Merino, A.E. Coy, F. Viejo, R. Arrabal, S. Feliú Jr., Influence of microstructure and composition on the corrosion behaviour of Mg/Al alloys in chloride media, Electrochimica Acta. 53 (2008) 7890–7902.

[59] G. Galicia, N. Pébère, B. Tribollet, V. Vivier, Local and global electrochemical impedances applied to the corrosion behaviour of an AZ91 magnesium alloy, Corros. Sci. 51 (2009) 1789–1794.

[60] ASTM B117 – 07a (2007) Standard Practice for Operating Salt Spray (Fog) Apparatus, Vol. 03.02, (2007).

[61] ASTM G31 – 72 (2004) Standard Practice for Laboratory Immersion Corrosion Testing of Metals, Vol. 03.02, (2004).

[62] K.R. Baldwin, C.J.E. Smith, Accelerated corrosion tests for aerospace materials: current limitations and future trends, Aircr. Eng. Aerosp. Technol. 71 (1999) 239–244.

[63] N. LeBozec, N. Blandin, D. Thierry, Accelerated corrosion tests in the automotive industry: A comparison of the performance towards cosmetic corrosion, Mater. Corros. 59 (2008) 889–894.

[64] G. Song, D. St. John, C. Bettles, G. Dunlop, The corrosion performace of magnesium alloy AM-SC1 in automotive engine block applications, Jom J. Miner. 57 (2005) 54–56.

[65] R. Ambat, N.N. Aung, W. Zhou, Studies on the influence of chloride ion and pH on the corrosion and electrochemical behaviour of AZ91D magnesium alloy, J. Appl. Electrochem. 30 (2000) 865–874.

[66] M.K. Cavanaugh, R.G. Buchheit, N. Birbilis, Modeling the environmental dependence of pit growth using neural network approaches, Corros. Sci. 52 (2010) 3070–3077.

[67] D.K. Xu, N. Birbilis, D. Lashansky, P.A. Rometsch, B.C. Muddle, Effect of solution treatment on the corrosion behaviour of aluminium alloy AA7150: Optimisation for corrosion resistance, Corros. Sci. 53 (2011) 217–225.

[68] J. Zhu, L.H. Hihara, Corrosion of continuous alumina-fibre reinforced Al–2 wt.% Cu–T6 metal–matrix composite in 3.15 wt.% NaCl solution, Corros. Sci. 52 (2010) 406–415.

[69] M.L. Doche, J.Y. Hihn, A. Mandroyan, C. Maurice, O. Hervieux, X. Roizard, A novel accelerated corrosion test for exhaust systems by means of power ultrasound, Corros. Sci. 48 (2006) 4080–4093.

[70] M.G. Fontana, Corrosion Principles, in: Corros. Eng., McGraw-Hill, 1986: pp. 12–38.

[71] G. Song, A. Atrens, X. Wu, B. Zhang, Corrosion behaviour of AZ21, AZ501 and AZ91 in sodium chloride, Corros. Sci. 40 (1998) 1769–1791.

[72] M.-C. Zhao, M. Liu, G. Song, A. Atrens, Influence of the β-phase morphology on the corrosion of the Mg alloy AZ91, Corros. Sci. 50 (2008) 1939–1953.

[73] L.M. Kachanov, Time of the rupture process under creep conditions, Izvestiya Akademii Nauk SSSR, Otd. Tekhnicheskih. 8 (1958) 26–31.

[74] D.J. Bammann, K.N. Solanki, On kinematic, thermodynamic, and kinetic coupling of a damage theory for polycrystalline material, Int. J. Plast. 26 (2010) 775–793.

[75] T. Toh, W.M. Baldwin, Stress Corrosion Cracking and Embrittlement, J. Wiley & Sons, New York, 1956.

[76] M. Kappes, M. Iannuzzi, R.M. Carranza, Hydrogen Embrittlement of Magnesium and Magnesium Alloys: A Review, J. Electrochem. Soc. 160 (2013) C168–C178.

[77] C.A. Walton, H.J. Martin, M.F. Horstemeyer, W.R. Whittington, C.J. Horstemeyer, P.T. Wang, Corrosion stress relaxation and tensile strength effects in an extruded AZ31 magnesium alloy, Corros. Sci. (n.d.).

[78] A. Atrens, N. Winzer, W. Dietzel, Stress Corrosion Cracking of Magnesium Alloys, Adv. Eng. Mater. 13 (2011) 11–18.

[79] N. Winzer, A. Atrens, W. Dietzel, V.S. Raja, G. Song, K.U. Kainer, Characterisation of stress corrosion cracking (SCC) of Mg–Al alloys, Mater. Sci. Eng. 488 (2008) 339–351.

[80] Y. Unigovski, L. Riber, E.M. Gutman, Corrosion Stress Relaxation in Pure Magnesium and Die-Cast Mg Alloys, J. Met. Mater. Miner. 17 (2007) 1–7.

[81] L. Davison, A.L. Stevens, M.E. Kipp, Theory of spall damage accumulation in ductile metals, J. Mech. Phys. Solids. 25 (1977) 11–28.

[82] L.E. Malvern, Introduction to the Mechanics of a Continuous Medium, Prentice-Hall, Inc., Englewood Cliffs, NJ, 1969.

[83] I.U.N. Rabotnov, Creep Problems in Structural Members, in: North-Holland Pub. Co., Amsterdam, 1969.

[84] B. Budiansky, R.J. O'Connell, Elastic moduli of a cracked solid, Int. J. Solids Struct. 12 (1976) 81–97.

[85] M.F. Horstemeyer, A.M. Gokhale, A void–crack nucleation model for ductile metals, Int. J. Solids Struct. 36 (1999) 5029–5055.

[86] J.R. Davis, J.D. Destefani, G.M. Crankovic, eds., ASM Handbook: Corrosion, ASM International, 1987.

[87] R.G. Ehl, A.J. Ihde, Faraday's electrochemical laws and the determination of equivalent weights, J. Chem. Educ. 31 (1954) 226.

[88] E.S. Amis, Coulomb's law and the qualitative interpretation of reaction rates, J. Chem. Educ. 28 (1951) 635.

[89] P.R. Roberge, Corrosion Electrochemistry, in: Corros. Basics - Introd., Second Ed., McGraw-Hill, Houston, Texas, 2008: pp. 35–47.

[90] A.W. Hull, N.H. Williams, Determination of Elementary Charge E from Measurements of Shot-Effect., Phys. Rev. 25 (1925) 147–173.

[91] H.J. Martin, R.B. Alvarez, J. Danzy, M.F. Horstemeyer, P.T. Wang, Quantification of Corrosion Pitting Under Immersion and Salt Spray Environments on an As-Cast AM60 Magnesium Alloy, Corrosion. 68 (2012) 571–585.

[92] C.A. Walton, H.J. Martin, M.F. Horstemeyer, P.T. Wang, Quantification of corrosion mechanisms under immersion and salt-spray environments on an extruded AZ31 magnesium alloy, Corros. Sci. 56 (2012) 194–208.

[93] Z. Trojanová, P. Lukáč, K.H. Kim, Stress relaxation in selected magnesium alloys, Key Eng. Mater. 345-346 (2007) 1613–1616.

[94] Z. Trojanová, K. Máthis, P. Lukáč, G. Németh, F. Chmelík, Internal stress and thermally activated dislocation motion in an AZ63 magnesium alloy, Mater. Chem. Phys. 130 (2011) 1146–1150.

[95] Metals handbooks vol. 2: properties and selection, 10th ed., ASM International, [S.l.], 1990.

[96] Z. Trojanová, P. Lukác, K.U. Kainer, Stress Relaxation in AX41 Magnesium Alloy Studied at Elevated Temperatures, Adv. Eng. Mater. 9 (2007) 370–374.

[97] E. Gutman, Surface plasticity modification using electrolytic etching, Surf. Coatings Technol. 67 (1994) 133–136.

[98] S. Matsuoka, M. Oguri, T. Murai, Mechanical properties and extrudability of magnesium alloys, in: Proc. 41st Gen. Meet., 2004: pp. 215–216.

[99] Failure Analysis, in: Met. Handb., ASM International, 1997.

[100] M. Bobby Kannan, W. Dietzel, Pitting-induced hydrogen embrittlement of magnesium–aluminium alloy, Mater. Des. 42 (2012) 321–326.

[101] W.M. Pardue, F.H. Beck, M.G. Fontana, Propagation of stress-corrosion cracking in a magnesium-based alloy as determined by several techniques, Trans Am Soc Met. 64 (1961) 539–548.

[102] R.S. Stampella, R.P.M. Procter, V. Ashworth, Environmentally-induced cracking of magnesium, Corros. Sci. 24 (1984) 325–341.

APPENDIX A

MODEL CONSTANTS FOR MG ALLOY APPLICATION

A.1 Physical Constants

Table A.1 Physical constants used for model application.

Parameter	Values
F (C/mol)	96485
M (g/mol)	24.305
z	2
k_e (Nμm^2/C^2)	8.987E+21
q_1 (C)	1E-19
q_2 (C)	1E-19
ε_0 (C^2/Nμm^2)	8.85419E-24
MO/MO_0	0.15
z_{ic}	3

A.2 Material Constants

Table A.2 Material constants used for model application.

Parameter	Extruded AZ31		Extruded AZ61		Extruded AM30		Cast AM60		Cast AE44	
	SS	IM	SS	IM	SS	IM	SS	IM	SS	IM
C_1	-5.5E-04	1.7E-03	2.5E-05	1.1E-04	2.4E-04	-5.0E-05	1.2E-03	-1.5E-03	-1.2E-02	-1.0E-02
C_2	1.6E-04	1.9E-04	3.0E-04	2.7E-04	0	1.1E-04	1.8E-05	3.2E-05	1.0E-04	1.7E-04
C_3	0.0389	0.005	0.216	0.21	0	0.055	0.09	0.05	0.45	0.21
C_4	0.000377	0.00034	0.0007	0.0012	0.000045	0.00138	0	0	0.000185	0.000412
C_5	-0.58	-0.58	-0.4	-0.415	-0.09	-1.04	0	0	-0.105	-0.18
C_6	0.21	0.18	0.059	0.031	0.065	0.111	0.0066	0.0098	0.095	0.11
C_7	0.195	0.23	0.38	0.5	0.22	0.16	0.138	0.15	0.08	0.245
C_8	39.7	38	27.5	26.1	74	50.6	110	76.1	36.5	33.9
C_9	-0.00785	-0.01	-0.06	-0.038	0.0178	-0.033	-0.12	-0.051	-0.085	-0.035
C_{10}	30.1	28.5	19.5	12	0	33.1	0	33.2	32.6	33.9
C_{11}	0.2	0.205	0.215	0.28	0	0.143	0	0.143	0.02	-0.035
C_{12}	0.16	0.21	0.0235	0.012	0.17	0.055	0.045	0.065	0.1	0.05
C_{13}	0.12	0.06	0.5	0.69	0.65	0.4	0.35	0.4	0.1	0.43
C_{14}	0.343	0.336	0	0	0.435	0	0	0.315	0	0.5
C_{15}	-0.192	-0.3	0	0	-0.0651	0	0	-0.239	0	-0.5

SS and IM denote exposure to the salt spray and immersion environment, respectively.